An investigation in actuator disc CFD solution applicabillity for aeroacoustic analysis of propellers and rotors.

UNIVERSITY OF TWENTE.

Internship report

A.P. Verweij

Report on the internship within the Master Mechanical Engineering

Carried out by:	A.P. Verweij S0096830
Host institution:	Centro Italiano Richerche Aerospaziali (CIRA) (Italian Aerospace Research Center) Physics of Fluids Capua, Italy
Supervisor host organisation:	Ing. Marcello Amato Physics of Fluids, Head
Home institution:	Universiteit Twente The Netherlands
Supervisor home institution:	Prof. Dr. Ir. H.W.M. Hoeijmakers
Duration of internship:	April 4th 2010 to Juli 9th 2010

Preface

This report covers the project that I worked on in the fifteen weeks I was working at the Italian center for Aerospace Research(CIRA) for my internship. I worked with the Physics of Fluids group led by Marcello Amato, to whom I am grateful for the challenging assignment I was giving, as well as his directions, confidence and guiding remarks during the project. Furthermore, I would like to thank Ainslie French for getting me up to speed with the FORTAN code and all the systems used at CIRA. My gratitude also goes to Pierluigi Vitaliano for helping me out with the aerodynamic analysis of the ZEN results, to Mattia Barbarino who learned me how the basics of the aeroacoustic code, and to Damiano Casalino for giving me all the good directions in the aeroacoustic analysis of the prop-rotor. Also, I would like to give my special thanks to Antonio Visingardi, who spent many weeks helping me during the struggle to find the inconsistencies in the RAMSYS to ZEN conversions. Without the help of the people named I could never have covered so many bases in the short amount of time given for the project. Finally, my gratitude goes to Professor Hoeijmakers for giving me the opportunity to go to CIRA for my internship altogether, and indirectly to Jasper Tomas, whose previous report work on the actuator disk made it easy for me to get comfortable with the mechanisms involved in the project.

Table of Contents

Nomenclature

General

$\vec{x} = (x, y, z)^T$	Global Cartesian coordinates	[m,m,m]^T
$\vec{u} = (u, v, w)^T$	Velocity vector in global Cartesian coordinates	[m/s]
$(r, \theta, z)^T$	Polar coordinates in the actuator disk plane	[m,rad,m]^T
q	Velocity magnitude	[m/s]
V, u_n	Velocity component normal to the actuator disk	[m/s]
M	Local Mach Number	[-]
a	Local speed of sound	[m/s]
ρ	Local fluid density	[kg/m^3]
p	Local fluid pressure	[kg/m^2]
T	Local fluid temperature	[K]
H	Local fluid total enthalpy	[J/kg]
E	Local fluid total energy	[J/kg]

Propeller specific

R	Propeller tip radius	[m]
r	Local radius of a point in polar coordinates	[m]
$\vec{r}$	Non-dimensional radius (r / R)	[-]
D	Propeller/rotor diameter	[m]
T	Propeller/rotor thrust	[N]
P	Propeller/rotor power	[W]
Ω	Propeller/rotor rotational speed	[rad/s]
n	Propeller/rotor rotations per second	[1/s]
$J = \frac{V}{nD}$	Propeller/rotor advance ratio	[-]
c	Propeller/rotor local blade chord length	[m]
α	Propeller/rotor local angle of incidence with the free stream	[rad]

ZEN specific

$\frac{dC_T}{d\vec{r}}$	Local thrust coefficient	[-]
$\frac{dC_P}{d\vec{r}}$	Local power coefficient	[-]
$\frac{dC_R}{d\vec{r}}$	Local radial force coefficient	[-]
N_r	Number of cells in radial direction	[-]
N_θ	Number of cells in circumferential direction	[-]
N_z	Number of cells in longitudinal direction	[-]
Δ	Unsteady distribution width	[rad]
DTS	Number of timesteps per revolution	[-]

RAMSYS specific

C_N	Local normal force coefficient	[-]
C_A	Local force coefficient in chordwise direction	[-]
C_Y	Local force coefficient in spanwise direction	[-]

Aero-acoustic specific

$\square[..]$	Wave equation operator	
$\delta(x)$	Dirac delta function	
$v(\vec{x},t)$	Velocity of a point on the control surface $f=0$	[m/s]
c	Local speed of sound	[m/s]
t	Observer time	
τ	Emission time	[s]
τ_{ret}	Retarded time	[s]
r	Distance between source and observer	[m]
$[..]_{ret}$	Evaluated at the retarded time.	

1. Introduction

This report covers an investigation into the feasibility of the use of the actuator disk approach in aero-acoustic analysis of a propeller/rotor. In the actuator disk approach, a propeller or rotor is represented as an infinitesimally thin disk where flow field quantities are added to the flow in a discontinuous jump. This approximation results in a dramatic reduction of computational workload. The approach has been validated on aerodynamical grounds for a steady computation in earlier investigations. Recent developments at CIRA extend the use of the actuator disk approach to unsteady flow calculation. However, little investigation has been done in the past on the effects of using the approach in this way and therefore in the first part of the project, the effect of using the actuator approach in unsteady computation is investigated. Also the way to properly model a specific propeller/rotor as an unsteady actuator disk boundary condition has not been formulated before, and so a distribution is constructed and validated.

In the second part of the report, the output of the unsteady CFD computations are used as input data for an in-house aero-acoustic code that is based on the permeable Ffowcs Williams-Hawkings analogy. This can be done by formulating a surface around the actuator disk. In order to investigate the result of using this approach, a comparison is made between computations that use this ZEN input data and regular input data containing a moving body. The report is structured in the following way.

In chapter 2, an overview of ZEN is given, which is the used CFD code. This chapter starts with a small introduction into the features of ZEN and the theory behind the actuator disk approach. Then, a short description of the unsteady form of ZEN (UZEN) is given, together with an explanation in the way an unsteady boundary condition is formulated. The last paragraph of the chapter contains a description of possible phenomena that can emerge with the use of UZEN in comparison to ZEN.

Chapter 3 contains an investigation into ZEN and UZEN using a simple test case. First, a steady simulation is done to generate reference data and investigate the effects of mesh density. Then, the unsteady boundary condition is constructed and ran through a series of tests. The chapter ends with observations and conclusions on the effects of using the actuator disk approach in UZEN for propellers/rotors.

Then in chapter 4, an attempt is made in generating an actuator disk boundary condition from the output data of a potential flow solver for number of propellers and rotors. The code used for this is RAMSYS. The reason for this is that RAMSYS output can be used reference data for the aero-acoustic analysis. The chapter contains a description on how to convert the output data of RAMSYS to an actuator disk boundary condition. Then, the result is investigated for 3 different geometries and a geometry is chosen on which the aero-acoustic investigation will be performed.

Chapter 5 covers the investigation of aero-acoustics. As with the other chapters, this section starts with an introduction into the method used. The first paragraph contains information about the theory of the FW-H analogy and the description of the test setup. Then, a number of tests are conducted comparing the results of a variety of aero-acoustic simulations with UZEN input data to a simulation done with RAMSYS input data. This will lead to a number of observations and conclusions at the end of the chapter.

Finally all the conclusions made in the project are summarized in chapter 6, which is followed by several recommendations about possible future work on the subject in chapter 7. This chapter also lists a selection of tests that need to be conducted to check whether the conclusions made in the project are valid.

Also, since the report consists of a variety of subjects and the amount of tests done and displayed is quite large, the author has tried to keep the report readable by adding small sections that summarize the conclusions in between chapters. With the same goal, all of the in depth theory used has been placed in the appendix.

2. UZEN overview

This chapter contains information on the flow solver used in the investigation. In the first subchapter the specifications of the ZEN solver are introduced, as well as the necessary input and output files. In the second subchapter, the actuator disk boundary condition is described, together with the non-dimensionalization involved. After this the implementation of the actuator disk boundary condition in the solver is explained in subchapter three. Finally, subchapter four starts with a description of the unsteady ZEN solver. After this, the chosen definition of the unsteady boundary condition distribution is explained and motivated.

2.1. Introduction

The ZEN (Zonal Euler Navier-Stokes) simulation system is a set of codes for the analysis of steady aerodynamic flows around complex geometry. It solves the RANS equations, and optionally Euler or TLNS equations using the multi-zone approach. It is based on a multi-block structured grid finite volume approach which is a Jameson-like quasi second order accurate cell centered method. For Euler blocks, artificial dissipation is introduced based on the Jameson artificial dissipation model, which introduces a dissipative flux at each cell face. For RANS computation, the method is able to use a variety of turbulence models that include algebraic models, e.g. Baldwin Lomax, κ-ε models and κ-ω models.

Furthermore, ZEN has optional features that include a TVD switch and the usage of multi-grid to enhance stability and computational speed respectively. Relaxation is performed with the Runge-Kutta time stepping scheme, which utilizes implicit residual averaging. Also the time step needed is evaluated locally, i.e. local time stepping is employed.

ZEN uses with the following input files:

IN:	Contains the configuration parameters for the simulation, as well as the choice of solution type.
INTOO:	Contains additional configuration parameters for the simulation. (Optional)
GRID:	Contains the structured grid. (Binary file)
SELECT:	Contains the configuration parameters to obtain desired output variables.
BCDAT:	Contains the block specific boundary condition data.

The output consists of:

OUT:	Contains information about the solution process
FLOW:	Contains the flow solution
VISFOR:	Contains the desired output variables in Tecplot360 format.

This report includes the use of ZEN using the actuator disk boundary condition in Euler flow only.

2.2. Actuator disk boundary condition

The actuator disk boundary condition is an internal boundary condition that imposes addition of flow field quantities to the flow through discontinuities that work according to the general momentum theory. (Glauert, 1963). Across the disk, mass flux is continuous, while there is a discontinuous jump in momentum and total energy flux. These discontinuous jumps are implicitly defined by specifying jumps in other variables. ZEN allows this to be done in two ways, that is, with a field model and a force model definition of boundary condition data. Because this report will only include simulations performed using boundary conditions defined for the force model because of the limited capability of unsteady ZEN, the field model will not be mentioned hereafter. The force model boundary condition distribution is defined in the following way.

2.2.1. ZEN force model actuator disk boundary condition

The ZEN force model contains a distribution of force coefficient data. Based on the general momentum theory, an added axial force, i.e. thrust induces in a jump in pressure while added radial and tangential force exerted induces in a jump in momentum.

The non-dimensional data distribution in the boundary condition consists of a local thrust coefficient C_a, a local power coefficient C_p, and a local radial force coefficient C_r, which are function of radius r and angle θ. The added axial tangential and radial force is calculated in ZEN from the non-dimensional boundary condition data in the following way: (Excerpt from the CESAR-report by A. French)

Local axial force

The non-dimensionalization of axial force is done according to the coefficient definition of Renard. The Renard thrust coefficient is defined as:

$$C_T = \frac{T}{\rho_\infty n^2 D^4} \tag{1.1}$$

Therefore locally, the thrust can be defined as:

$$dT = \rho_\infty n^2 D^4 dC_T \rightarrow \frac{dT}{d(r/R)} = \rho_\infty n^2 D^4 \frac{dC_T}{d(r/R)} \tag{1.2}$$

Where $dT/d(r/R)$ is the local axial force per unit scaled radius and $dC_T/d(r/R)$ is the local thrust coefficient per unit scaled radius. The radial coordinate can be made non-dimensional by:

$$\overline{r} = \frac{r}{R}$$

$$d\overline{r} = \frac{dr}{R}$$

Where R is the radius of the disk.

Using the definition of the advance ratio and the fact that $D = 2R$:

$$\frac{dT}{d\bar{r}} = \frac{4\rho_\infty V_\infty^2 R^2}{J^2}\frac{dC_T}{d\bar{r}} \tag{1.3}$$

Therefore, the axial force on a circular element of scaled radius $d\bar{r}$ is:

$$dT = \frac{4\rho_\infty V_\infty^2 R^2}{J^2}\frac{dC_T}{d\bar{r}}d\bar{r} \tag{1.4}$$

The local axial force per unit area is obtained by dividing the result by the area of a circular strip $(2\pi\bar{r}R^2 d\bar{r})$:

$$F_a = \frac{2\rho_\infty V_\infty^2}{J^2\pi\bar{r}}\frac{dC_T}{d\bar{r}} \tag{1.5}$$

Using the definition of the speed of sound for an ideal gas: $c_\infty^2 = \gamma p_\infty / \rho_\infty$

$$\boxed{F_a = \frac{2\rho_\infty V_\infty^2}{J^2\pi\bar{r}}\frac{dC_T}{d\bar{r}} = \frac{2\gamma p_\infty V_\infty^2}{c_\infty^2 J^2\pi\bar{r}}\frac{dC_T}{d\bar{r}} = \frac{2\gamma p_\infty M_\infty^2}{J^2\pi\bar{r}}\frac{dC_T}{d\bar{r}}} \tag{1.6}$$

Where M_∞ is the Mach number of the free stream. The result is the definition used in the subroutine biprop.f of the ZEN code.

Local tangential force

The local tangential force is calculated from the local power coefficient. The Renard power coefficient is defined as:

$$C_P = \frac{P}{\rho_\infty n^3 D^5} \tag{1.7}$$

Therefore locally, the power can be defined as:

$$dP = \rho_\infty n^3 D^5 dC_P \rightarrow \frac{dP}{d\bar{r}} = \rho_\infty n^3 D^5 \frac{dC_P}{d\bar{r}} \tag{1.8}$$

The total power is equal to the product of the tangential velocity and the total tangential force, therefore:

$$P = V_\theta . f_{\theta_{total}} = 2\pi nr. f_{\theta_{total}}$$

The local power therefore is:

$$dP = V_\theta . f_\theta = 2\pi nR\bar{r}. f_\theta \tag{1.9}$$

Combining equations(1.8) and (1.9) results in the tangential force per unit non-dimensional radius:

$$\frac{df_\theta}{d\bar{r}} = \frac{\rho_\infty n^2 D^5}{2\pi R\bar{r}} \frac{dC_P}{d\bar{r}} \tag{1.10}$$

Using the definition of the advance ratio and the fact that $D = 2R$:

$$\frac{df_\theta}{d\bar{r}} = \frac{4\rho_\infty V_\infty^2 R^2}{J^2 \pi \bar{r}} \frac{dC_P}{d\bar{r}} \tag{1.11}$$

Therefore, the tangential force on a circular element of scaled radius $d\bar{r}$ is:

$$df_\theta = \frac{4\rho_\infty V_\infty^2 R^2}{J^2 \pi \bar{r}} \frac{dC_P}{d\bar{r}} d\bar{r} \tag{1.12}$$

The local tangential force per unit area is obtained by dividing the result by the area of a circular strip $(2\pi\bar{r}R^2 d\bar{r})$:

$$F_\theta = \frac{4\rho_\infty V_\infty^2 R^2}{2J^2 R^2 \pi^2 \bar{r}^2 d\bar{r}} \frac{dC_P}{d\bar{r}} d\bar{r} = \frac{2\rho_\infty V_\infty^2}{\left(J\pi\bar{r}\right)^2} \frac{dC_P}{d\bar{r}} \tag{1.13}$$

Again using the definition of the speed of sound for an ideal gas results in:

$$\boxed{F_\theta = \frac{2\rho_\infty V_\infty^2}{\left(J\pi\bar{r}\right)^2} \frac{dC_P}{d\bar{r}} = \frac{2\gamma p_\infty V_\infty^2}{c_\infty^2 \left(J\pi\bar{r}\right)^2} \frac{dC_P}{d\bar{r}} = \frac{2\gamma p_\infty M_\infty^2}{\left(J\pi\bar{r}\right)^2} \frac{dC_P}{d\bar{r}}} \tag{1.14}$$

Which is the definition used in the subroutine biprop.f of the ZEN code.

Local axial force

The non-dimensionalization of radial force is done in a similar way to the non-dimensionalization of the axial force. The radial force coefficient is defined as:

$$C_r = \frac{F_r}{\rho_\infty n^2 D^4} \tag{1.15}$$

Where F_r is the total radial force on the disk. Locally:

$$dF_r = \rho_\infty n^2 D^4 dC_R \rightarrow \frac{dF_r}{d\bar{r}} = \rho_\infty n^2 D^4 \frac{dC_R}{d\bar{r}} \tag{1.16}$$

Following the same procedure of non-dimensionalization as was used for the axial force, the local axial force per unit area is found to be:

$$\boxed{F_r = \frac{2\gamma p_\infty M_\infty^2}{J^2 \pi \overline{r}} \frac{dC_R}{d\overline{r}}}$$

Which is again the definition used in the subroutine biprop.f of the ZEN code.

2.3. Boundary condition formulation

The force model boundary condition data is used in ZEN to calculate the discontinuous jump between the blocks where the actuator disk boundary condition is located. This is done in the following way. Assume the actuator disk to be located at the interface of two blocks, namely block 1 and block 2, illustrated in figure 1 (National Aerospace Laboratory NLR, 1987).

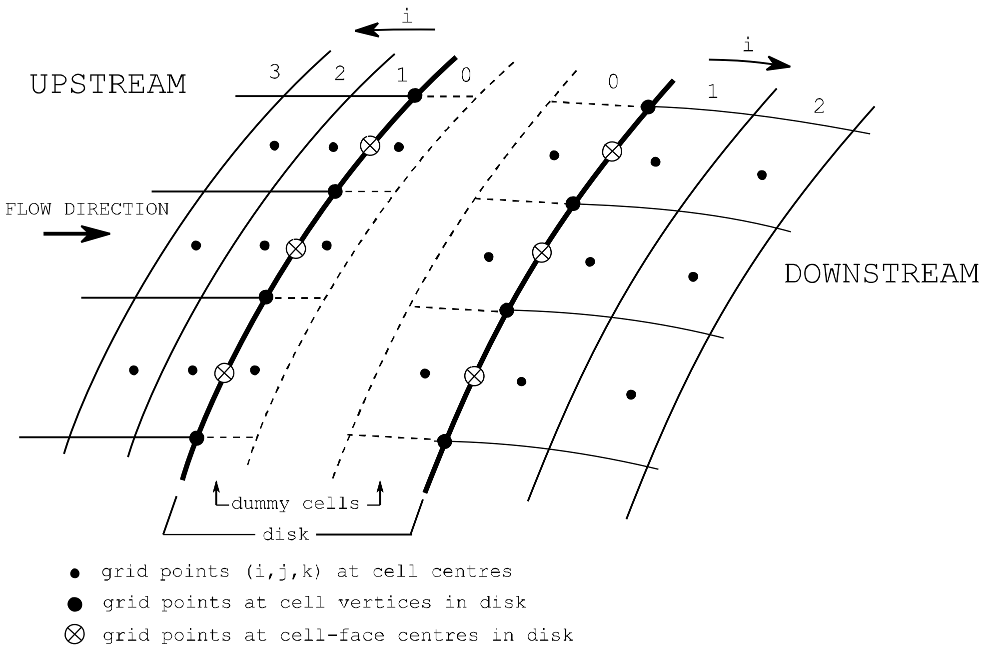

figure 1: AD cell locations and indices

The following steps are carried out twice during one iteration; once for each block.

The subscript notation used in this section comprises of two indices. The first indicates the cell number of the block, which is positive away from the boundary. The second index indicates the block number. Cell number 0 indicates the dummy cell.

Initially the values of the local flow at the interface between blocks, i.e. the position of the actuator disk, are calculated by linear interpolation of the values of the cell centers at both sides of the interface. The index *d* indicates the values at the disk.

$$\rho_d = \frac{1}{2}\left[\rho_{1,1} + \rho_{1,2}\right]$$

$$(\rho\vec{u})_d = \frac{1}{2}\left[(\rho\vec{u})_{1,1} + (\rho\vec{u})_{1,2}\right] \quad (1.17)$$

$$p_d = \frac{1}{2}\left[p_{1,1} + p_{1,2}\right]$$

Where $\vec{u}$ is the velocity vector $(u,v,w)^T$. Furthermore, the velocity normal to the disk, Q_{out}, is defined as:

$$Q_{out} = \frac{(\rho\vec{u})_d}{\rho_d} \cdot \vec{\hat{n}} \tag{1.18}$$

where $\vec{\hat{n}}$ is the unit normal pointing from block 1 to block 2. Q_{out} indicates in which direction the momentum is flowing; If Q_{out} is less than zero, momentum flows from block 2 to block 1 and if Q_{out} is positive momentum flows from block 1 to block 2. If Q_{out} equals zero, there is no exchange of momentum between the blocks.

When the flow direction is known, the location of the up- and downstream blocks is also known. Hereafter, it is assumed that block 1 is the upstream block and block 2 is the block downstream.

Since the forces exerted by the disk on the fluid have been calculated, they can be added to the momentum equations. In ZEN, the local axial force is added directly to the local pressure downstream in coherence with the general momentum theory. The resulting value of the dummy cell then becomes:

$$\begin{aligned} p_{0,2} &= 2p_d - p_{1,2} + F_a \\ p_{0,1} &= 2p_d - p_{1,1} - F_a \end{aligned} \tag{1.19}$$

These pressures are used to calculate the density at the up-and downstream side by using Poisson's relation for isentropic flows $p = C\rho^\gamma$:

$$\rho_{0,2} = \rho_d \left(\frac{p_{0,2}}{p_d} \right)^{\frac{1}{\gamma}} \tag{1.20}$$

$$\rho_{0,1} = \rho_d \left(\frac{p_{0,1}}{p_d} \right)^{\frac{1}{\gamma}} \tag{1.21}$$

With these quantities the total enthalpy per unit volume is calculated:

$$(\rho H)_{0,1} = \frac{\gamma}{\gamma - 1} p_{0,1} + \frac{1}{2} \rho_{0,1} |\vec{u}|^2 - \rho_{0,1} H_\infty \tag{1.22}$$

ZEN calculated the enthalpy always in block 1, even if block 1 is on the downstream side. This is because the same steps are also done for the block on the other side of the actuator disk.

Furthermore, the velocity normal to the disk Q_{out} is used to calculate the momentum components to be added to the downstream side:

$$\Delta(\rho u) = \frac{F_x}{Q_{out}} \tag{1.23}$$

$$\Delta(\rho v) = \frac{F_y}{Q_{out}} \tag{1.24}$$

$$\Delta(\rho w) = \frac{F_z}{Q_{out}} \tag{1.25}$$

Where F_x, F_y and F_z are the x, y and z components of the tangential and radial non-dimensional force in the actuator disk plane.

Finally, these components are added to the momentum components on the downstream side. The resulting value at the dummy cell of each block therefore becomes:

(Upstream) block 1:

$$\begin{aligned}
(\rho u)_{0,1} &= 2(\rho u)_d - (\rho u)_{1,1} - \Delta(\rho u) \\
(\rho v)_{0,1} &= 2(\rho v)_d - (\rho v)_{1,1} - \Delta(\rho v) \\
(\rho w)_{0,1} &= 2(\rho w)_d - (\rho w)_{1,1} - \Delta(\rho w)
\end{aligned} \tag{1.26}$$

(Downstream) block 2:

$$\begin{aligned}
(\rho u)_{0,2} &= 2(\rho u)_d - (\rho u)_{1,2} + \Delta(\rho u) \\
(\rho v)_{0,2} &= 2(\rho v)_d - (\rho v)_{1,2} + \Delta(\rho v) \\
(\rho w)_{0,2} &= 2(\rho w)_d - (\rho w)_{1,2} + \Delta(\rho w)
\end{aligned} \tag{1.27}$$

2.4. Unsteady ZEN solver

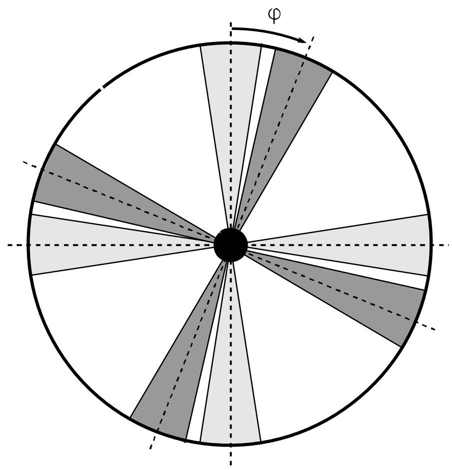

figure 2: rotation of boundary condition

Basic steady ZEN input data for a rotor consists of non-dimensional force coefficients as a function of r and ψ, represented on a disk. In a UZEN computation (i.e. Unsteady ZEN), there is an option that allows the actuator disk boundary condition to rotate in time in order to simulate a rotating propeller, thus generating non-steady flow.

The concept is illustrated in a very basic way in figure 2. Every physical time step, the boundary condition is rotated with angle $\varphi = 360° / \mathrm{TPR}$, where TPR represents the number of time steps per rotation, which can be specified in the 'IN' file of ZEN. Here, the user is able to specify the amount of time steps to be calculated.

The unsteady ZEN solver solves can run for a specified number of iterations or until the residual of the continuity equation is reduced by a specified factor. Then, the solver uses a dual time step approach to solve the problem in time.

This method has certain limitations, because only one force distribution in ψ can be specified for all time steps. This boundary condition is then rotated around the actuator disk axis, implying that the method is only applicable for blades or rotors in an axisymmetrical flow. Therefore, the method is only applicable for cases where the following conditions are both present:

- The propeller/rotor axis is at zero angle of incidence with the free stream (zero inflow angle).
- Axisymmetrical hub/nacelle geometry is used.

For the purpose of this investigation, which is to check the effects numerical effects of UZEN in comparison with steady ZEN, this is sufficient. In fact, the input data for the currently adopted actuator disk BC in ZEN consists of time averaged data, which are used to create an unsteady boundary condition.

2.4.1. Construction of the unsteady BCDAT

The BCDAT file for UZEN is constructed from a BCDAT file valid for a steady ZEN computation. In contrast to UZEN, steady ZEN flow solutions are naturally not a function of time. This means that the force coefficients used in the boundary condition data are defined as the fully developed time averaged flow field induced by the propeller/rotor.

For the zero inflow angle condition, UZEN conveniently adopts the same approach. Therefore, the integral of the force coefficients in the boundary condition distribution over the disk surface at any time has to be equal to the integral of the force coefficients in the boundary condition distribution over the disk surface for a steady ZEN run. If this is ensured, the same amount of time averaged momentum is added to the flow and in theory the resulting time averaged flow field will be identical to the steady solution.

Furthermore, in order to simulate a propeller, the unsteady distribution of force coefficients should be constructed it such a way that it simulates the presence of a propeller/rotor at any time. This is explained in the following paragraph.

2.4.2. Conversion of steady to unsteady BCDAT

In order to simulate the presence of a propeller, the force coefficient data prescribed in the BCDAT file used for a steady ZEN simulation are redistributed. An example of this transformation for a six blade propeller is depicted in figure 3 and figure 4. A method for constructing this distribution is presented in this paragraph.

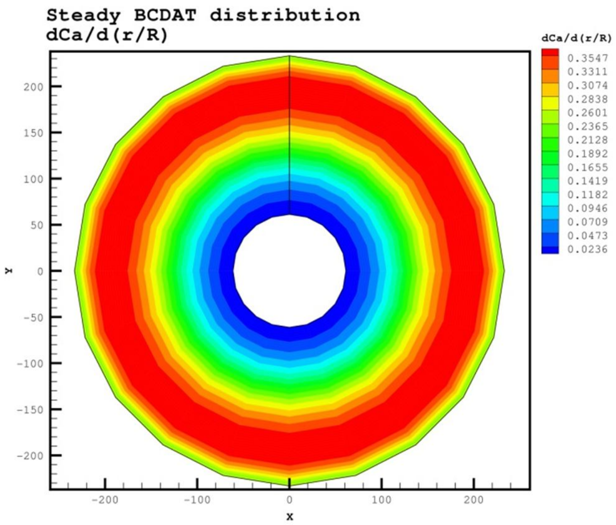

figure 3: 6-blade CESAR steady axial force coefficient distribution

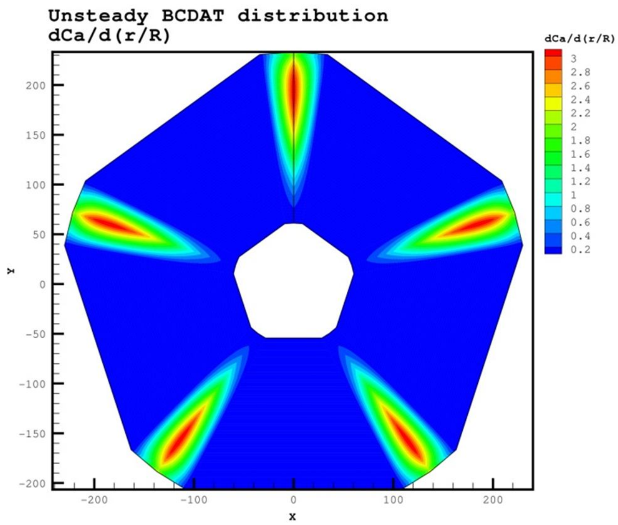

figure 4: 6-blade CESAR unsteady axial force coefficient distribution

A general BCDAT distribution is defined in a polar coordinate system, hence the force coefficient data are function of r and θ. The presence of a propeller in an unsteady BCDAT is simulated by redistributing the force coefficient data on angular sections with size Δ that approximates the propeller blades (figure 5).

As stated earlier, in the transformation from a steady to an unsteady distribution of the AD boundary conditions, it is essential that the quantity of the non-dimensional force coefficients of the unsteady distribution remains equal to that of the steady distribution. To ensure this, the transformation must hold the following integral equation:

$$\int_{Rhub}^{Rtip}\int_{0}^{2\pi}\frac{dC}{d\overline{r}}\overline{r}d\theta d\overline{r}=\sum_{k=1}^{N_p}\int_{Rhub}^{Rtip}\int_{0}^{\Delta}\frac{dC_{\Delta k}}{d\overline{r}}\overline{r}d\theta d\overline{r} \qquad (1.28)$$

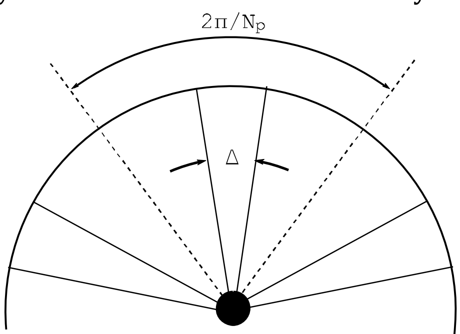

figure 5: visualization of Δ

Where k is the blade index, N_p is the number of blades and $dC_{\Delta k}/d\overline{r}$ is the force coefficient distribution in the section with angular width Δ representing blade k. One way to do this is to split up the disc into N_p parts of angular size $2\pi / N_p$ as depicted in figure 5, i.e. one domain for every blade.

Consider steady BCDAT data for a five blade propeller in i radial positions and $j = n_\theta = 20$ azimuthal positions. For a given radial position, it is then required to integrate over 4 azimuthal positions per blade. The situation is depicted in figure 6. ZEN uses (tri)linear interpolation to project the BCDAT data onto the grid, which means that the data specified on the points at a certain radial position i result in a $\theta-$ distribution of force coefficient data in ZEN depicted by the red line.

Because ZEN uses this (tri)linear interpolation when projecting the BCDAT data onto the grid, a convenient way[1] to express the unsteady boundary condition data distribution in θ for a blade is as a triangle with base width $\Delta\bar{r}(i)$ and height $dC_\Delta(i)/d\bar{r}$. This triangle is positioned at the center of the integration domain at $\theta = \Phi_p$ (the azimuthal position of the center of a blade). This distribution is also depicted in figure 6. The triangle is generated automatically by interpolation in ZEN if the BCDAT file contains for every blade:

- An array of force coefficients on $\theta = \Phi_p$ with values $dC(i)/d\bar{r} = dC_\Delta(i)/d\bar{r}$
- Arrays of force coefficients at $\theta = \Phi_p \pm \Delta/2$ with values $dC(i)/d\bar{r} = 0$

The values of $dC_\Delta\left(i\right)/d\bar{r}$ are calculated from a steady distribution BCDAT file by considering equation (1.28). It is possible to evaluate the integral of $dC(i)/d\bar{r}$ on a line in the domain depicted in figure 5 for the case considered by summation of the quantity Q_C of $dC(i)/d\bar{r}$ of the 4 azimuthal line sections displayed in figure 6.

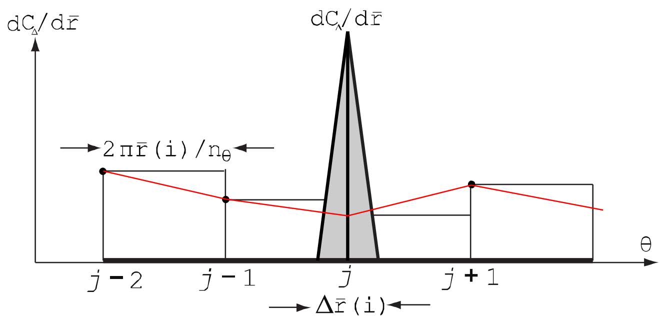

figure 6: triangle distribution slice

The quantity Q_C of $dC(i)/d\bar{r}(i)$ in an arbitrary single line section in figure 6 can be approximated as:

$$Q_C(i,j) = \frac{2\pi\bar{r}\left(i\right)}{n_\theta}\frac{dC(i,j)}{d\bar{r}} \tag{1.29}$$

Evaluation of the integral through the summation of the quantitiy Q_C of the 4 azimuthal positions in this way is equal to evaluating an integral with a left Riemann sum. The Riemann sum evaluation of the integral of an arbitrary smooth and differentiable function $f(\theta)$ over a domain in θ has a maximum error of:

$$E = \frac{1}{2n_\theta}\sup\left(\frac{\partial f}{\partial\theta}\right) \tag{1.30}$$

[1] Other options are also possible; e.g. a step-like function. These however are less computationally stable in UZEN.

which is not particulary accurate. Note however that the used steady boundary condition distribution in this investigation is constant in θ (figure 3) because of test case limitations listed the previous paragraph. Therefore, the error of the sum reduces to zero and its use is justified. For the case of the BCDAT data considered in figure 6, the sum becomes:

$$\sum_{j=-1}^{2} Q_c\left(i,j\right) = \frac{2\pi\overline{r}\left(i\right)}{n_\theta}\sum_{j=-2}^{1}\frac{dC\left(i,j\right)}{d\overline{r}\left(i\right)} \tag{1.31}$$

This must be equal to the amount of quantity Q_c of $dC(i)/d\overline{r}$ present in the triangle distribution, and so:

$$\frac{\Delta\overline{r}\left(i\right)}{2}\frac{dC_\Delta(i)}{d\overline{r}} = \frac{2\pi\overline{r}\left(i\right)}{n_\theta}\sum_{j=-2}^{1}\frac{dC\left(i,j\right)}{d\overline{r}\left(i\right)} \tag{1.32}$$

After rearranging this equation, a relation is obtained for one blade. In general form this is:

$$\boxed{\frac{dC_{\Delta k}(i)}{d\overline{r}} = \frac{4\pi}{n_\theta\Delta}\sum_{j=j_{0,k}}^{j_{0,k}+\frac{n_\theta}{N_p}}\frac{dC\left(i,j\right)}{d\overline{r}\left(i\right)}}$$

This is to be done for all blades present. After this, integration over $\overline{r}$ will satisfy equation (1.28).

2.4.3. Definition of Δ

The only variable used that hasn't been defined yet in a quantitive way is the angular size of the unsteady boundary condition data distribution, Δ. Because little is known about the influence of this parameter on the unsteady flow solution, its size will be investigated. As a reference, Δ is constructed for all blades investigated in this report in the same following way:

Consider a rotor blade like the one depicted in figure 7 and assume that the local chord distribution is known. The average chords is calculated as:

$$c_m = \frac{1}{R_{tip}}\int_{R_{hub}}^{R_{tip}} c\left(r\right)dr \tag{1.33}$$

With the average chord, the blade surface area can easily be calculated as $A = c_m\left(R_{tip} - R_{hub}\right)$. Furthermore, the surface area of an azimuthal section with angular width Δ is:

$$A = \int_{R_{hub}}^{R_{tip}}\int_{0}^{\Delta} r dr d\theta = \frac{\Delta}{2}\left[R_{tip}^2 - R_{hub}^2\right]$$

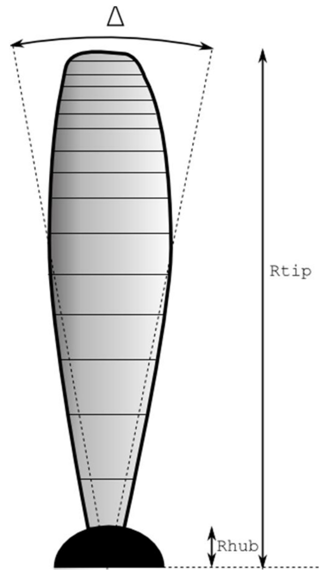

figure 7: Δ construction

Now Δ is defined by substituting the equation for blade surface area into equation (1.33) :

$$\boxed{\Delta = \frac{2c_m\left(R_{tip} - R_{hub}\right)}{R_{tip}^2 - R_{hub}^2}}$$

This defines Δ as a function of the surface of the blade. Note that this is only a definition. It is unknown whether or not Δ has to somehow incorporate geometry of the propeller in order to accurately simulate the flow. This will be investigated in this report.

2.5. Expected effects of the use of Unsteady ZEN

The use of the unsteady boundary condition as defined in the previous paragraph can be a source of effects not present in a steady simulation. These effects are explained below.

2.5.1. Increased artificial dissipation

The higher concentrations of force coefficients that are present in an unsteady boundary condition (BCDAT) file in ZEN result in high gradients of flow field variables around the actuator disk, inducing wiggles in the solution process of the (Euler) flow. This is the major source of numerical instability. Because of the quasi-second order Jameson like scheme used by UZEN, the calculation is made convergent by the use of dissipative terms. These terms in the numerical scheme make sure that the solution is smoothened out during the solving process. Basically, this is done by averaging the high gradients in momentum between neighboring cells in such a way that the scheme remains stable enough. However, because energy is conserved, this means that kinetic energy is transformed into internal energy.

In the analysis of the UZEN output, the total pressure is chosen as a way to measure the momentum in the flow. Because of the reasons explained above, it can be expected that the introduction of the unsteady force coefficient distribution will result in a drop in total pressure, increasing in magnitude with decreasing Δ. Further in depth detail on the Jameson scheme is included in appendix I.

Because of the redistribution of force coefficient data from a steady distribution to an unsteady one, a more or less physical phenomenon is occurring. To illustrate this, we consider a simplified distribution of force coefficients using four cells with a certain dimension:

$\Delta(\rho\|\|\bar{u}\|\|)$	$\Delta(\rho\|\|\bar{u}\|\|)$	$\Delta(\rho\|\|\bar{u}\|\|)$	$\Delta(\rho\|\|\bar{u}\|\|)$

figure 8

These cells introduce an increase of momentum of $4*\rho|\vec{u}|^2$. As was stated in paragraph 2.3, the pressure increases linearly with axial momentum added at the BC. Therefore, the total enthalpy increase in the flow will be:

$$\Delta H = 4\Delta\left(\frac{P}{\rho}\right) + 4\Delta\left(\frac{1}{2}\left\|\frac{(\Delta\rho V_\theta)+(\Delta\rho V_r)}{\rho}\right\|^2\right)$$

When the force coefficient data is redistributed to one cell while ensuring that the added momentum stays constant, the situation of figure 9 occurs:

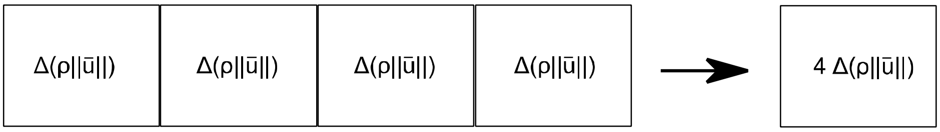

figure 9

While the amount of added momentum stays equal to the initial situation, the total enthalpy does not because the force coefficients inducing the increase in momentum are present on a smaller area. This causes an increase of total enthalpy of:

$$\Delta H_{new} = 4\Delta\left(\frac{P}{\rho}\right) + \left(\frac{1}{2}\sqrt{\left(4\frac{\Delta(\rho V_\theta)}{\rho}\right)^2 + \left(4\frac{\Delta(\rho V_r)}{\rho}\right)^2}^{\,2}\right) > 4\Delta H$$

The same phenomenon is occurring when a steady ZEN boundary condition distribution is redistributed for UZEN use in the way described in paragraph 2.4. Therefore, it can be expected that the total enthalpy, measured by the total temperature in the results of an analysis, will grow when the force coefficient distribution is made denser, i.e. when Δ is made smaller.

3. CESAR test case

In order to test the ZEN solver and to create a set of reference data, a simple test case is devised. In this chapter the actuator disk boundary condition data generated in the CESAR (Cost Effective Small AiRcraft) project is used to make a steady run in ZEN. The exact data used is obtained from the DLR URANS computation for the project and averaged over θ in order to be applicable for the test setup. The results of this test case are to be used as a reference for the validation of the unsteady ZEN solver later on. The objective is the obtain results of simulations of an isolated propeller with a dummy nacelle under 0 angle of incidence with the free stream.

An Euler simulation is carried out on both a fine and a course grid. This is done in order to establish the amount of smoothening that takes place when ZEN interpolates the boundary condition data onto the mesh and in which fashion this influences the resulting flow.

Because the unsteady ZEN method described in chapter 2 can only use ZEN's force model for actuator discs, also for the steady run the force model is used and the input data consists of the local thrust coefficient $\frac{dCa}{d\bar{r}}$, the local power coefficient $\frac{dCp}{d\bar{r}}$, and the local radial force coefficient $\frac{dCr}{d\bar{r}}$, which are defined according to the definitions given in appendix II. The used boundary condition distribution is depicted in figures figure 10, figure 11 and figure 12.

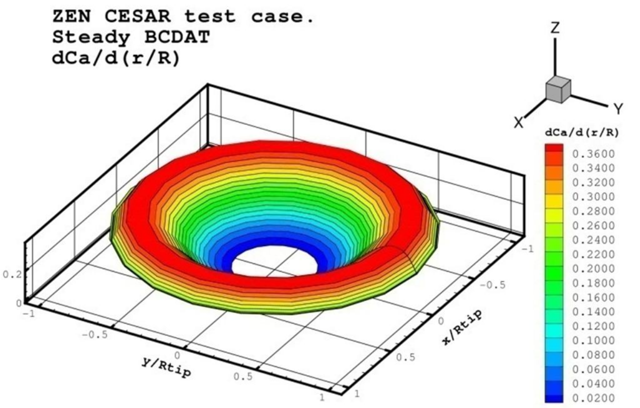

figure 10: steady CESAR axial force coeffient distribution

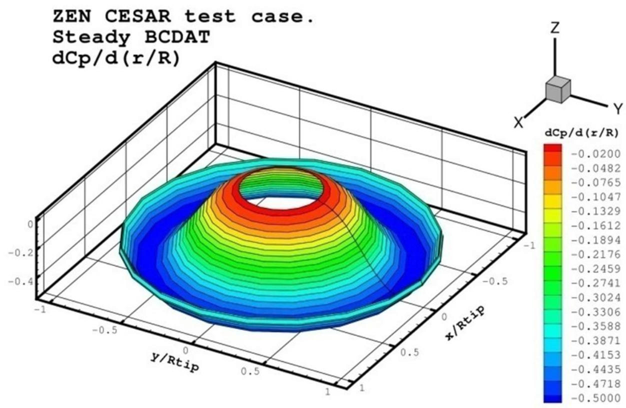

figure 11: steady CESAR power coeffient distribution

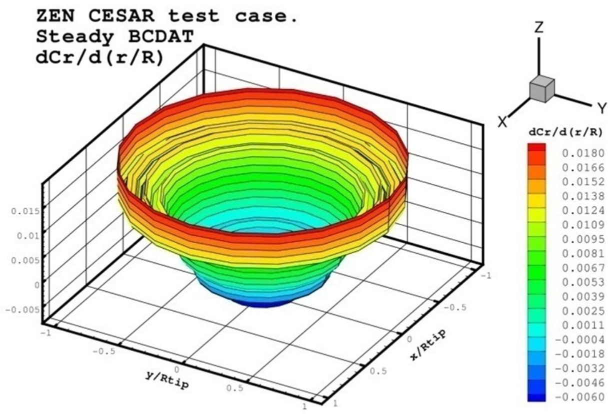

figure 12: steady CESAR radial force coeffient distribution

3.1.1. Test setup

The steady tests are conducted in ZEN and solved for Euler flow: effects of viscosity and thermal conductivity are neglected. Input parameters are:

Free stream Mach number:	0.235
Advance ratio:	1.101
R_{tip}	0.235 m
R_{hub}/R_{tip}:	0.2602
Angle of incidence α:	0°

3.1.2. Geometry

A dummy nacelle is used in the test in order to obtain lift, drag and side force data. The used geometry is depicted in figure 13. The actuator disk is located at $\overrightarrow{x_c} = (0,0,0)$.

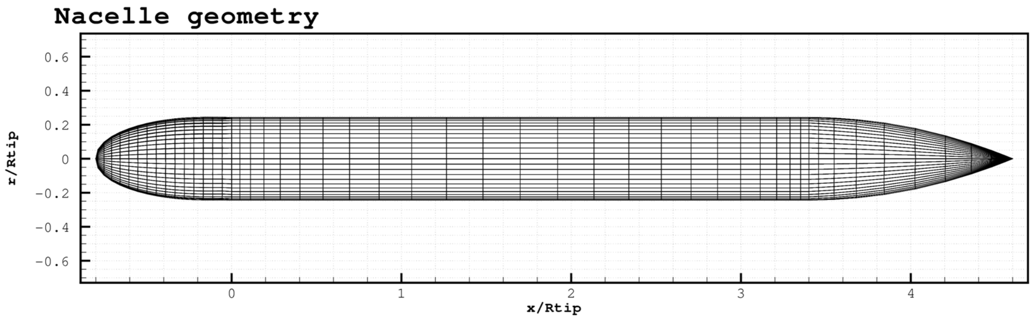

figure 13: nacelle geometry

3.1.3. Mesh

The mesh used for the CESAR propeller test case is a structured grid consisting of 24 blocks. The block structure is depicted in figure 14. In figure 15 the far field blocks are not shown, and the focus is on the block structure around the highlighted nacelle.

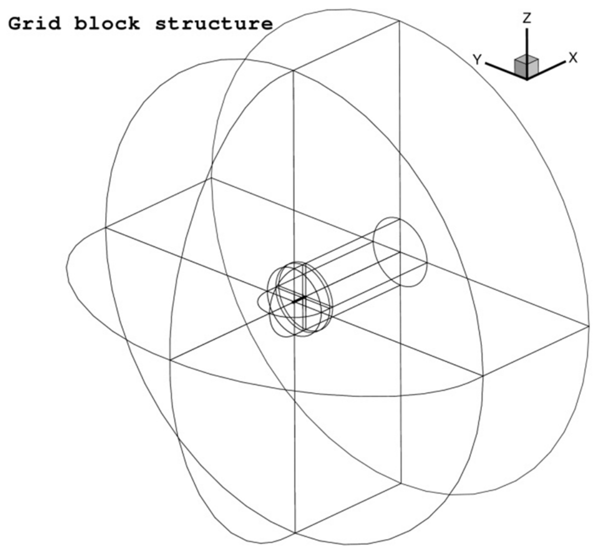

figure 14: Grid block structure

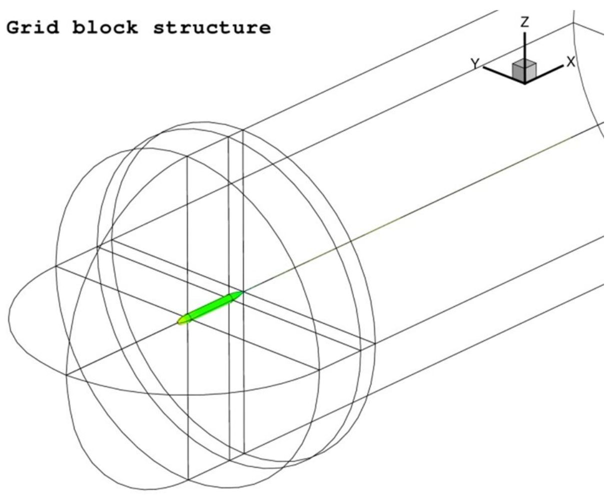

figure 15 Grid block structure detail

Furthermore, figure 16 shows the coarse mesh of cell centers in the ZX plane where y=0 and reveals the structure of the cells in downstream direction, while figure 17 and figure 18 reveal the cell structure of the mesh in the ZY plane just after the actuator disk and just after the nacelle respectively. The dense mesh has the same block and vertice structure as the coarse grid, but consists of twice as many cells in all directions.

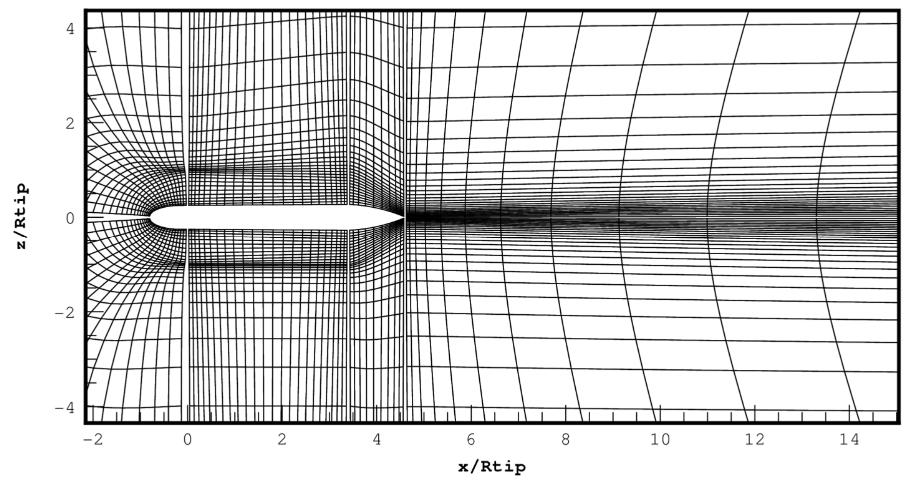

figure 16: Coarse grid cell density (ZX plane)

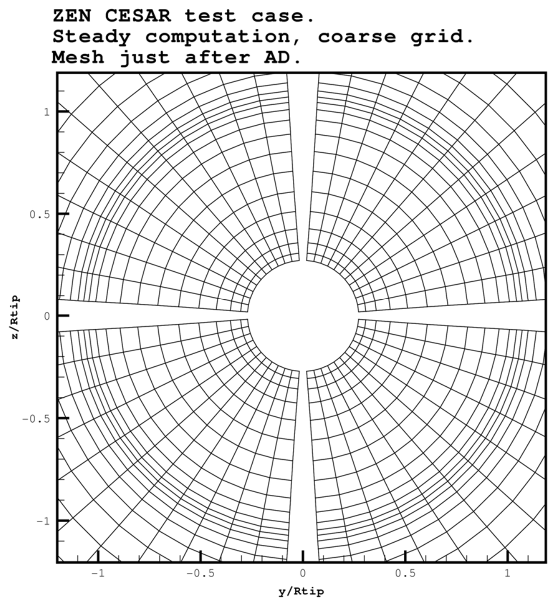

figure 17: Coarse grid cell density just after the AD (ZY plane)

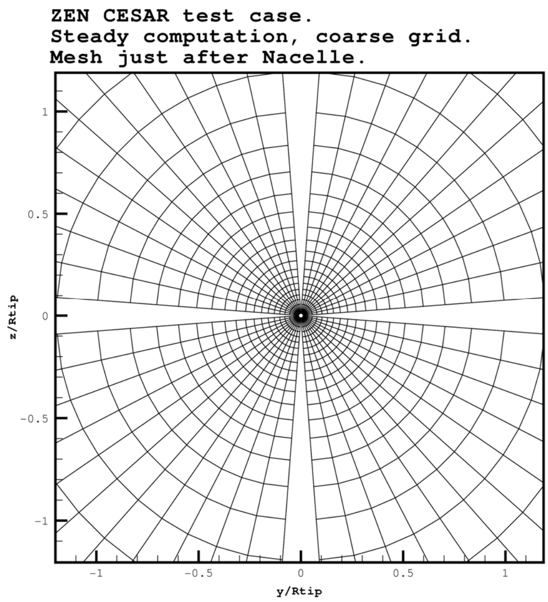

figure 18: Coarse grid cell density just after the nacelle (ZY plane)

3.2. Steady results

3.2.1. Convergence

Figures figure 19 and figure 20 show the convergence history of the run on the coarse mesh and the dense mesh respectively, by the residual of the root mean square of the continuity equation together with the maximum residual of the continuity equation. For both simulations, the residual decreases steadily. However, as can be expected, the residual of the simulation on the coarse mesh decreases more rapidly because of the smaller amount of equations needed to be solved.

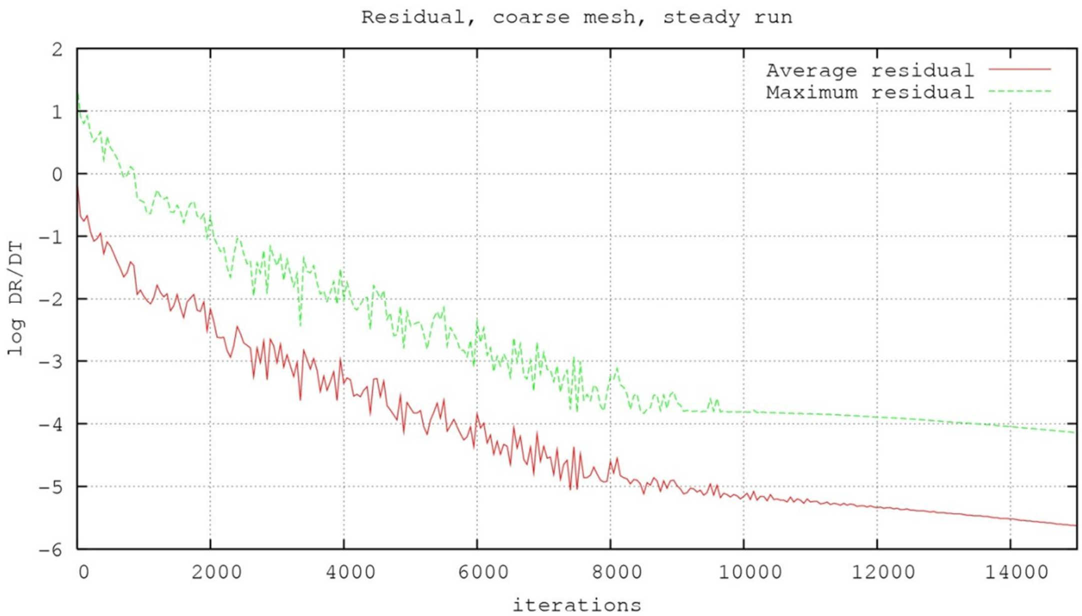

figure 19: Residual plot: CESAR test-case steady coarse grid run

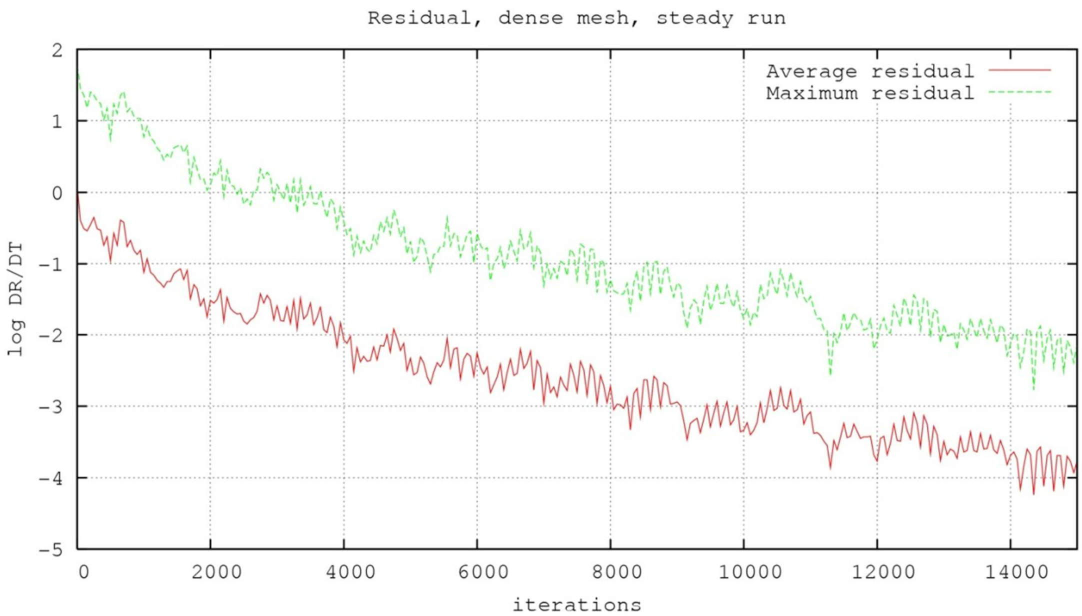

figure 20: Residual plot: CESAR test-case steady dense grid run

Below the results obtained for both simulations are depicted. The output given has been non-dimensionalized by the following convention:

$$T0 = T_t / T_\infty,\ P0 = P_t / P_\infty$$

Where T_t is the total temperature and P_t is the total pressure. Furthermore, the values with the infinity subscript are the quantities of the temperature and pressure in the undisturbed section of the flow field.

3.2.2. Coarse grid results

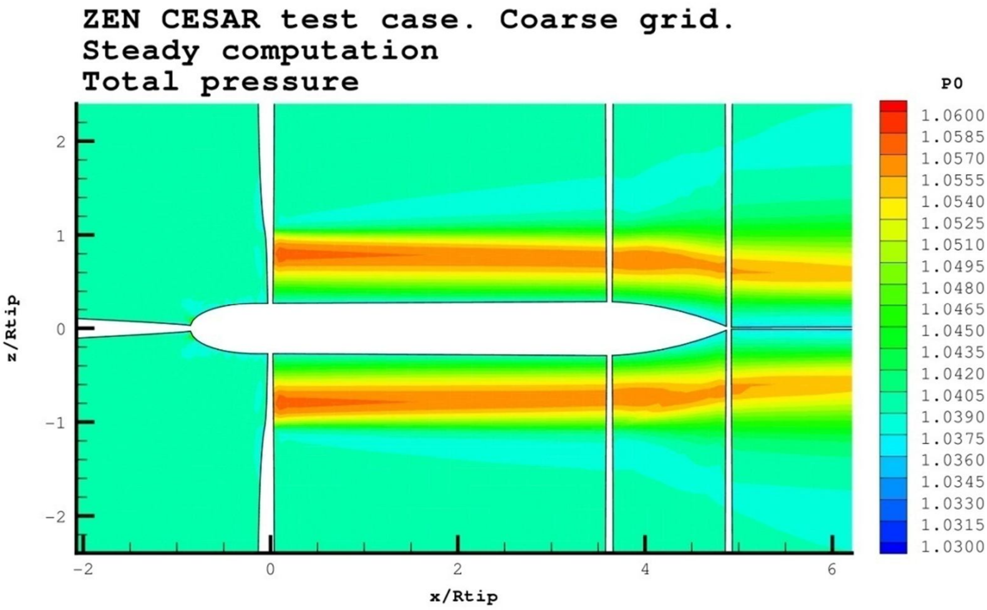

figure 21: Coarse grid run: Total pressure(ZX plane)

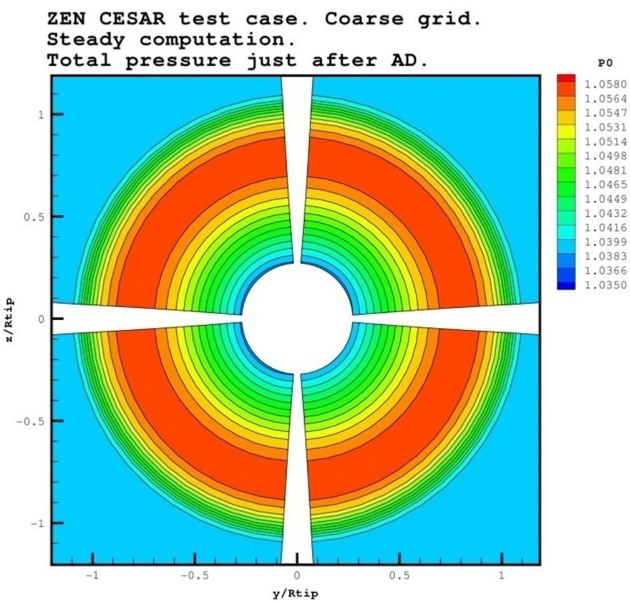

figure 22: Coarse grid run: Total pressure (ZY plane, just after the nacelle)

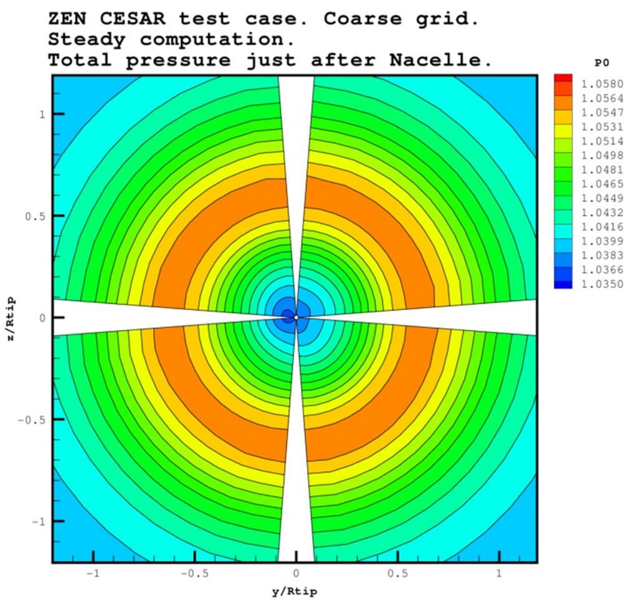

figure 23: Coarse grid run: Total pressure (ZY plane, just after the nacelle)

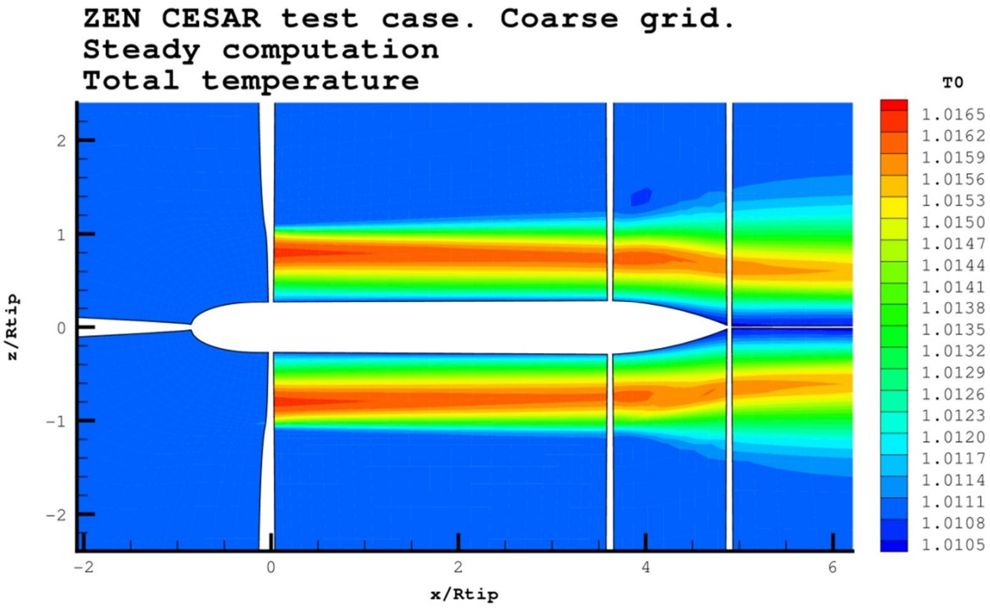

figure 24: Coarse grid run: Total temperature (ZX plane)

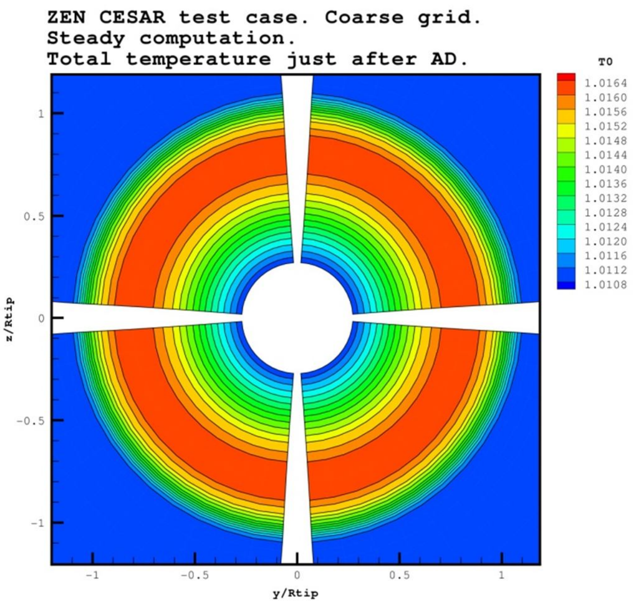

figure 25 : Coarse grid run: Total temperature (ZY plane, just after the AD)

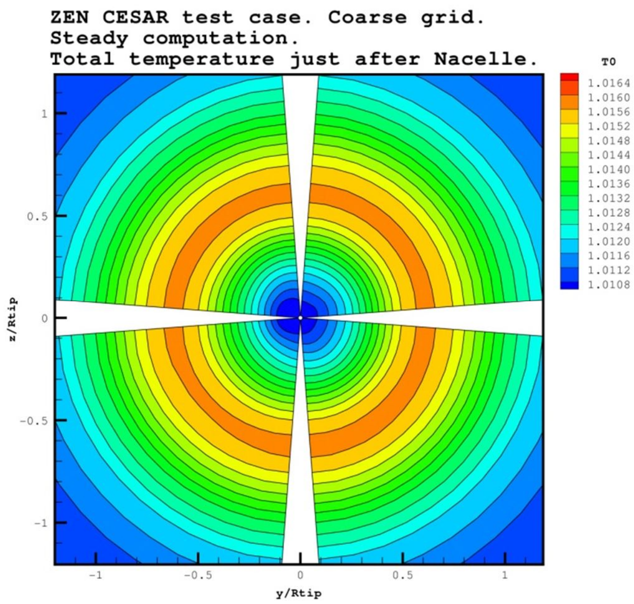

figure 26: Coarse grid run: Total temperature (ZY plane, just after the nacelle)

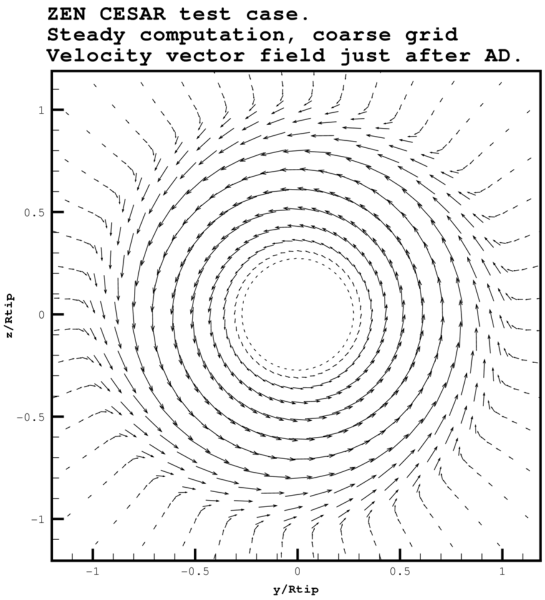

figure 27: Coarse grid run: velocity vector field(ZY-plane, just after the AD)

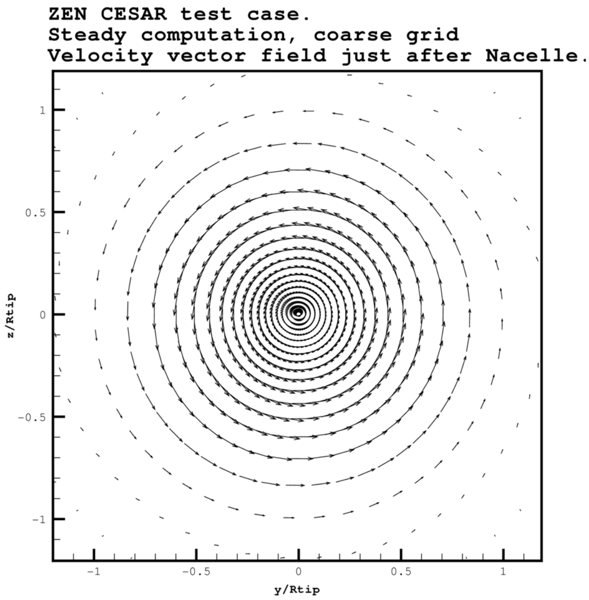

figure 28: Coarse grid run: velocity vector field(ZY-plane, just after the AD)

The simulation performed as expected and works according to the theory in paragraph 2.2. The total pressure increase induced by the axial force coefficient distribution on the boundary condition accelerates the flow in downstream direction after the actuator disk. The radial force coefficient adds contraction to the flow just after the actuator disk as can be seen in figure 21, while the power coefficient induces swirl, which is shown in figure 27. Furthermore, the flow expands diffuses after the actuator disk while moving downstream, which results in the total pressure- and temperature distribution of figure 23 and figure 26 respectively.

3.2.3. Dense grid results

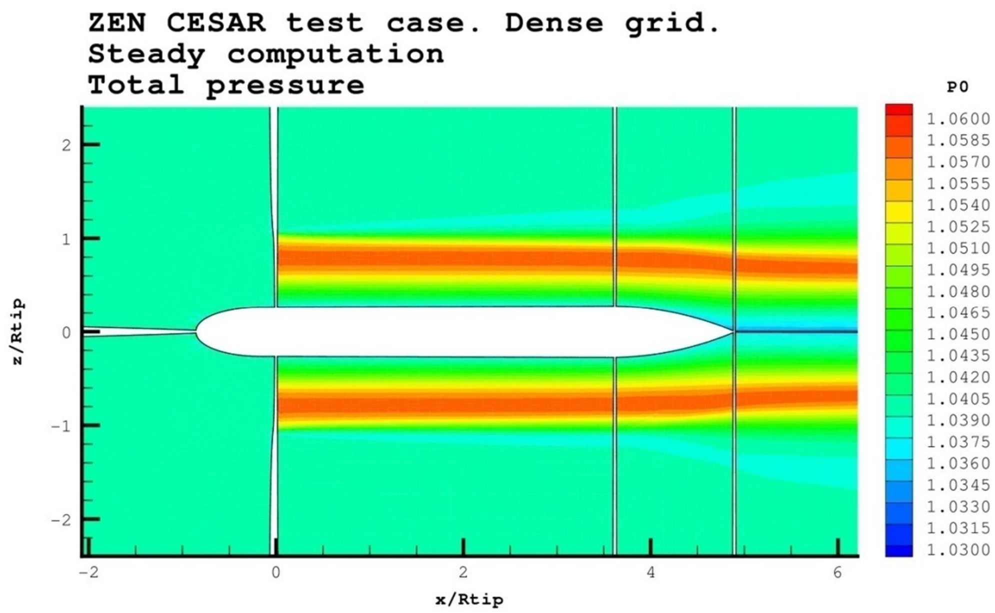

figure 29: Dense grid run: Total pressure(ZX plane)

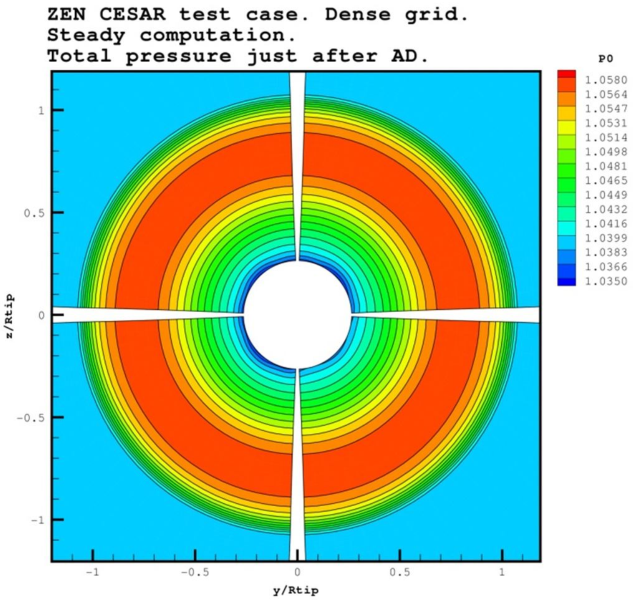

figure 30: Dense grid run: Total pressure (ZY plane, just after the AD)

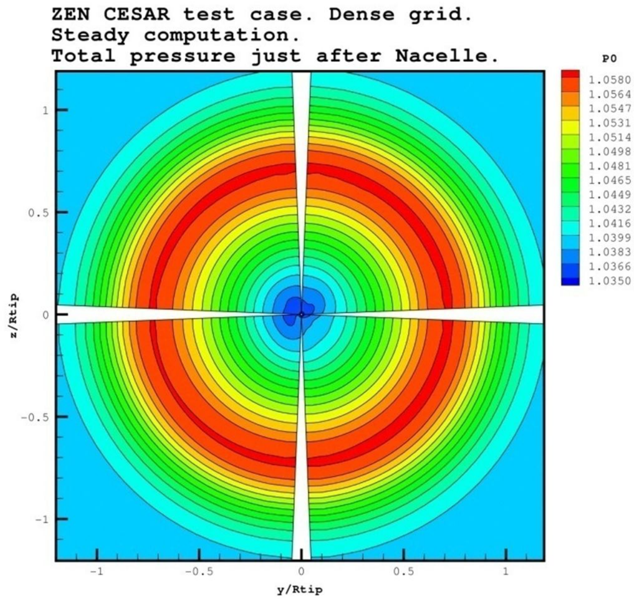

figure 31: Dense grid run: Total pressure (ZY plane, just after the nacelle

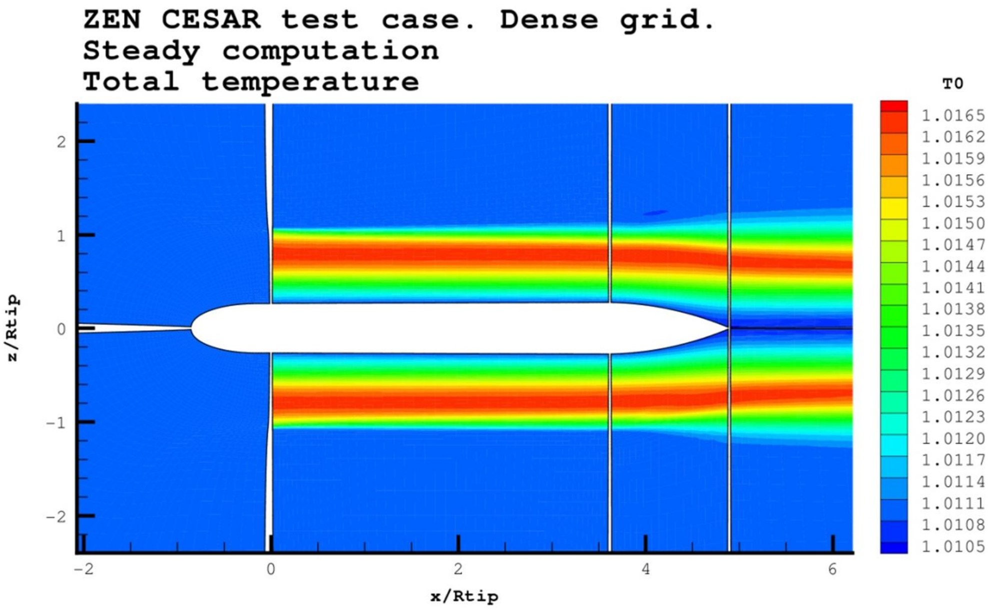

figure 32: Dense grid run: Total temperature(ZX plane)

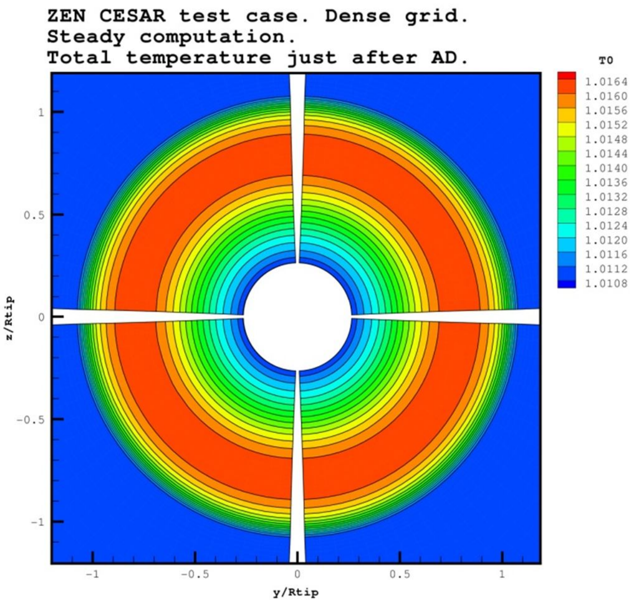

figure 33: Dense grid run: Total temperature (ZY plane, just after the AD)

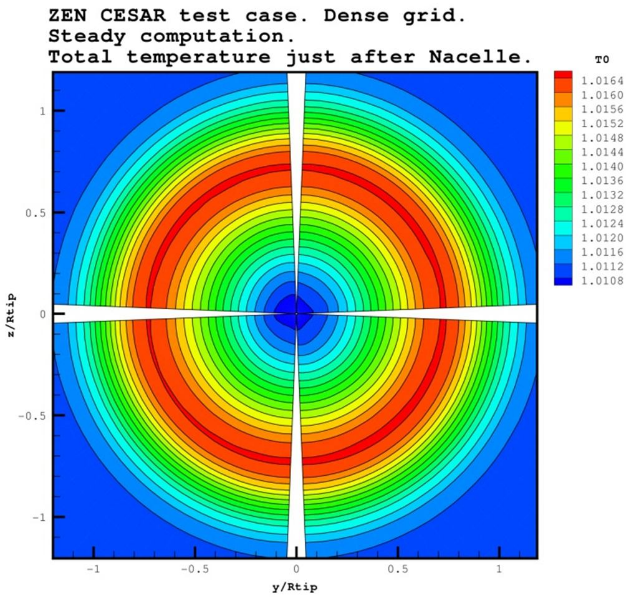

figure 34: Dense grid run: Total temperature (ZY plane, just after the nacelle)

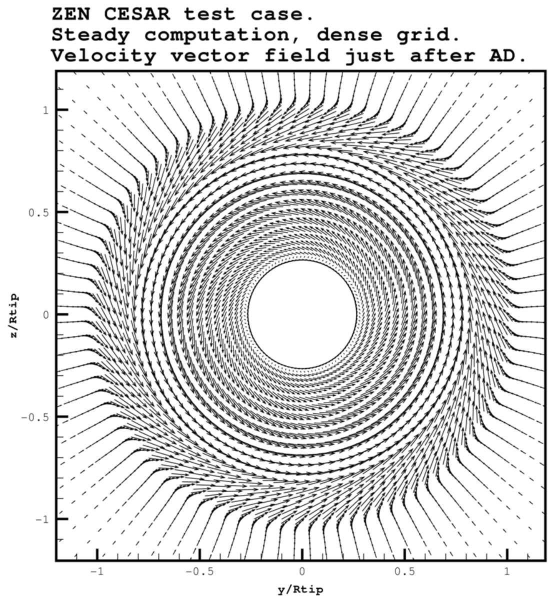

figure 35: Dense grid run: velocity vector field(ZY-plane, just after the AD)

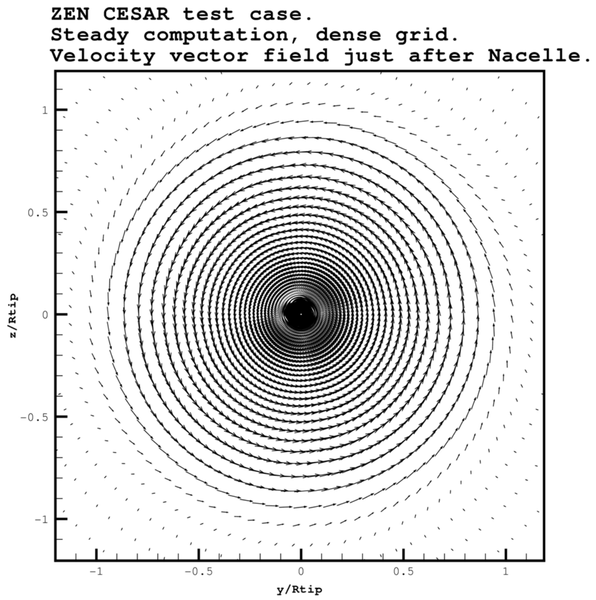

figure 36: Dense grid run: velocity vector field(ZY-plane, just after the nacelle)

The results of the ZEN run on the dense grid show similar results just after the actuator disk in comparison with the run on the coarse grid. However, after the nacelle the flow is more compact. Also, the concentration of total pressure induced at the actuator disk remains concentrated more. The expansion occurring in the run of the coarse grid is therefore dependent on mesh resolution. The reason why this phenomenon is occurring is the smoothening between grid points due to artificial dissipation. A description of this phenomenon is explained in paragraph 2.5.

In contrast to total pressure, ZEN conserves the amount of total enthalpy and thus total temperature. This means that the total temperature profile can be used as a way to measure the amount of artificial diffusion due to mesh density. The effect is clearly visible when comparing figure 26 to figure 34. It is difficult to quantify the results properly, but we know from appendix I, that the order of magnitude of artificial dissipation is of $O(\Delta x^3)$. Since our comparison is between a grid with Δx and a grid with $\Delta x / 2$, we expect the maximum difference to be $(1/2)^3 * 100\% = 12.5\%$ between the solutions of the dense and the coarse grid respectively. When we compare the coarse grid total temperature to the dense grid total temperature, we find a maximum difference of

$$\frac{\max|_{dense} - \max|_{coarse}}{\max|_{dense} - \min|_{dense}} * 100\% = \frac{1.0164 - 1.0158}{1.0164 - 1.0105} * 100\% = 10.2\%$$

If we assume that the simulation of the dense mesh comes very close to the exact solution, this agrees with the theory and therefore, the artificial diffusion is working as expected.

It should be noted that both for the run on the dense and the coarse grid, the flow is slightly non axial symmetric. Investigation of the 4th quadrant of the ZY plane just after the actuator disk reveals a small defect in the amount of total pressure and induced horizontal velocity near the nacelle. A closer look at the nacelle gives an explanation:

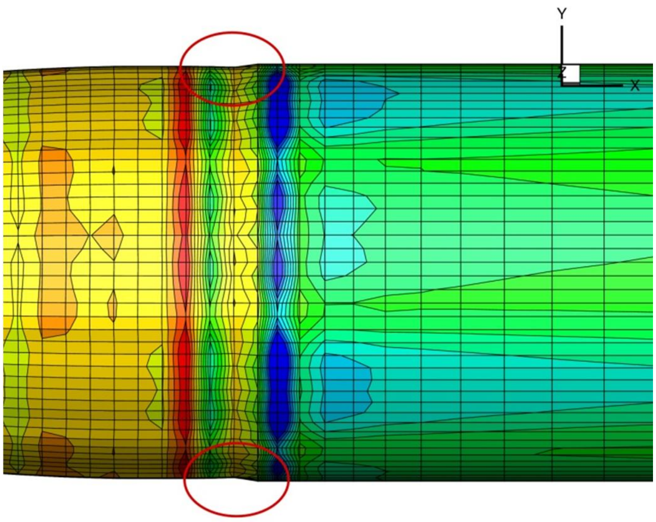

figure 37: Mesh defect

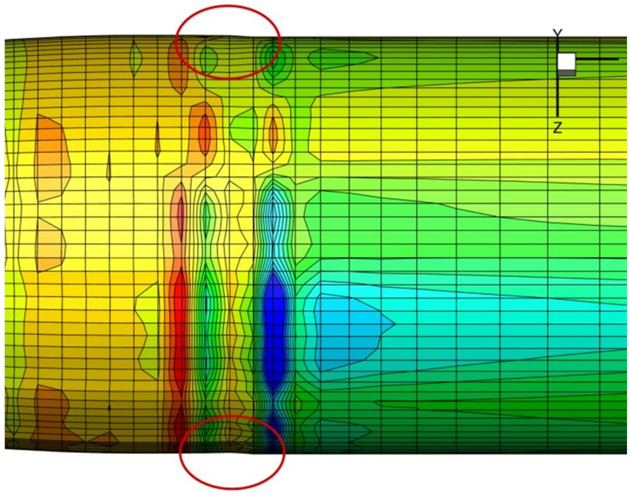

figure 38: Mesh defect(cont.)

figure 37 and figure 38 show a detailed view of the nacelle. The flooded areas represent the total pressure distribution. Inside the red circles in figure 37, it can be seen that the geometry is not completely straight in x-direction, i.e. it has a slight kink at the position of the actuator disk. Comparing this to figure 38, it can be seen that the mesh surface representing the nacelle is not axisymmetric at all. The position of the bump in figure 38 is on the same azimuthal position as the position of the different total pressure distribution on the nacelle after the actuator disk. Therefore it can be assumed that this geometric imperfection is the cause of the non-axisymmetrical total pressure distribution near the nacelle. To solve this, mesh refinement is needed. Because of the short duration of the study, this was impossible to do. However, because the resulting flow is only affected in a small way we continue the study with this mesh and see whether or not the effect is neglible.

3.3. Unsteady results

For the same CESAR test case, an unsteady run has been done with UZEN. The time averaged mean flow is used as a platform to measure the differences with a steady ZEN run to investigate the effects of the unsteady force coefficient distribution. This is measured just at the position just after the nacelle, which is some distance after the actuator disk where the effects are more visible than just after it. Also, in order to test to what extent grid density affects the aerodynamic solution of the unsteady computations, a series of comparisons have been done between the steady solution of the flow just after the nacelle of the CESAR test case is and the mean flow of its unsteady computation on both grids.

To examine the effects of smoothening of high gradients in momentum, another test is done using a distribution where Δ is half its size. In order to visualize the effects, plots are made of the difference in result.

The tests are conducted on the grid displayed in paragraph 3.1.3 for both a dense mesh and a coarse mesh, where the latter has half as many cells in every direction.

3.3.1. Coarse grid results

The convergence of the simulation on the coarse grid with $\Delta = 16.8^{\circ}$ depicted in the figures below:

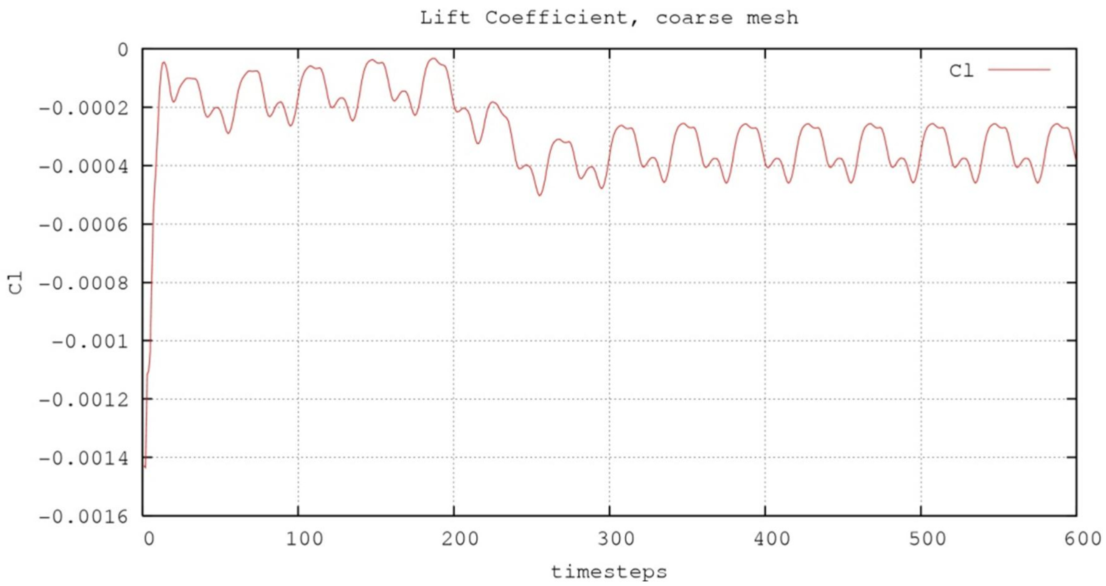

figure 39

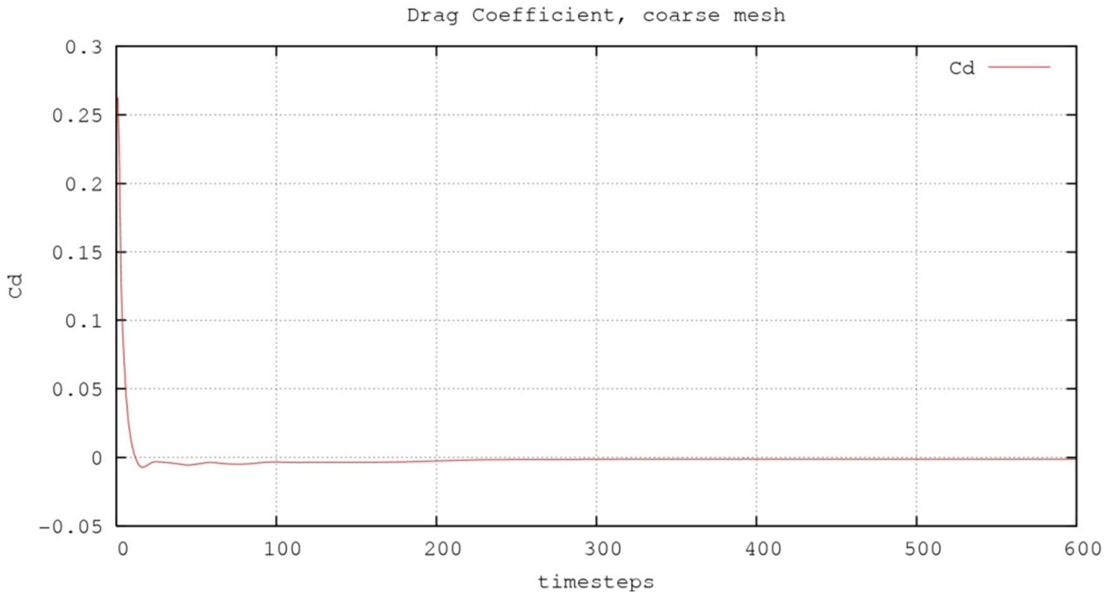

figure 40

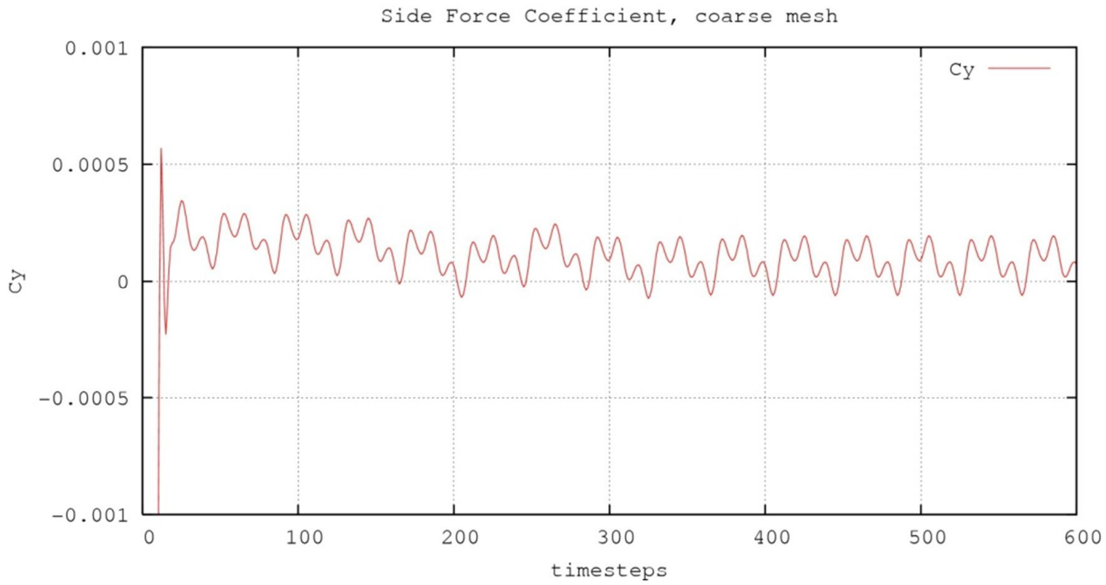

figure 41

From figures 39 to 41, it can be seen that the solution starts to oscillate in a steady manner. This is sufficient proof that the solution converges. Note that the side and lift force coefficient are not oscillating around zero. This is due to the mesh defect described in paragraph 3.2.

Total pressure

Comparing the plots of the total pressure distribution just after the nacelle, the first observation is that little effect of smoothening on the unsteady solution is taking place. In figure 45 the difference is plotted between the steady and the unsteady solution with Δ=16.8°. There is a maximum near the center of the mesh that is likely a result of the mesh imperfections discussed in paragraph 3.2. The maximum difference in the other area is around 0.0002, and this is

$$\frac{0.0002}{1.058-1.035}*100\% = 0.9\%$$

of the maximum total pressure increase.

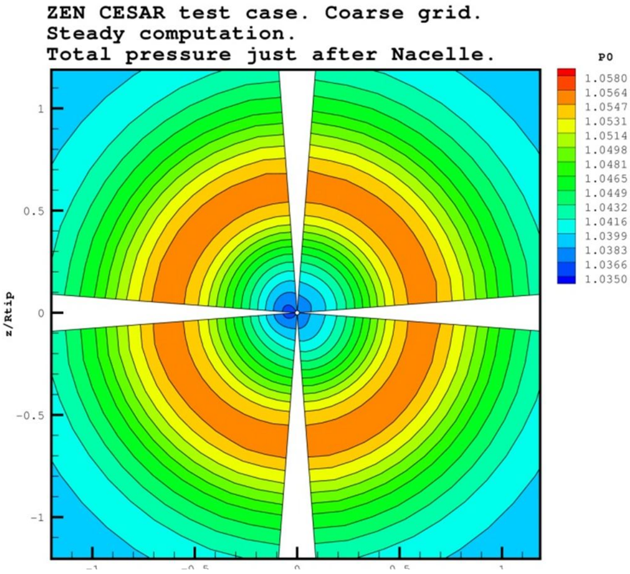

figure 42: P0: steady

The differences between the mean flow of the computation with Δ=16.8° and the computation with Δ=8.4° are somewhat larger, however still relatively small. The maximum difference is 0.0004 and this is:

$$\frac{0.0004}{1.058-1.035}*100\% = 1.7\%$$

of the maximum total pressure increase. What also is visible in figure 46 is the effect of the block structure of the mesh. Because the same error is visible in every quadrant while the propeller has five blades, it is likely that an interpolation error is occurring.

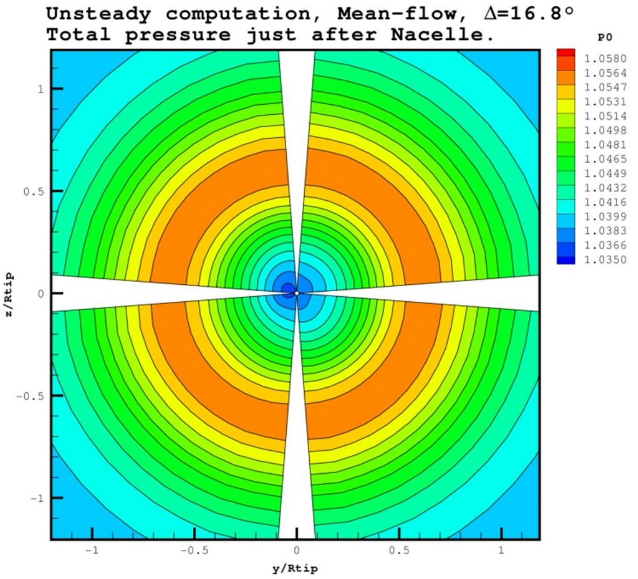

figure 43: P0: unsteady (Δ=16.8)

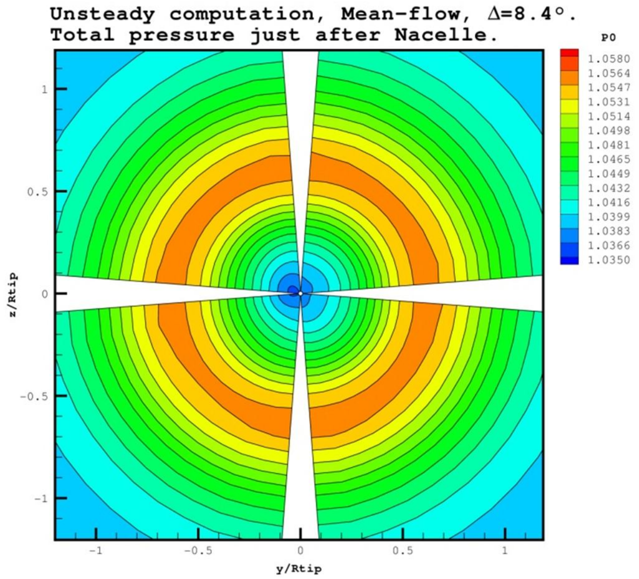

figure 44: P0: unsteady (Δ=8.4)

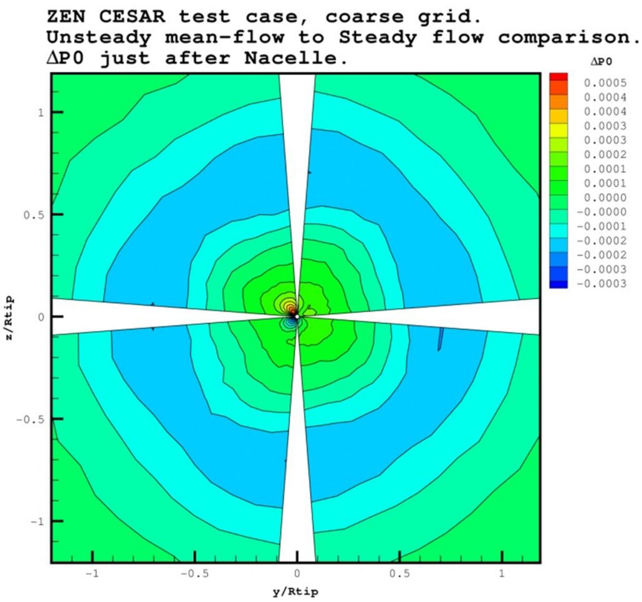

figure 45: ΔP0: steady – unsteady(Δ=16.8)

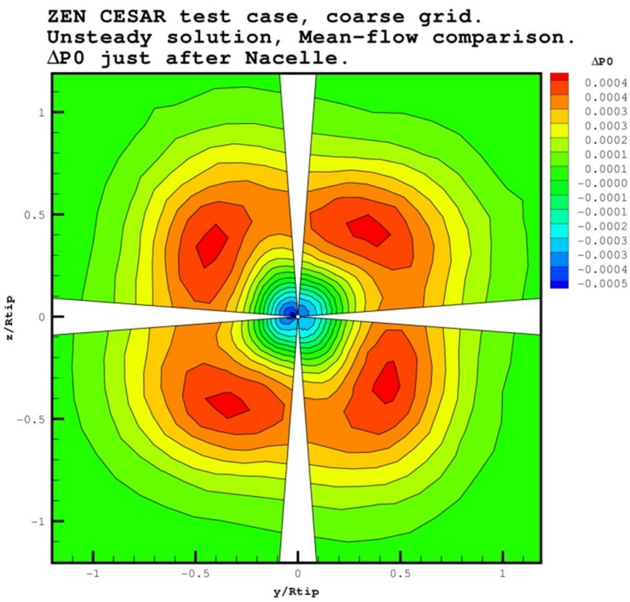

figure 46 ΔP0: unsteady(Δ=16.8) – unsteady(Δ=8.4)

Total temperature

Comparing figure 47, figure 48 and figure 49 reveals an influence of Δ. The mean flow of the unsteady distributions shows an increase of total temperature and thus total enthalpy with decreasing Δ. This phenomenon is to be expected as was explained in paragraph 2.5. figure 50 reveals a difference between the steady and unsteady solution that is

$$\frac{0.0005}{1.0164-1.0105}*100\% = 8,5\%$$

of the maximum increase in total temperature.

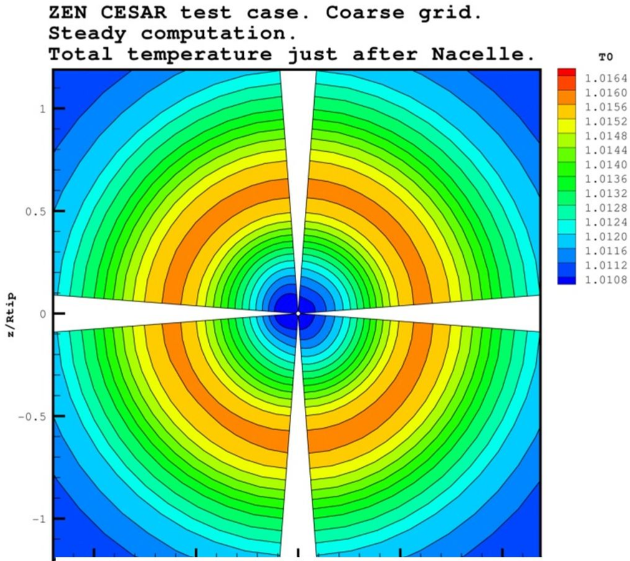

figure 47: T0: steady

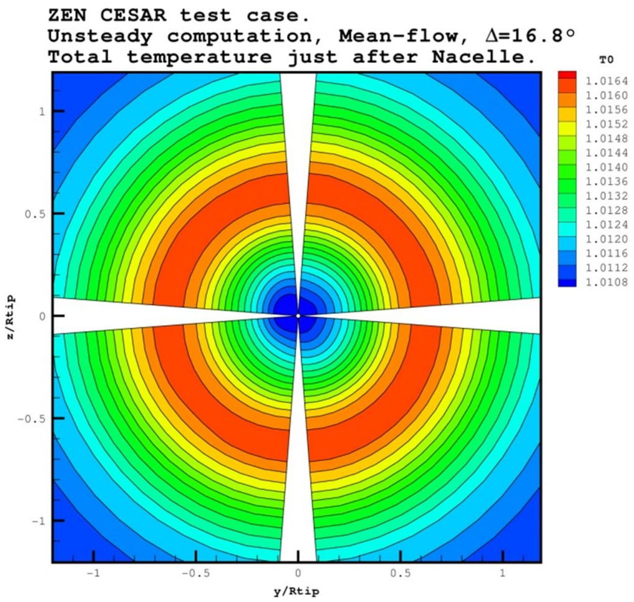

figure 48: T0: unsteady (Δ=16.8)

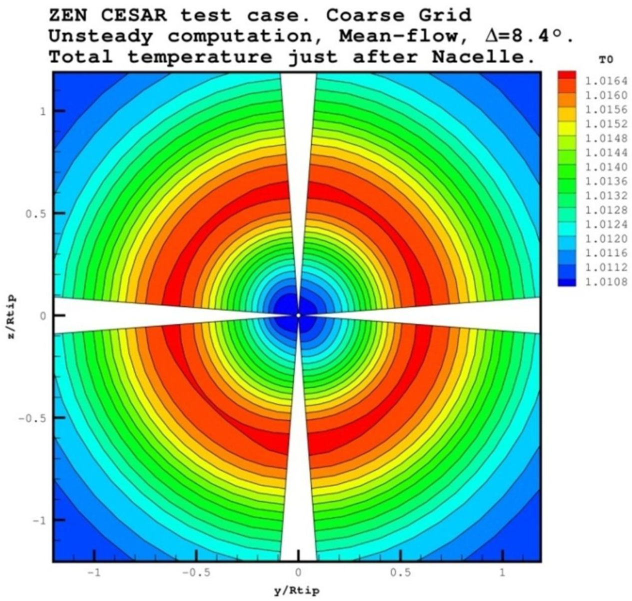

figure 49: T0: unsteady (Δ=8.4)

The difference between the mean-flow of the unsteady computation with Δ=16.8° and the computation with Δ=8.4° is, according to figure 51.

$$\frac{0.0003}{1.0164-1.0105}*100\%=5.1\%$$

of the maximum increase of the total temperature. Again, the comparison of the mean flow of the two unsteady cases reveals an error that seems to have a connection to the mesh block structure.

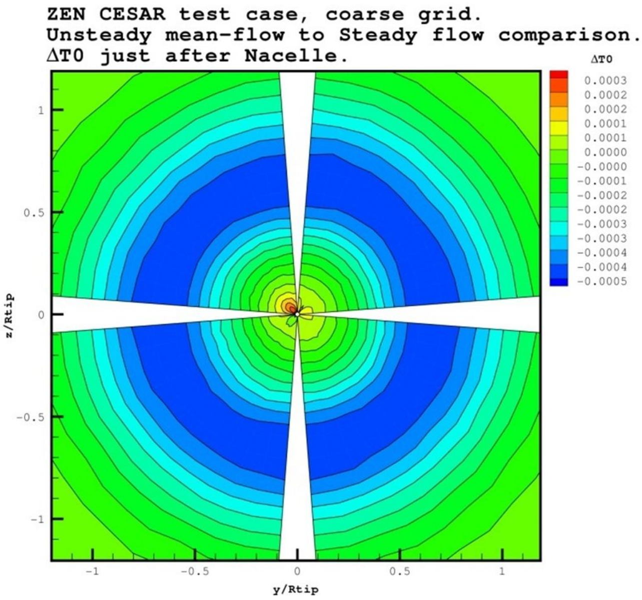

figure 50: ΔT0: steady – unsteady(Δ=16.8)

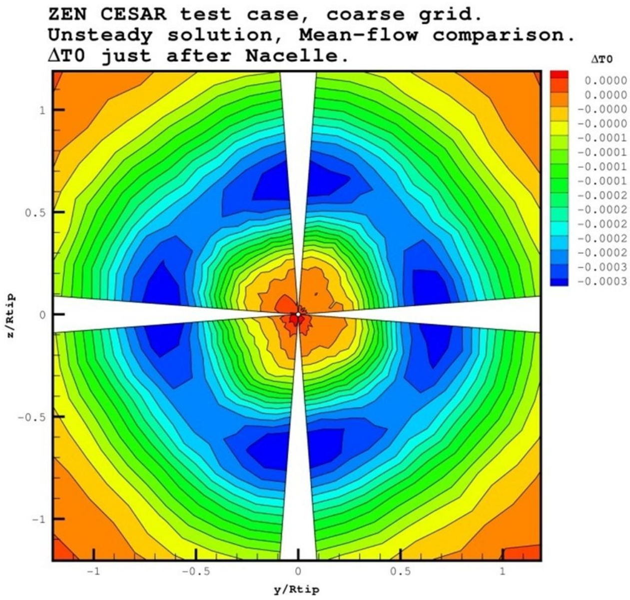

figure 51: ΔT0: unsteady(Δ=16.8)– unsteady(Δ=8.4)

3.3.2. Dense grid results

The convergence of the simulation on the coarse grid with $\Delta = 16.8^{\circ}$ depicted in the figures below:

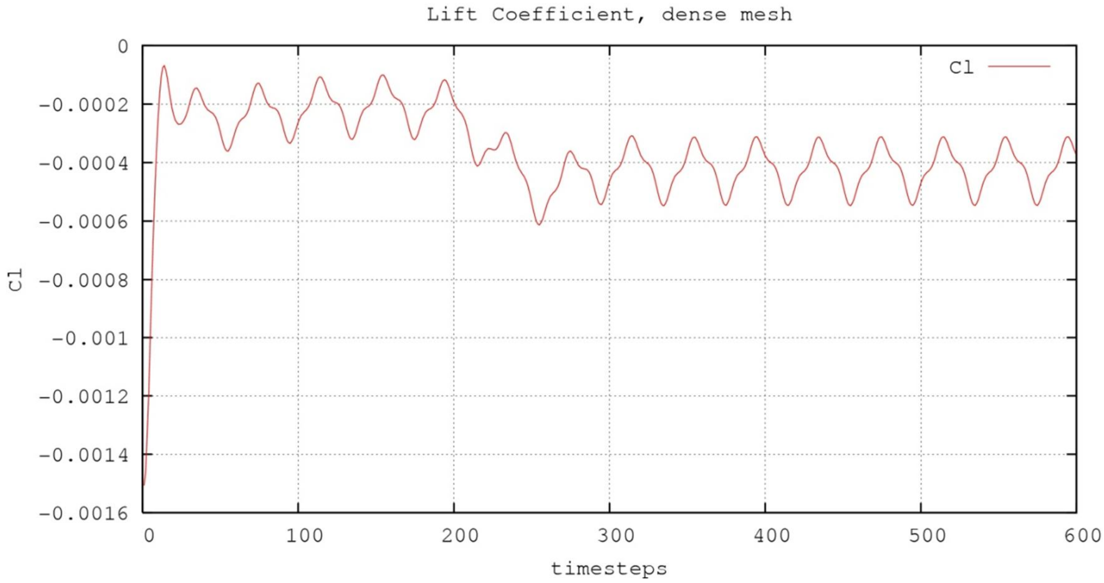

figure 52

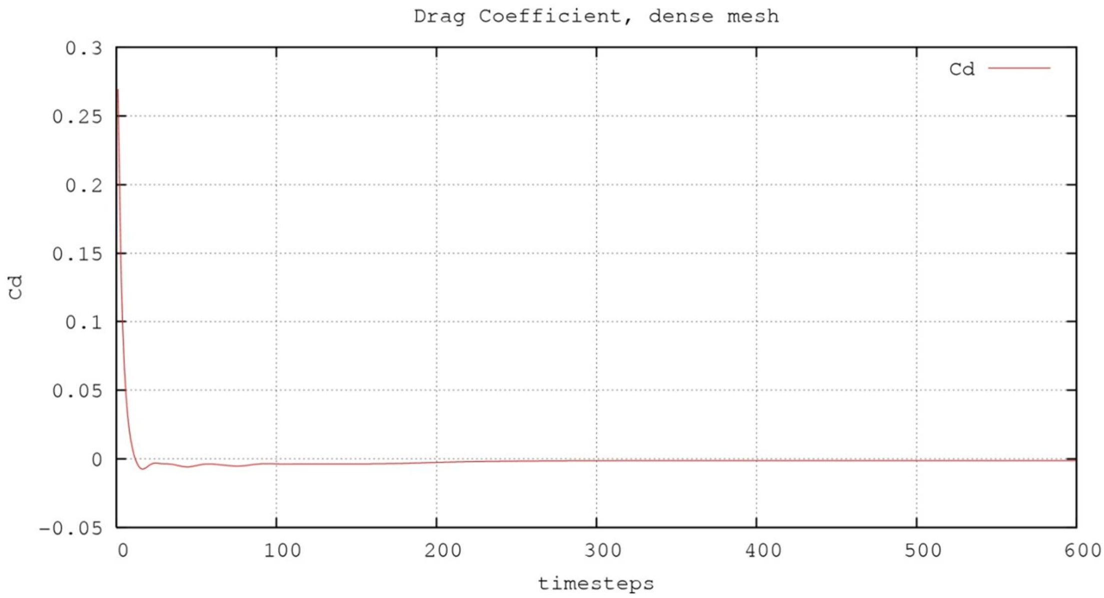

figure 53

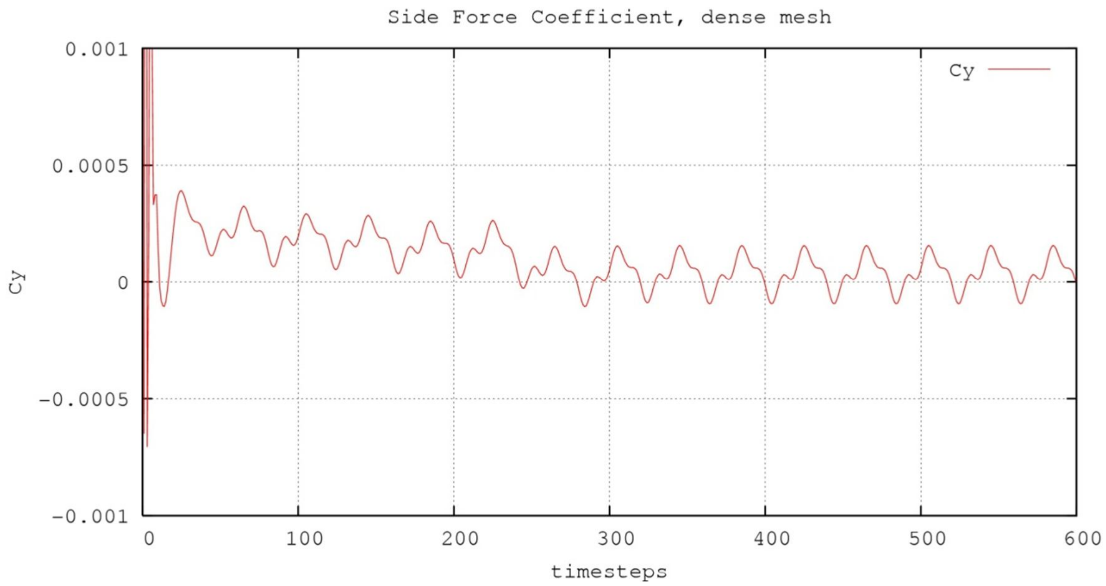

figure 54

Also for the dense mesh, it can be seen in figures 52 to 54 that the solution starts to oscillate in a steady manner. This is sufficient proof that the solution converges. Again the side and lift force coefficient are not oscillating around zero. This is due to the mesh defect described in paragraph 3.2.

Total pressure

Comparing the plots of the total pressure distribution just after the nacelle on the dense grid, it can be concluded that there is again little effect of smoothening. In figure 58 the difference is plotted between the steady and the unsteady solution with Δ=16.8°. There is again a maximum near the center of the mesh, however much more concentrated. For mesh imperfection reasons stated before this difference is neglected. The maximum difference in the other regions is around 0.001, and this is

$$\frac{0.001}{1.058-1.035}*100\% = 4.35\%$$

of the maximum increase in total pressure.

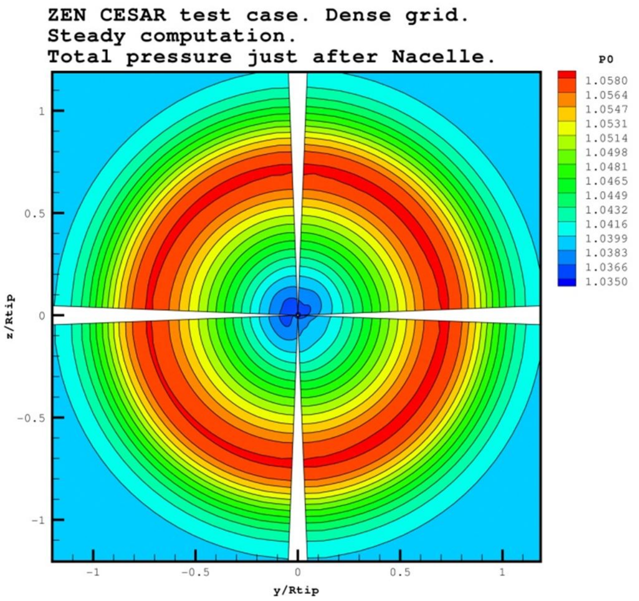

figure 55: P0: steady

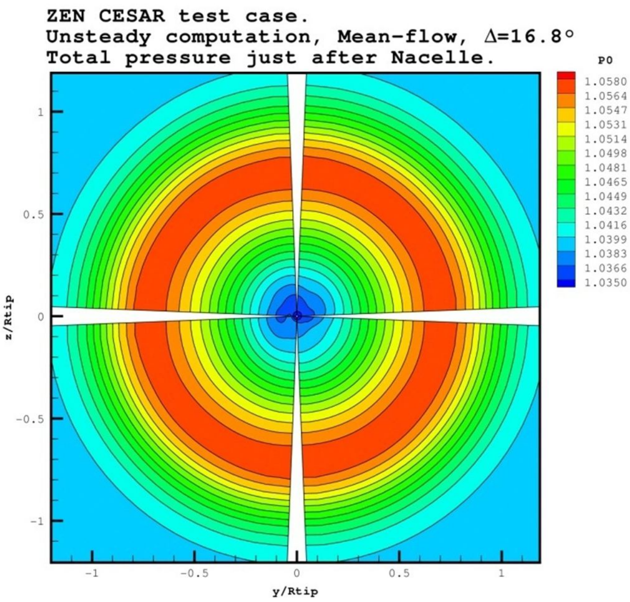

figure 56: P0: unsteady (Δ=16.8)

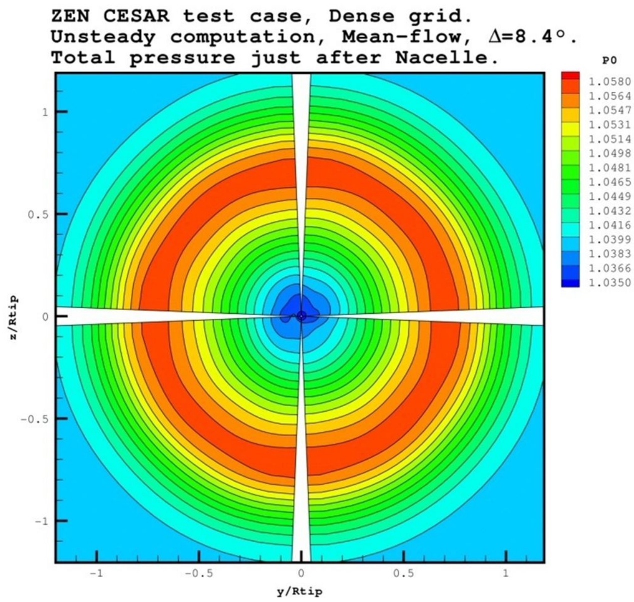

figure 57: P0: unsteady (Δ=8.4)

The difference between the unsteady computation with Δ=16.8° and the computation with Δ=8.4° is depicted in figure 59. The maximum difference is

$$\frac{0.0005}{1.058-1.035}*100\% = 2.2\%$$

of the maximum increase in total pressure, which is of the same relative magnitude as what was found for the coarse grid. The mesh size doesn't seem to have an influence of the phenomenon.

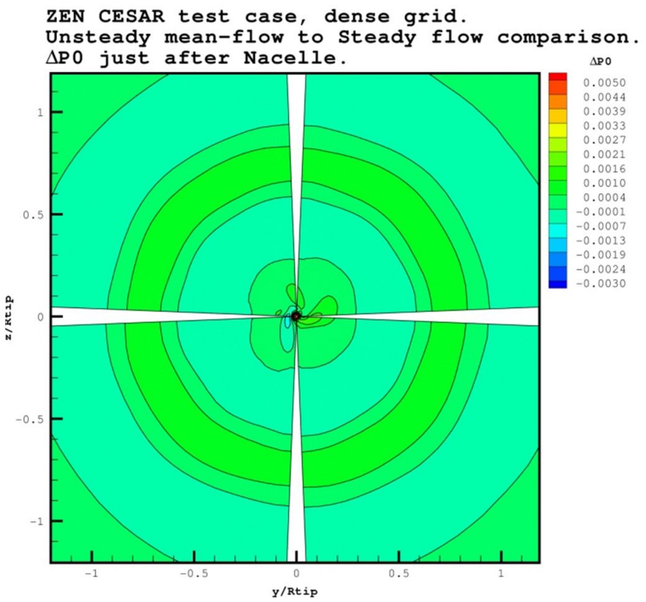

figure 58: ΔP0: steady – unsteady(Δ=16.8)

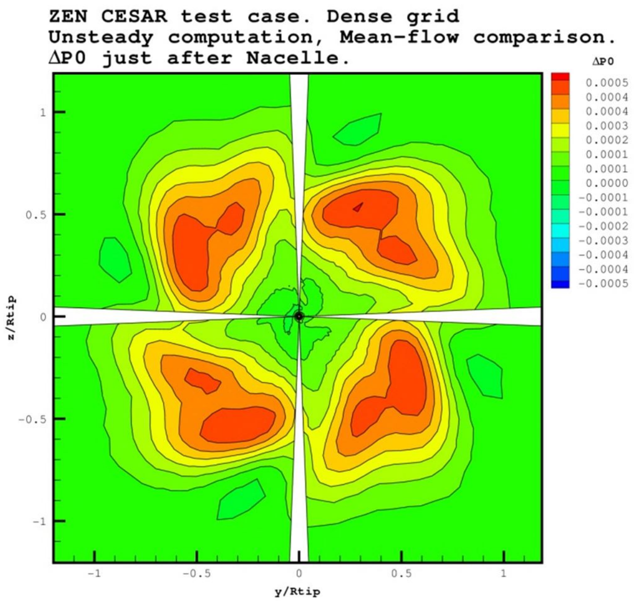

figure 59: ΔP0: unsteady(Δ=16.8)– unsteady(Δ=8.4)

Total temperature

Also on the dense grid it can be concluded from figure 57, figure 61 and figure 62 that there is again little effect from smoothening. The difference between the steady solution and the unsteady solution with Δ=16.8° is depicted in figure 63, and from it can be estimated that the maximum difference between the two is

$$\frac{0.0005}{1.0164-1.0108}*100\% = 8.5\%$$

of the maximum increase of total temperature.

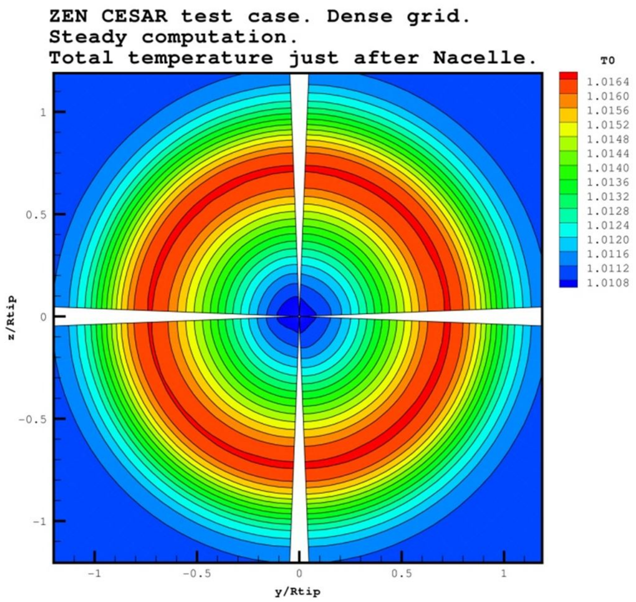

figure 60: T0: steady

The difference between the unsteady computation with Δ=16.8° and the computation with Δ=8.4° is depicted in. The maximum difference is

$$\frac{0.0003}{1.0164-1.0108}*100\% = 5.1\%$$

Of the total increase of total temperature.

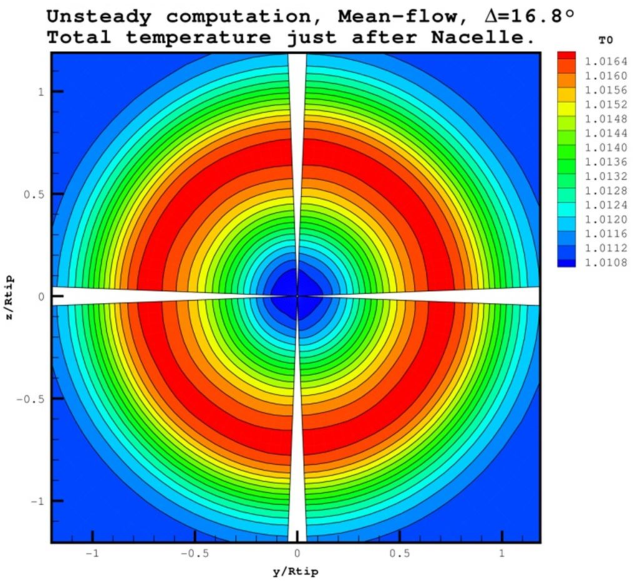

figure 61: T0: unsteady (Δ=16.8)

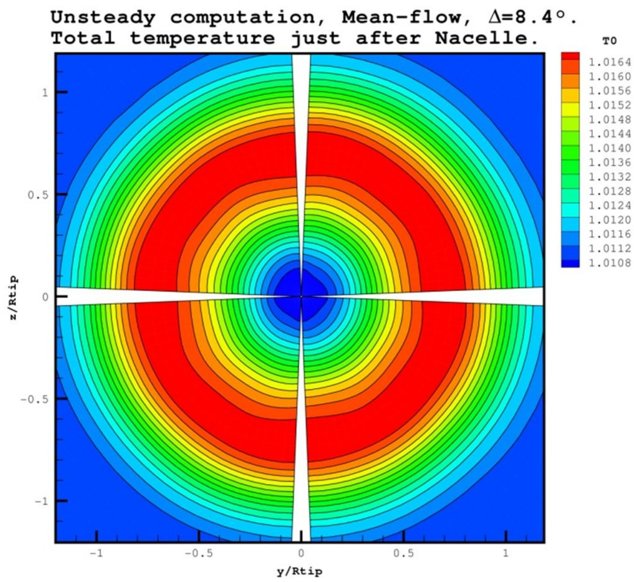

figure 62: T0: unsteady (Δ=8.4)

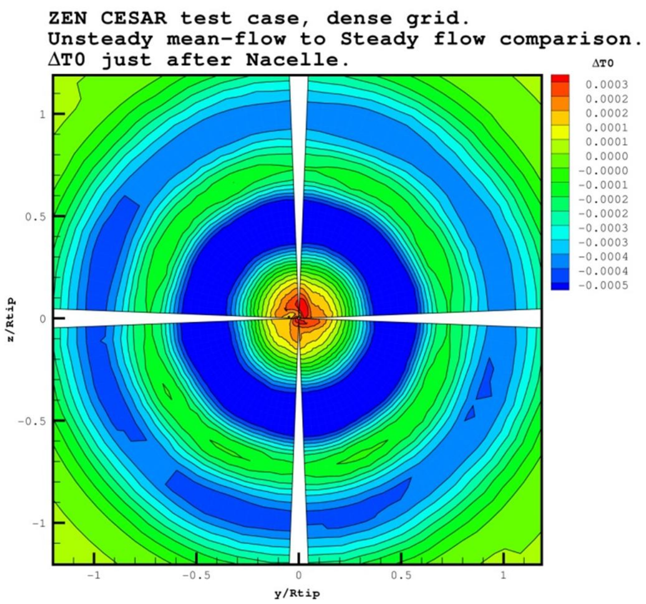

figure 63: ΔT0: steady – unsteady(Δ=16.8)

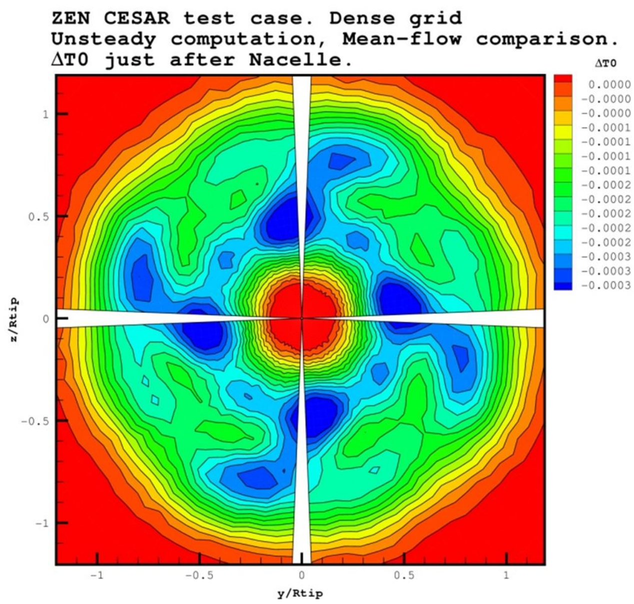

figure 64: ΔT0: unsteady(Δ=16.8)– unsteady(Δ=8.4)

3.3.3. Observations

From the illustrations showcased in the previous paragraph, a number of observations can be made. These are listed below.

- ***Artificial dissipation of total pressure***

Mesh density has an effect on the smoothening caused by the artificial diffusion as was found in the investigation of the steady ZEN results of paragraph 3.2. For reasons explained in paragraph 2.5, a decrease in total pressure is expected for decreasing Δ due to artificial dissipation because kinetic energy is transferred to internal energy in the process.

The result of the unsteady simulation on the coarse grid, displays the opposite. From figure 45, the difference in magnitude of total pressure of the unsteady solution with $\Delta = 16.8°$ is very small in comparison to the distribution of the steady solution. Therefore regrettably, little statements can be made about the artificial dissipation of the high gradients of momentum and energy from the simulation on the coarse grid.

On the dense grid, the presence of artificial dissipation is properly resulting in a decrease in total pressure. However, the results represented in figure 58 and figure 59 show that the difference is very small: The effect of halving the Δ parameter results in a maximum difference of 2% in total pressure.

- ***Total temperature increase and artificial diffusion***

Due to the presence of the effect described in paragraph 2.5, total temperature increases with decreasing Δ. The occurrence of this more or less physical phenomenon is present in the results above. For both the coarse and dense grid, total temperature increases with decreasing Δ. Since the total temperature represents the total enthalpy which is a conserved quantity in ZEN, the differences in the total temperature distribution between the results of the simulations on the dense and coarse mesh respectively, are an illustration of the artificial diffusion as was found in earlier in the steady investigation of paragraph 3.2.

- ***Block structure***

From all plots comparing the effects of the distribution with $\Delta = 16.8°$ and $\Delta = 8.4°$ we observe an effect related to the block structure of the mesh. The occurrence of this effect is due to an interpolation of flow field variables between blocks. Sadly, because this error was found very late in the investigation, no attempts have been made to circumvent the problem which is regrettable because this is likely a source of unwanted noise in the aero-acoustic analysis.

3.4. Conclusions

From the observations made in the previous paragraph, it can be concluded that the use of the unsteady boundary condition as defined in chapter 2.4 generally gives good results. The deviations in the mean flow are consistent with the expected effects of the use of the redistributed boundary conditions as listed in paragraph 2.5. The magnitudes of the effects are small and in no case the total temperature of the solution of the unsteady computation differs more than 10% from the steady result for Δ=16.8%. The decrease of total pressure due to redistribution is never larger than 5%.

The investigation is also inconclusive in some areas. From the tests conducted, only statements can be made about the effects occurring due to an increase in force coefficient concentration. Decreasing Δ increases artificial dissipation and thus increases error. Another test should have been performed with a Δ that is larger than 16.8° to check whether the distribution should incorporate the blade geometry and/or to check if the Δ chosen according to the definition from paragraph 2.4.3 is close to an optimum. This should be further investigated in the future.

4. RAMSYS to ZEN conversion

To generate ZEN actuator disk boundary condition data, a conversion is made from between RAMSYS output and the ZEN BCDAT file.[2] The RAMSYS code (A. D'Alascio) (Rotorcraft Aerodynamic Modelling SYStem) is an unsteady panel code for multi body configurations, based on a boundary integral formulation for arbitrary rigid-body motion in subsonic compressible or incompressible flow. A propeller/rotor geometry is used as input data and the RAMSYS code solves the 3D potential flow around this geometry for certain operational parameters. The code calculates the pressure distribution induced by the flow on the blade. With certain transformations, the code can also output these local pressures as a force coefficient distribution is Cartesian coordinates on the tip path plane. A short description of the tip path plane is given below:

Tip path plane

A possible output of RAMSYS is the forces acting on the blade. While it is possible to extract force data in spanwise, chordwise and normal direction of the real geometry, a more convenient way for conversion to ZEN is the output data in the tip path plane frame of reference. The tip path plane is the plane in which the tips of the rotor turn and thus it is a plane perpendicular to the axis of rotation. This is different from a local frame of reference of a blade section because RAMSYS includes a routine that calculates the deflection of the blade due to elastic effects, which results in a possible rotor shape depicted in the upper part of figure 65. The tip path plane frame of reference makes sure all the force coefficients are defined in the same global directions which simplifies the conversion to ZEN.

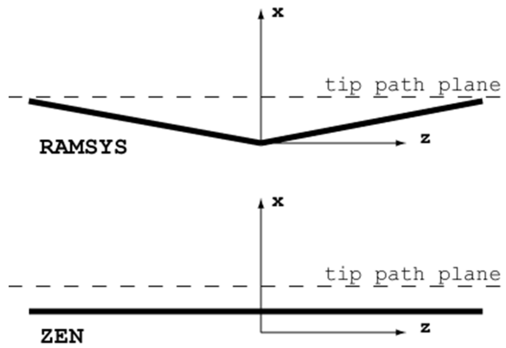

figure 65: tip path plane definition

When this tip path plane force coefficient data is given for the full rotation of a rotor, the result is a disk of force coefficients. A simple transformation leads to force coefficients in the tip path plane, defined in polar coordinates. These non-dimensional force coefficients are:

$C_N M_l^2(r,\psi)$: Force coefficient in axial direction

$C_A M_l^2(r,\psi)$: Force coefficient in tangential direction

$C_Y M_l^2(r,\psi)$: Force coeffcient in radial direction

Where M_l is the local Mach number defined as V_l / a_∞ with $V_l = \Omega r + V_\infty \sin\psi$. How this data is constructed from the Cartesian RAMSYS output is explained in appendix IV.II. Keeping in mind the axis definitions in appendix 0, it is possible to convert this data into a ZEN actuator disk boundary condition distribution using the non-dimensionalization explained in appendix I and III.

[2] Note that this is a choice. Other CFD codes can be used to create the AD boundary data as well.

The resulting output of the conversion consists of a disk distribution for a number of positions in r and ψ of the following non-dimensional force coefficients:

$$\frac{dC_T}{d\bar{r}}(r,\psi): \text{ thrust coefficient per unit non-dimensional radius}$$

$$\frac{dC_P}{d\bar{r}}(r,\psi): \text{ power coefficient per unit non-dimensional radius}$$

$$\frac{dC_r}{d\bar{r}}(r,\psi): \text{ radial force coefficient per unit non-dimensional radius}$$

These coefficients on the disk are the input data for a steady ZEN run. In the following paragraph, this conversion is tested after which it is used to investigate a number of propeller/rotor geometries.

4.1. Conversion test

To test if the conversion from RAMSYS to ZEN is correct, a comparison is made of the force distribution on a blade. The boundary condition data that is compared is constructed with the method described in the previous paragraph. Furthermore. the geometry used is the APIAN blade, shown in the next paragraph. The comparison consists of:

- The force distribution per unit radius derived present in the BCDAT after the conversion has been made using definitions listed in Appendices I, III and 0.
- The force distribution calculated by the integration over all the panels of the forces acting on them in RAMSYS.

Results are shown below:

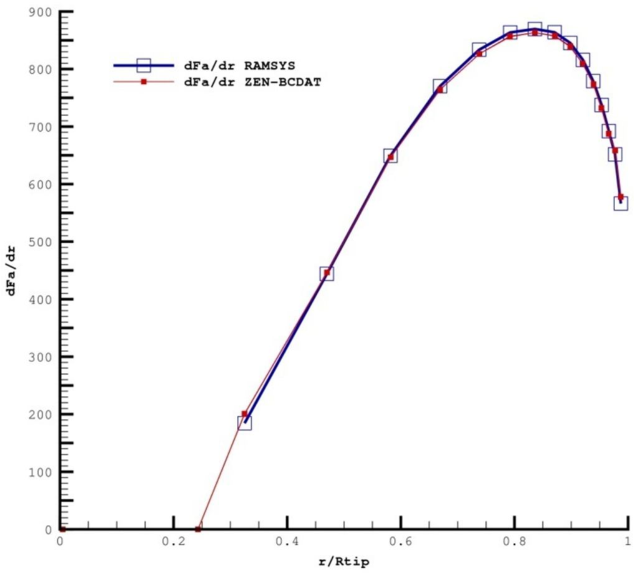

figure 66: axial force per unit radius comparison

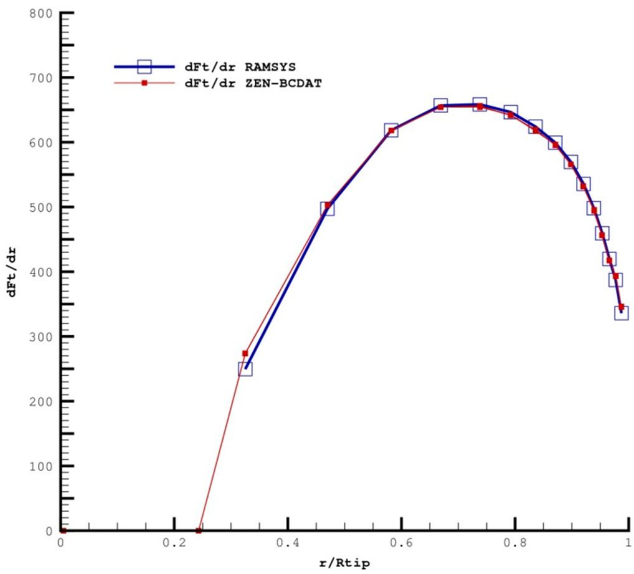

figure 67: tangential force per unit radius comparison

figure 66 shows the axial force distribution, figure 67 shows the tangential force distribution while figure 68 shows the radial force distribution, all per unit radius. From the graphs, it can be concluded that the conversion from RAMSYS output data to ZEN AD force model BCDAT input data is correct.

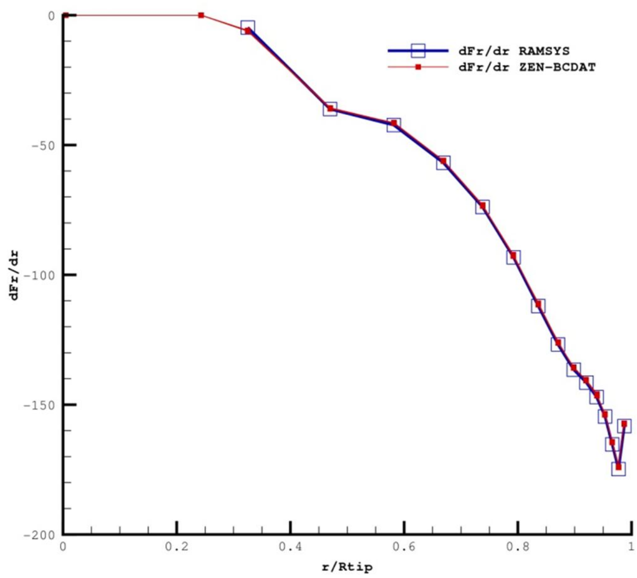

figure 68: radial force per unit radius comparison

4.2. Test case results

To test the effects of using RAMSYS data as input data for ZEN a number of test cases are investigated, each with a different blade geometry. Results are shown below.

4.2.1. APIAN propeller

This paragraph describes the simulation of the propeller used in the APIAN (Advanced Propulsion Integration Aerodynamics and Noise)-project. The advantage of using this rotor is in the fact that it is well studied and as a consequence there is experimental data available. Its geometry however is quite complicated. A picture of the rotor is displayed in figure 69.

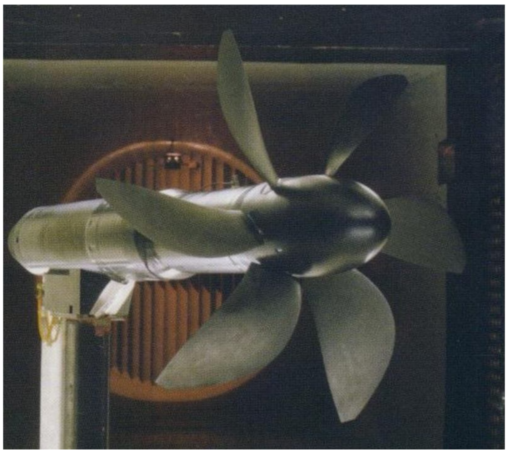

figure 69; APIAN 6-blade propeller

A simulation of RAMSYS has been performed with the APIAN propeller and dummy nacelle geometry. Relevant test data is displayed below:

APIAN geometrical properties

Tip radius:	0.25 m
Hub ratio:	0.243
Number of blades:	6

APIAN test conditions

Free stream Mach number:	0.23
Rotational speed:	876 rpm
Advance ratio:	1.118
Free stream pressure:	101673 Pa
Free stream density:	1.225 kg/m^3
Angle of incidence α:	0°

The run in ZEN is done on a redimensionalized version of the grid shown in paragraph 3.1.3. The convergence history is plotted below:

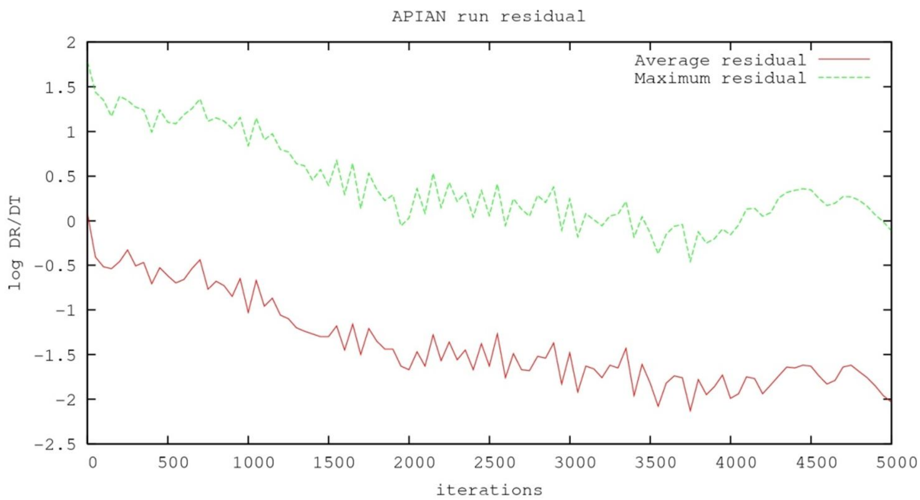

figure 70: Steady APIAN ZEN convergence plot

Conversion results:

For validation of the conversion, the velocity profile evolution in downstream direction is examined. At different axial positions, from both the steady ZEN and time averaged RAMSYS simulation velocity profiles are extracted. ZEN simulations are done using the dense grid for accurate results. The plane is chosen such that the x-velocity represents the axial velocity, the y-velocity represents the tangential velocity and the z-velocity represents the radial velocity. Results are shown below:

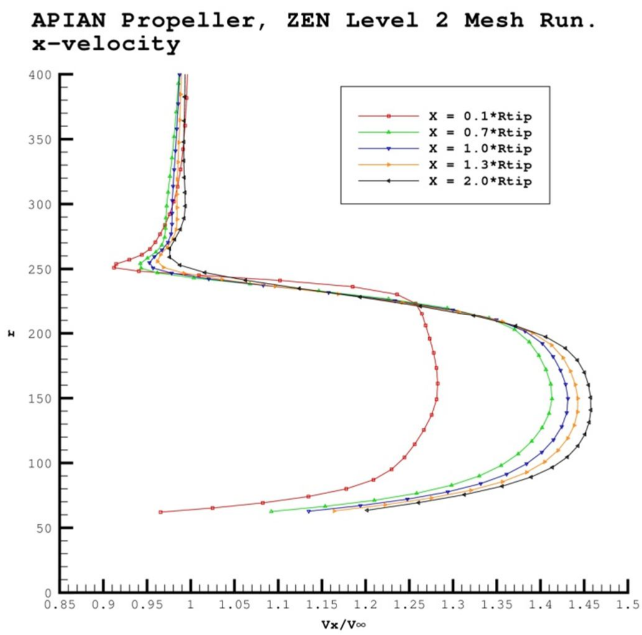

figure 71: APIAN propeller: ZEN axial velocity profiles

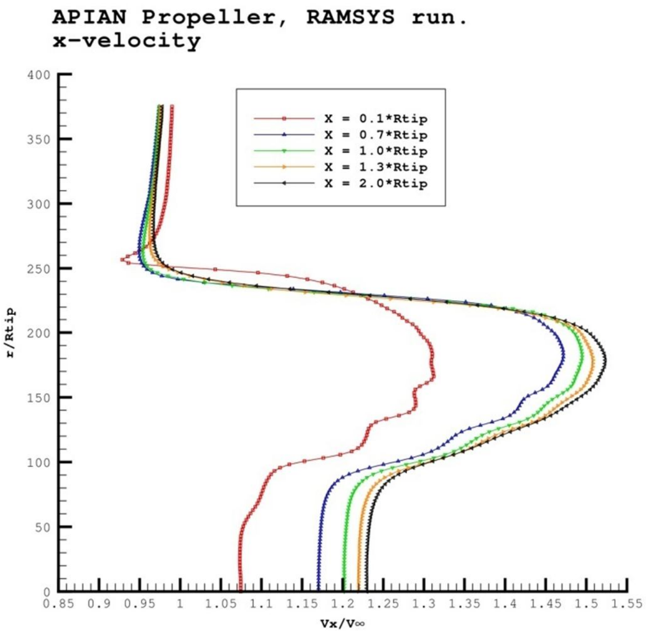

figure 72: APIAN propeller: RAMSYS axial velocity profiles

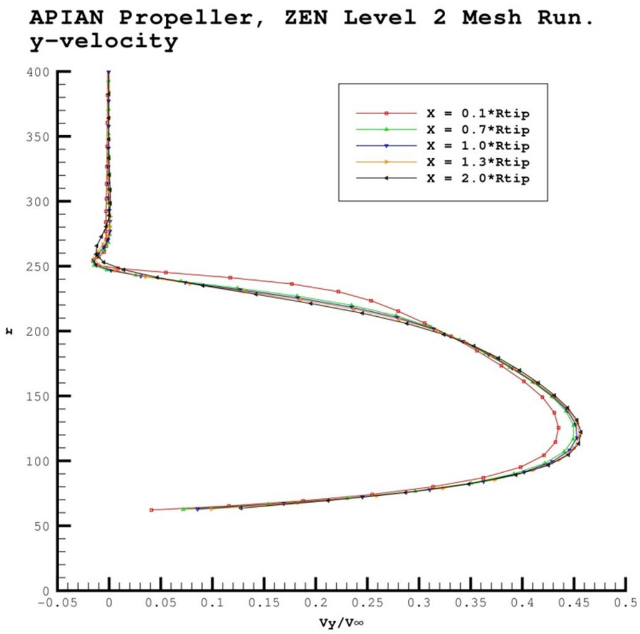

figure 73: APIAN propeller: ZEN tangential velocity profiles

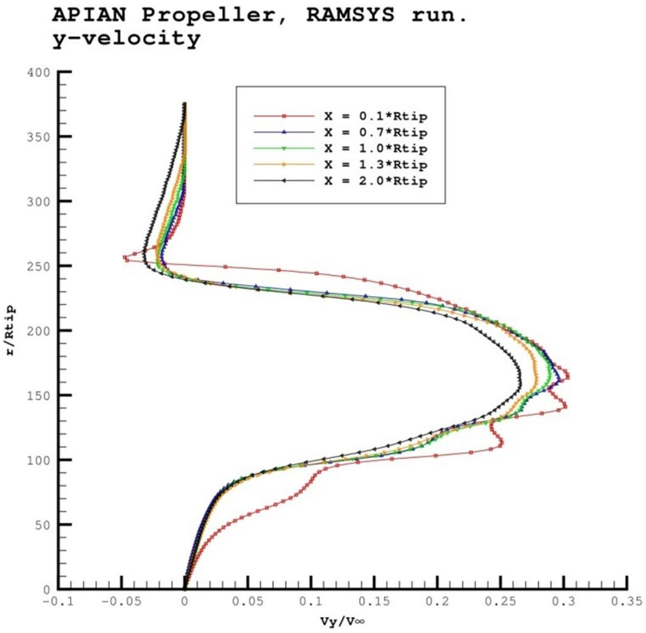

figure 74: APIAN propeller: RAMSYS tangential velocity profiles

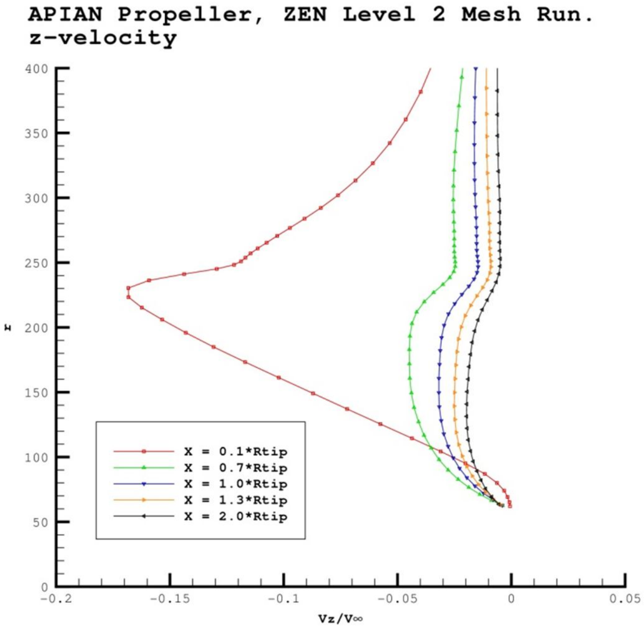

figure 75: APIAN propeller: ZEN radial velocity profiles

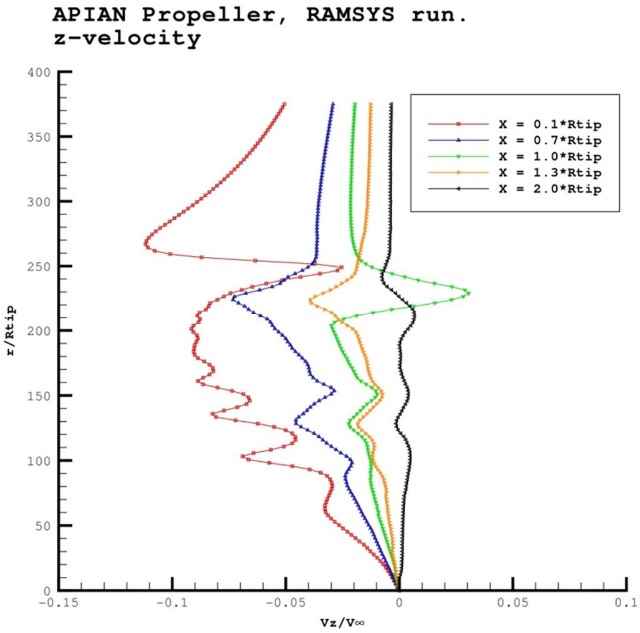

figure 76: APIAN propeller: RAMSYS radial velocity profiles

The results shown above indicate an error. Since the time averaged RAMSYS results shown agree to some degree with the existing ZEN AD field model results, displayed below.

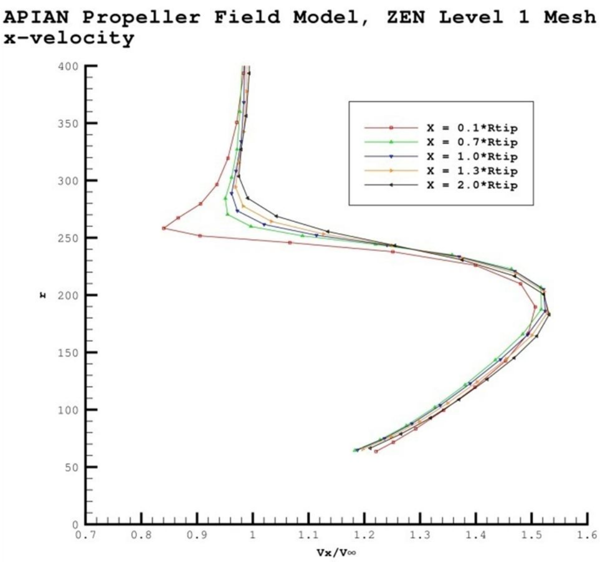

figure 77: APIAN propeller; ZEN field model run: axial velocity profiles

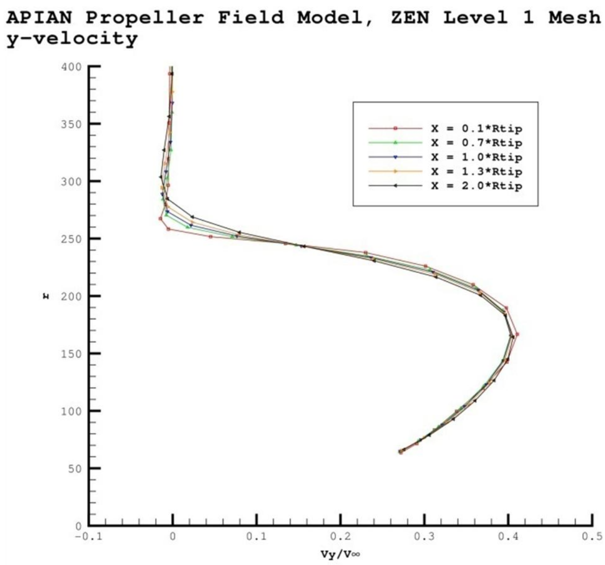

figure 78: APIAN propeller; ZEN field model run: tangential velocity profiles

Even though the field model simulation was done using the coarse grid, these results were validated in an earlier investigation of the APIAN propeller. From figure 76 we see that the maximum in axial velocity is close to the tip, which is also the case with the time-averaged RAMSYS result displayed in figure 72.

From paragraph 4.1 it was learned that the non-dimensionalizing of the force coefficient data was done in the correct way. Therefore, in theory the BCDAT file should include the proper force coefficient distribution and this means something awkward is happening if the RAMSYS data is used as ZEN input for the APIAN test case. A test with an even denser grid (2x2x2 times as dense as before) is done to rule out the effect of mesh density. The results are shown below:

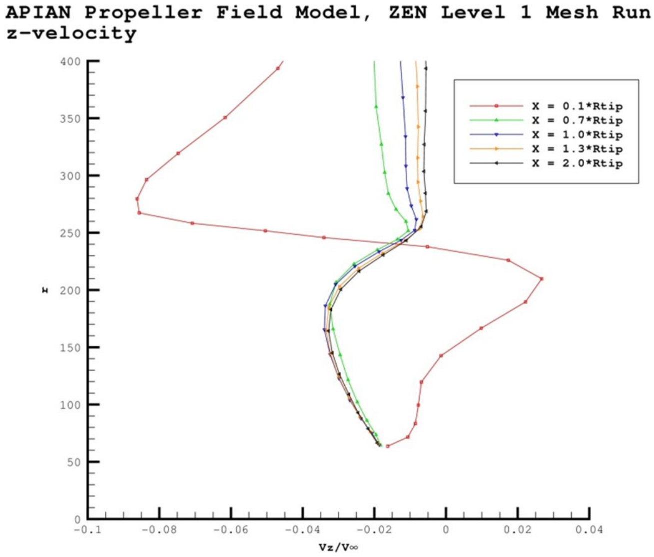

figure 79: APIAN propeller; ZEN field model run: radial velocity profiles

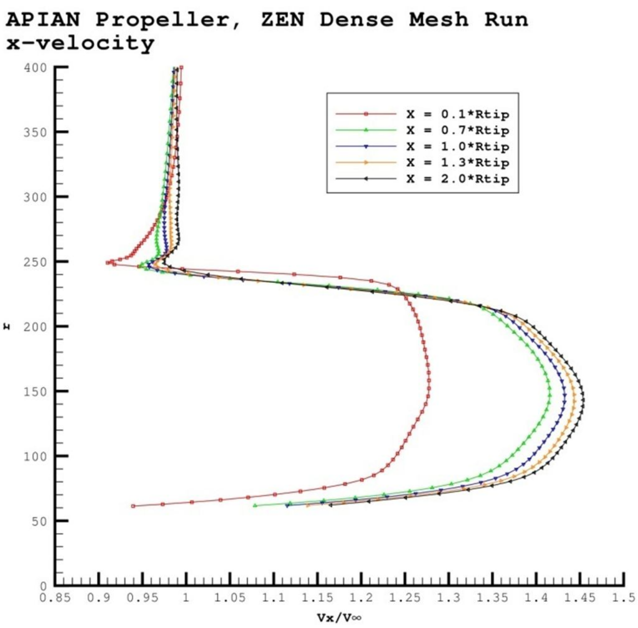

figure 80: APIAN propeller; ZEN run on denser mesh: axial velocity profiles

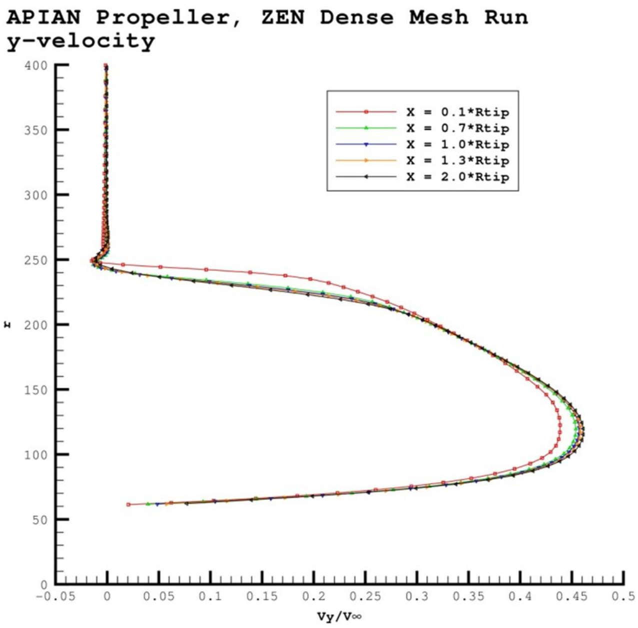

figure 81: APIAN propeller; ZEN run on denser mesh: tangential velocity profiles

Because there are no further numerical phenomena in ZEN that can cause an error of this magnitude to exist, the question arises if the non-correspondence of the simulation results with RAMSYS is the result of a physical effect. This however, is hard to prove. An analysis has to be performed in the future to investigate why the force coefficient data is not sufficient to simulate the flow field it induces.

As a result, the APIAN propeller is abandoned for another test case in order to find out whether or not the ZEN BCDAT can be constructed from RAMSYS data properly and the problem is indeed specific to the APIAN propeller test case.

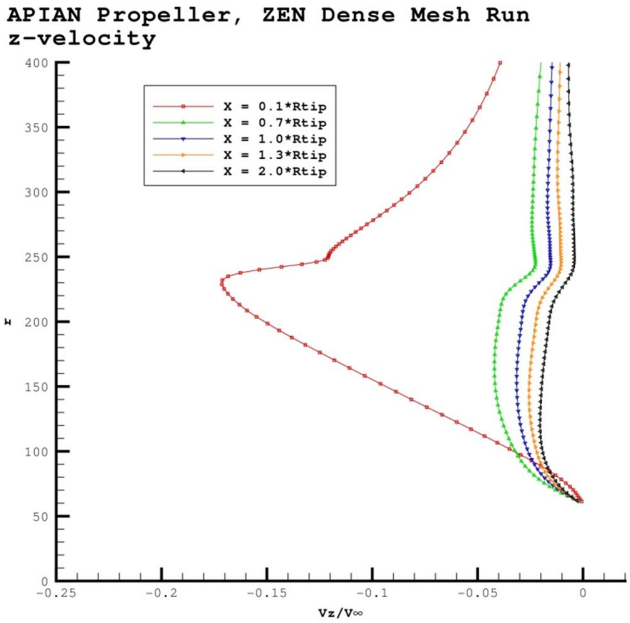

figure 82: APIAN propeller; ZEN run on denser mesh: radial velocity profiles

4.2.2. Fictional helicopter rotor test case

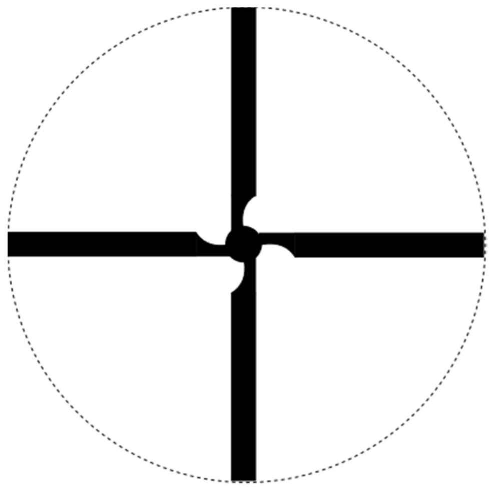

This paragraph describes the simulations done on a fictional helicopter rotor under hover conditions. The choice for this test case was made because of its simple geometry; the blades have a constant chord. Also, in a previous project, the helicopter rotor was successfully converted from RAMSYS to ZEN.

A simulation of RAMSYS has been performed on the fictional helicopter rotor geometry. Relevant test data is displayed below:

Fictional helicopter rotor geometrical properties

Tip radius:	8.54 m
Hub ratio:	0.200
Number of blades:	4

Fictional helicopter rotor test conditions

Free stream Mach number:	0.003 (Hover condition)
Rotational speed:	222 rpm
Advance ratio:	0.0322
Free stream pressure:	91076 Pa
Free stream density:	1.103 kg/m^3
Angle of incidence α:	0°

The steady run in ZEN is done on the grid depicted in the next paragraph. The convergence history is plotted below:

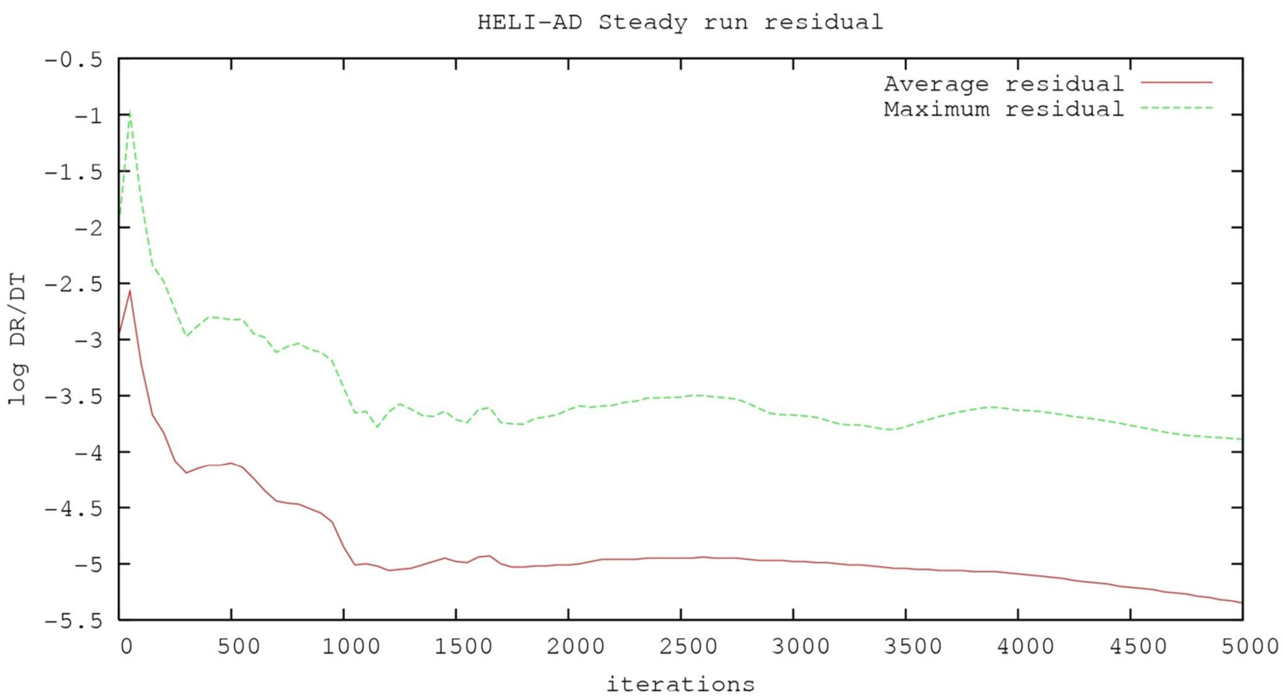

figure 83: Steady HELI_AD ZEN convergence plot

Grid

The grid used for the fictional helicopter is depicted below:

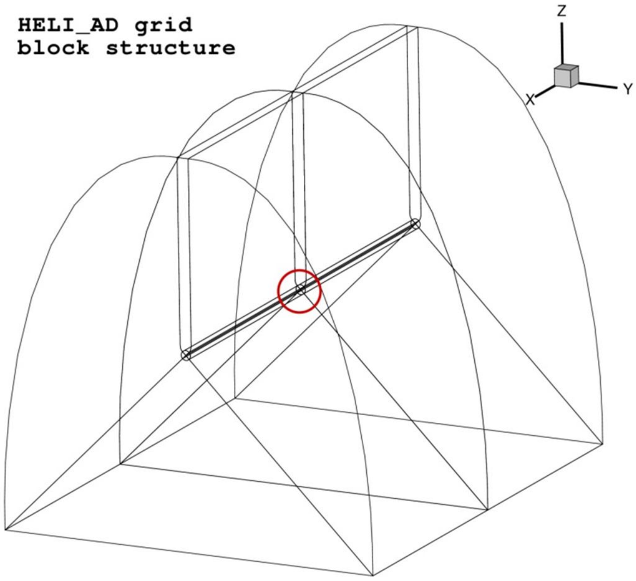

figure 84: HELI_AD grid block structure

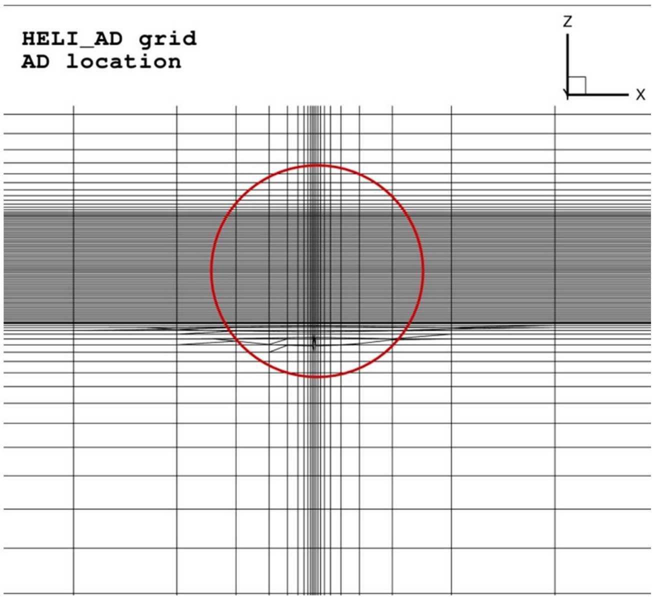

figure 85: HELI_AD grid(ZX plane) showing AD location

The mesh structure differs quite a bit from forward flight meshes suited for propellers. The mesh used here was generated for the simulation of forward flight for a helicopter (Tomas, 2009), which involves a very high angle of incidence of the free stream. Nevertheless, it can also be used for this specific test case.

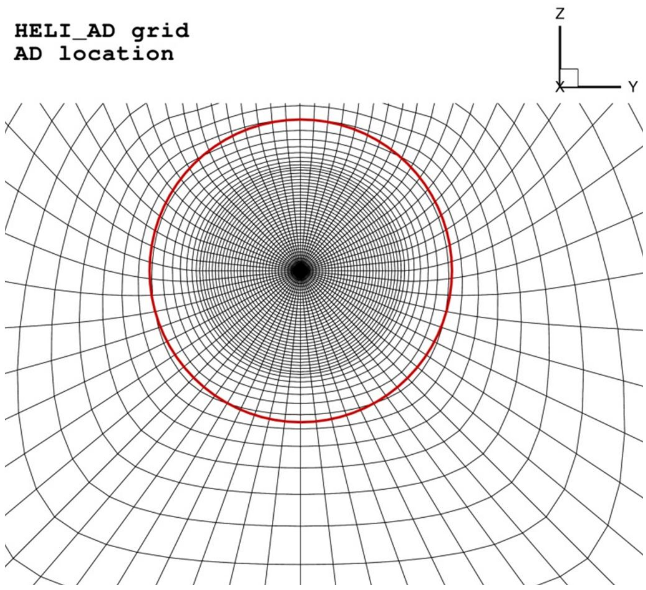

figure 86: HELI_AD grid(ZY plane) showing AD location

Conversion results:

For validation of the conversion, again the velocity profile evolution in downstream direction is examined. At different axial positions, from both the steady ZEN and time averaged RAMSYS simulation velocity profiles are extracted. In contrast to the APIAN investigation, the results are plotted in one figure for each velocity direction:

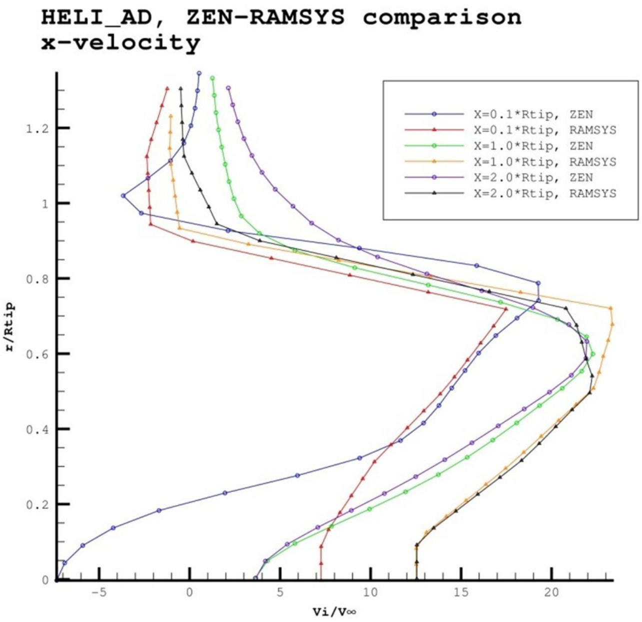

figure 87: HELI_AD axial velocity profiles

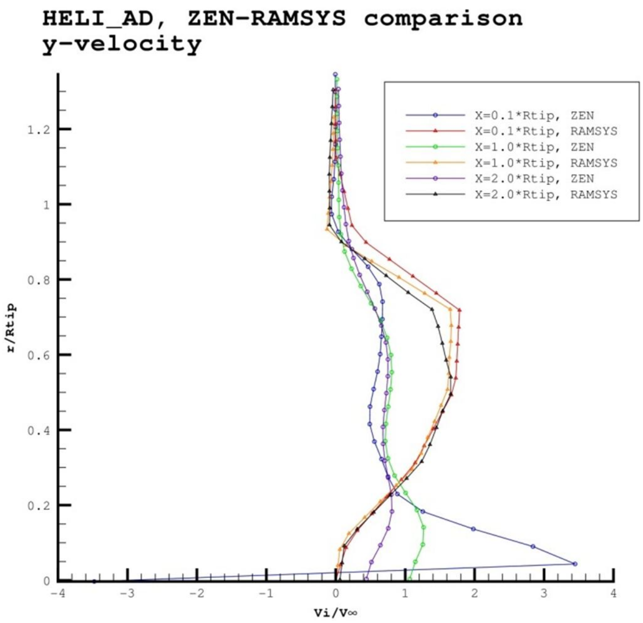

figure 88: HELI_AD tangential velocity profiles

In the velocity profiles displayed, it can be seen that results more or less agree between RAMSYS and ZEN. The differences close to the hub are a result of the difference in approach: In ZEN a certain hub condition is defined, while in RAMSYS, a geometry is present there. The axial velocity profiles of figure 87 show the maximum to be more or less in the right position for all 3 positions. The tangential velocity profile differs a bit, but the induced velocities in this direction are very small in comparison to the axial velocities and so this might be a numerical problem as much as anything else. The radial velocity profiles in figure 88 compare very good.

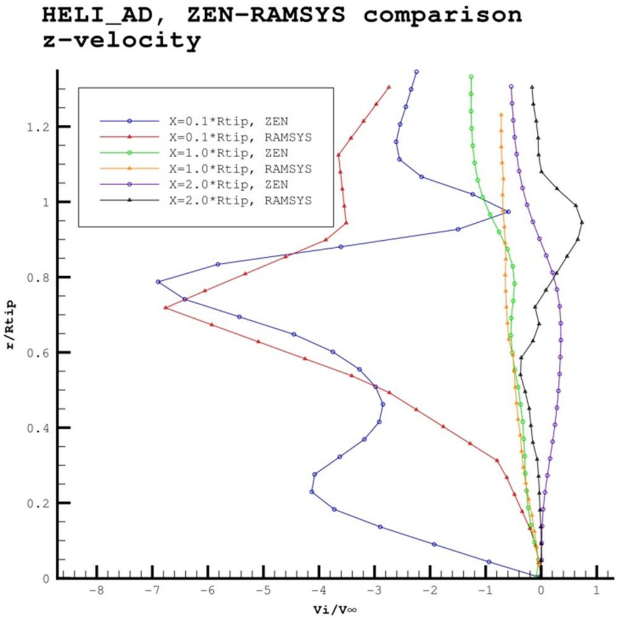

figure 89: HELI_AD radial velocity profiles

Therefore, it can be concluded that for this test case acceptable results are obtained. This was expected since the test case was carried out before in the past. However, for future purposes the results cannot be used since the ZEN solver has severe stability problems with a very low Mach number of the free stream. Therefore, another test case is considered to provide usable data for the aeroacoustic analysis of chapter 5.

4.2.3. Prop-rotor test case

This paragraph describes the simulations done on a classified prop-rotor geometry in forward flight. The choice for this test case was made because of the fact that the blades are more similar to a helicopter rotor than more common lower aspect ratio propeller blades and therefore good results are expected. On the other hand, more complex features like a variable chord are present in the geometry that make the investigation more interesting.

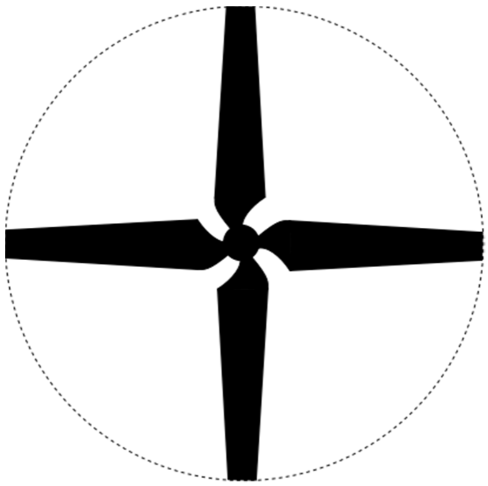

A simulation of RAMSYS has been performed on the fictional helicopter rotor geometry. Relevant test data is displayed below:

Prop- rotor geometrical properties

Tip radius:	3.70 m
Hub ratio:	0.108
Number of blades:	4

Prop-rotor test conditions

Free stream Mach number:	0.303
Rotational speed:	426 rpm
Advance ratio:	1.958

Free stream pressure:	97753 Pa
Free stream density:	1.19 kg/m³
Angle of incidence α:	0°

The steady run in ZEN is done on the grid displayed in the next paragraph. The convergence history is plotted below:

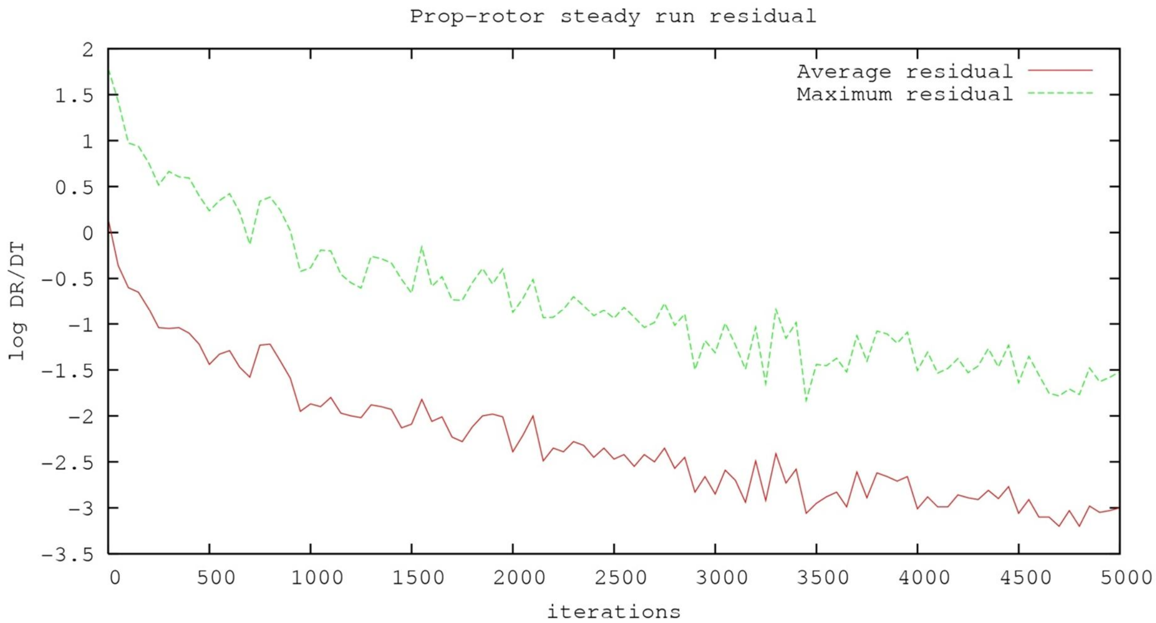

figure 90: Steady Prop-rotor ZEN convergence plot

Mesh

The grid used for the fictional helicopter is a modified version of the grid presented in paragraph 3.1.3, to include the hub ratio specification of the prop-rotor. Also it has twice as many cells in radial direction for improved accuracy. Details are shown below. Note that this is the coarse grid; the dense grid has twice as many cells in every dimension.

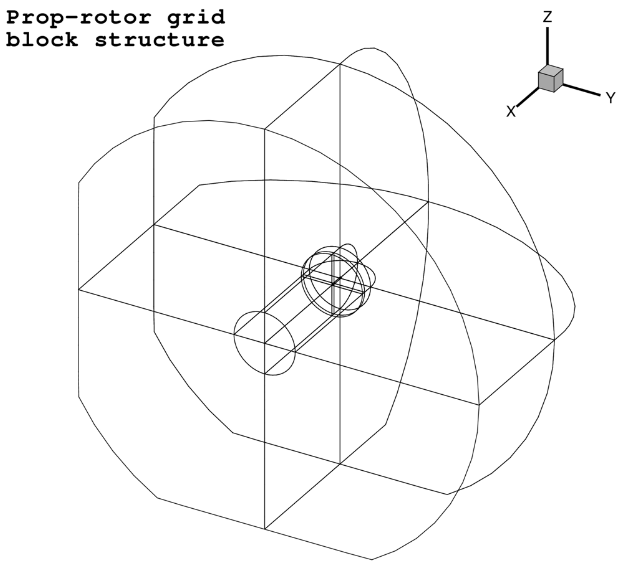

figure 91: Prop-rotor grid block structure

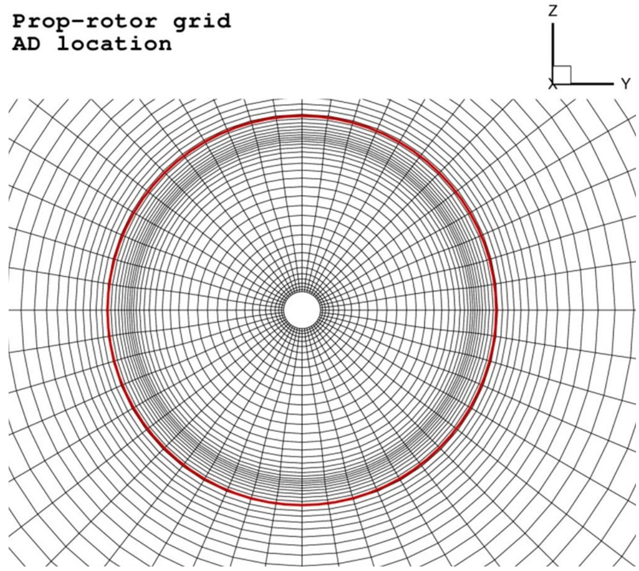

figure 92: Prop rotor grid(ZX-plane) showing AD location

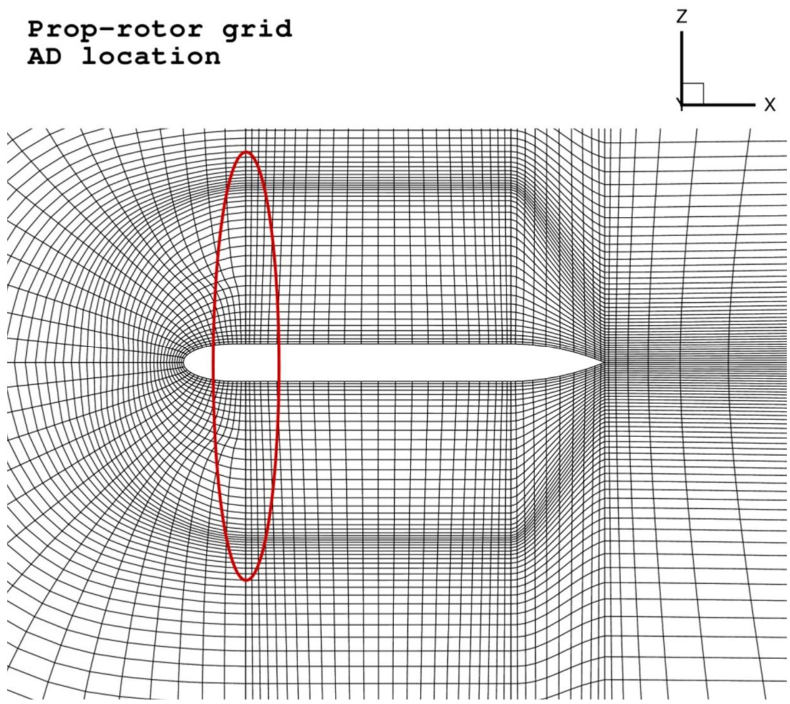

figure 93: Prop rotor grid(ZY-plane) showing AD location

Conversion results:
For validation of the conversion, again the velocity profile evolution in downstream direction is examined. At different axial positions, from both the steady ZEN and time averaged RAMSYS simulation velocity profiles are extracted:

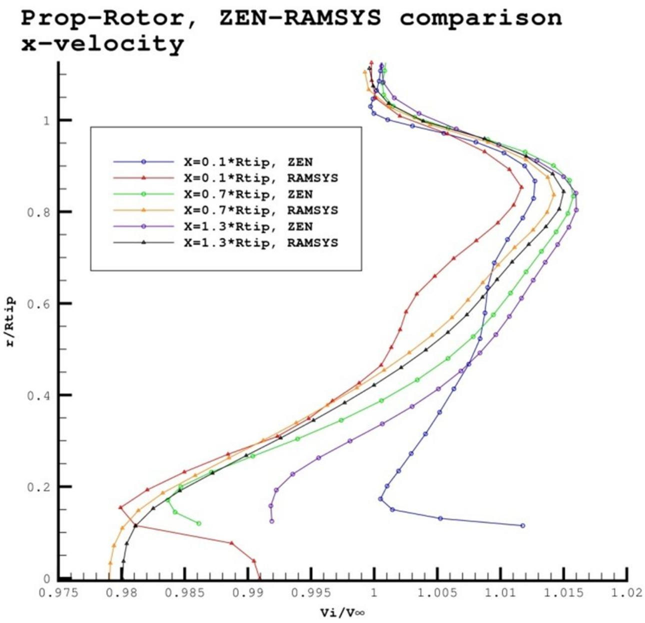

figure 94: Prop-rotor axial velocity profiles

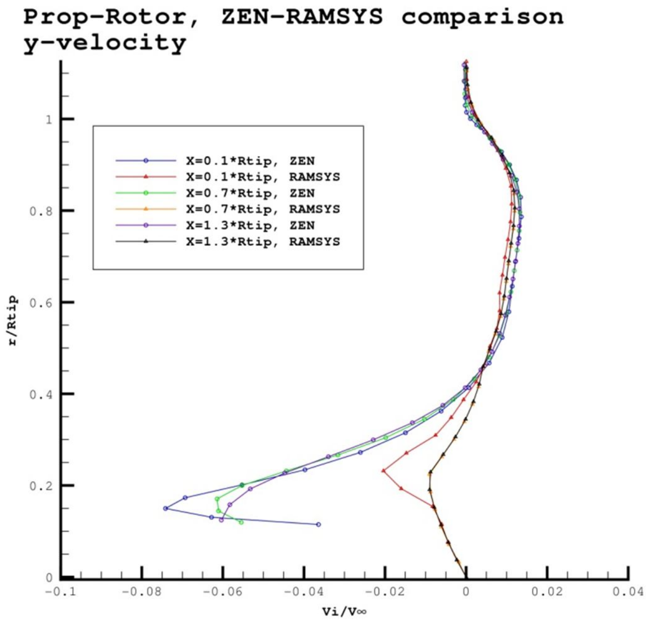

figure 95: Prop-rotor tangential velocity profiles

The results are similar to the results of the fictional helicopter. Close to the nacelle, there is some difference between RAMSYS and ZEN. These differences indicate the effects of the presence of the nacelle in the ZEN simulation, which is not present in the RAMSYS simulation. However, again it can be observed from the axial velocity profiles of figure 94 that the ZEN profiles have the right shape and the maximum is at the same radial position as the profiles obtained with RAMSYS. The same is true for the tangential and radial velocities depicted in figure 95 and figure 96 respectively. Therefore, it can be assumed safely that the simulations for the prop-rotor boundary condition data in ZEN give a coherent representation of the flow with respect to the RAMSYS solution of the flow field.

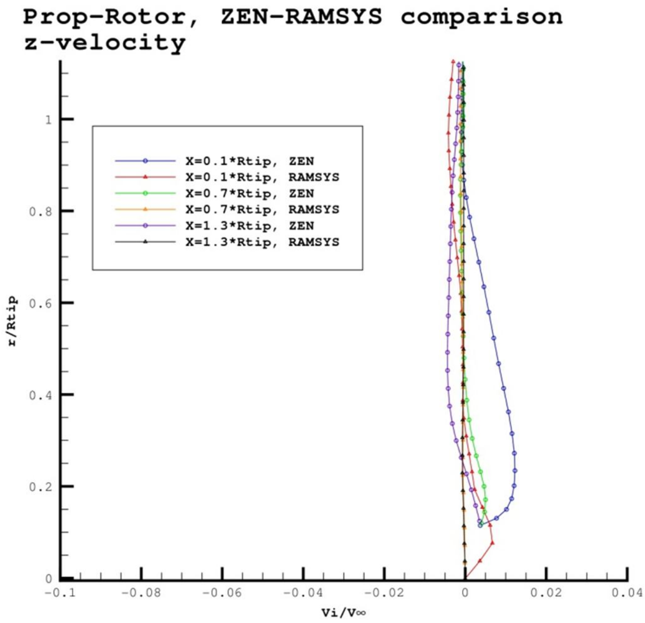

figure 96: Prop-rotor radial velocity profiles

4.3. Conclusions

From the investigation in this chapter, a number of things can be concluded:

- The conversion interface between ZEN and RAMSYS works as expected. This means that the non-dimensionalization explained in appendix I,III and 0 is correct, together with axis orientations.

- The use of an actuator disk to model a propeller/rotor using solely force coefficient data does not always work with satisfactory results. Why this is the case is not known. Possible causes for error are discrepancies, e.g. the absence of certain flow features in ZEN, or faulty RAMSYS-simulation output. This needs to be further investigated in the future.

  Therefore, the use of the converted RAMSYS data should always be checked and validated.

- The HELI-AD investigation shows satisfactory compliance with RAMSYS simulation results. The same is the case for the Prop-rotor geometry. It should be noted that close to the nacelle/hub, values are slightly off. This is due to a difference in method between RAMSYS and ZEN near the nacelle/hub. To properly check the results and for the sake of scientific rigor, RAMSYS simulations should be conducted with proper nacelle/hub geometry. Because of the limited time available for the investigation, this is recommended to do in future investigations.

- The Prop-rotor geometry is found suited for future investigation, because the test involves forward flight. All the aero-acoustic tests will be done on this geometry.

Summary of results so far

Before the investigation into aero-acoustics begins in the next chapter, a short recap of conclusions regarding (U)ZEN is displayed below:

On steady ZEN:

- In steady ZEN, the simulation works as expected. The influence of the grid density is visible in the results and complies with the spatial scheme accuracy.

On unsteady ZEN:

- As was predicted, the use of unsteady ZEN introduces two effects in comparison with steady ZEN:

    1. the increase of total enthalpy in the flow.
    2. the decrease of total pressure due to artificial dissipation.

    The second effect is found to be very small, even neglible. The first effect is larger, but since this is a physical phenomenon this is not considered an error.

- With the Δ specified, the mean flow of the unsteady simulations shows overall good compliance with the steady flow solution and the method is validated.

- With the tests conducted, any statements about the influence of the shape of the unsteady distribution are inconclusive. What can be concluded is that a too concentrated distribution will result in higher gradients and more artificial dissipation thus lesser accuracy. No statements can be made about the assumption that the distribution should incorporate physical properties of the blades. To find an optimum in the magnitude of Δ, comparison should be made between unsteady ZEN results and experimental data. The present distribution definitions give satisfactory results.

- The generation of difference plots shows a small defect due to interpolation between mesh blocks. This effect should be kept in mind in the aero-acoustic investigation.

On the RAMSYS to ZEN conversion:

- The conversion is validated for two geometries. The cause of the erroneous flow field results of the APIAN geometry is unknown. Therefore when using the method, a flow field comparison between ZEN, RAMSYS and preferably experimental data should always be made to check for coherence.

5. Aeroacoustics

With the results from UZEN of the prop-rotor test case, it is possible to make an aero-acoustic analysis of the noise generated by the test case. This will be done in this chapter. In the first paragraph, a small introduction on the theory used is included. In paragraph two the test setup will be described, together with a description of the input files and parameters used. Furthermore, the third paragraph contains the results of the aero-acoustic simulation of the UZEN results. This paragraph will be divided into a number of subparagraphs, each one containing a specific comparison. Finally, the fourth paragraph contains the observations and conclusions that can be made from the investigation.

5.1. Ffowcs Williams-Hawkings analogy

For aero-acoustic predictions, there are two strategies that can be adopted. One is based on the Computational AeroAcoustic approach, the other is based on the integral formulations. The CAA approach predicts the acoustic fluctuations using classical CFD methods with high accuracy numerical schemes. For this method to be cost effective, the approach is limited to near-field predictions. On the other hand, with integral formulations it is possible to propagate near field fluctuations to the far field at computational cost which doesn't depend on observation distance.

Combining these strategies leads to a hybrid approach using acoustic analogies. The acoustic analogy-approach is based on the ideal assumption that the sources of sound generation can be separated from its propagation in the physical domain. Therefore, the governing equations are rearranged in a form of the wave equation, where all the terms not included in wave propagation are gathered in the right hand side of the equation as source terms. The first model of this approach was proposed by Lighthill. (Lighthill, 1952). Later on, this model was extended by Ffowcs Willams and Hawkings (Ffowcs Williams J. E., 1969). The Ffowcs Williams-Hawkings(FW-H) approach is the most appropriate analogy for understanding the mechanisms involved in the generation of aerodynamic sound from bodies in complex motion, which is the case in predictions of rotor noise. A short description of the analogy is given below. For a more detailed derivation of the analogy, the reader can resort to appendix V.

5.1.1. Theory

Consider a control surface $f(\vec{x},t)=0$ with a boundary that moves with velocity $\vec{v}(\vec{x},t)$. Furthermore, the surface is defined such that $\nabla f = \vec{n}$, where $\vec{n}$ is the unit normal vector that points out of the surface. The flow field enclosed by this surface ($f<0$) can be replaced by a quiescent fluid combined with a surface distribution of sources that the restore the conservative character of the field. This allows us, after some manipulations described in appendix V, to write the linear conservation equation of mass and momentum as:

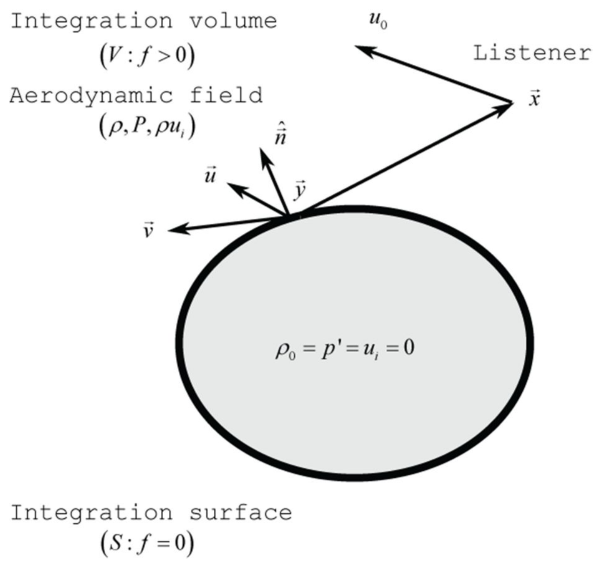

$$
\begin{aligned}
&\frac{\partial \rho}{\partial t}+\frac{\partial}{\partial x_i}\left(\rho u_i\right)=\rho_0 u_n \delta(f)+\left(\rho-\rho_0\right)\left(u_n-v_n\right)\delta(f) \\
&\frac{\partial}{\partial t}\left(\rho u_i\right)+\frac{\partial}{\partial x_j}\left(P_{ij}+\rho u_i u_j\right)=P_{ij}' n_j \delta(f)+\rho u_i\left(u_n-v_n\right)\delta(f)
\end{aligned}
\tag{4.1}
$$

where $P_{ij}=\left(p-p_0\right)\delta_{ij}-\tau_{ij}$ is the compressive stress tensor and $P_{ij}'=P_{ij}-p_0\delta_{ij}$ is the perturbation stress tensor. Furthermore, subscript n denotes the velocities normal to the integration surface S and $\delta(f)$ denotes the Dirac delta function. Rearranging these equations leads to the Ffowcs Williams-Hawkings equation for a permeable surface:

$$
\Box^2\left[c^2\left(\rho-\rho_0\right)\right]=\frac{\partial}{\partial t}\left[Q\delta(f)\right]-\frac{\partial}{\partial x_i}\left[L_i\delta(f)\right]+\frac{\partial^2 T_{ij}}{\partial x_i \partial x_j}
\tag{4.2}
$$

where:

$$
Q=\rho_0 U_i n_i, \quad U_i=u_i+\left(\frac{\rho}{\rho_0}-1\right)\left(u_i-v_i\right), \quad L_i=P_{ij}' n_j+\rho u_i\left(u_n-v_n\right)
\tag{4.3}
$$

And where

$$
T_{ij}=P_{ij}'+\rho u_i u_j-c^2\left(\rho-\rho_0\right)\delta_{ij}
\tag{4.4}
$$

is Lighthill's equivalent stress tensor. Assuming sufficiently small perturbations in the medium, the solution of the pressure perturbations of this equation is again derived in appendix V.I, and can be written in a compact way as:

$$
p'(\vec{x},t)=p_Q'(\vec{x},t)+p_L'(\vec{x},t)+p_T'(\vec{x},t)
$$

which describes that the pressure perturbations are divided into 3 components, namely the thickness noise p_Q', the loading noise p_L' and the quadrupole noise term p_T'. The loading term accounts for the unsteady loading exerted by the body on the fluid, while the thickness term accounts for the displacement of fluid produced by the moving body. Furthermore, the quadruple noise term accounts for all the flow non-linearity in the exterior of the control surface where $f>0$.

5.2. Test setup

The simulation software used was written by Damiano Casalino and it can be configured in multiple ways. This enables us to make a comparison between the aero-acoustic predictions using UZEN aerodynamical results as input and the aero-acoustic predictions of an actual rotating geometry in a flow. The input of this rotating geometry can be specified using RAMSYS output data, which consists of the surface of a propeller with local pressure values for a specific number of time steps, generating thickness and loading noise. Since RAMSYS was also used to construct the boundary conditions for UZEN, this enables us to investigate the influence of the CFD approach on the final aero-acoustic result.

The UZEN simulation output is used as the boundary condition data for the aero-acoustic code by exporting a permeable surface around the propeller for every computational time step and using it as input for the corresponding time step in the aero-acoustic code. This permeable surface remains stationary in time. On this surface, local pressure, density and velocity distributions are defined for each specific time step which are regarded by the code as a source distribution representing the interior of the surface. This distribution logically changes every computational time step and hence simulates the rotating rotor being present in the flow field of the aero-acoustic simulation.

An example of such a surface is depicted in figure 97 and figure 98. In these particular figures, the pressure distribution is depicted, and clearly the influence of the four-bladed rotor present can be observed.

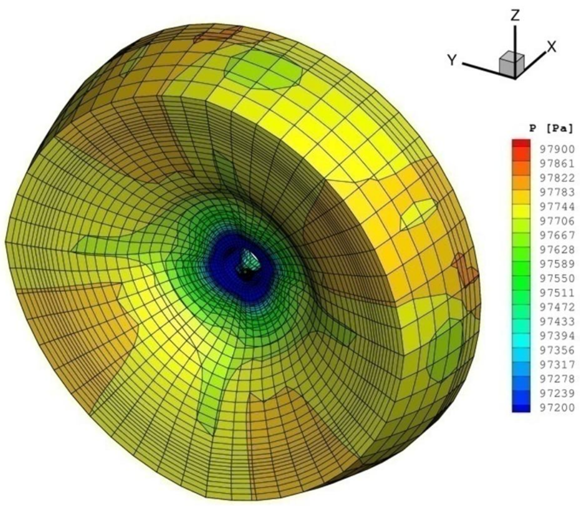

figure 97: extruded surface from UZEN solution(front)

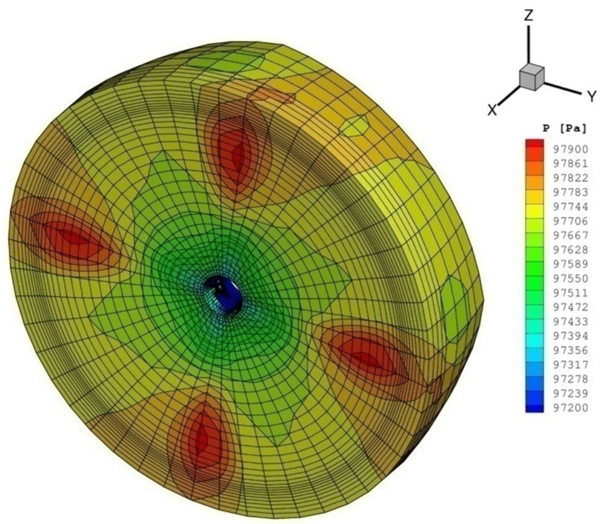

figure 98: extruded surface from UZEN solution(back)

As a guideline, the distance of the surface with respect to the actuator disk is chosen to be about one average chord length from all sides. The influence of this choice will be analyzed further on in the investigation.

Finally, to measure the resulting acoustic output in the far field, microphone carpets with specific size, position and orientation are defined. The choice made in this investigation is depicted in figure 99, and consists of a carpet parallel to the flow and a carpet downstream of the surface orientated parallel to the flow. Both carpets are located sufficiently far from the surface to find far field acoustic data. In future references to the carpets, carpet 1 denotes the carpet that is positioned parallel to the flow direction and carpet 2 refers to the carpet positioned in the wake, orientated perpendicular to the flow direction

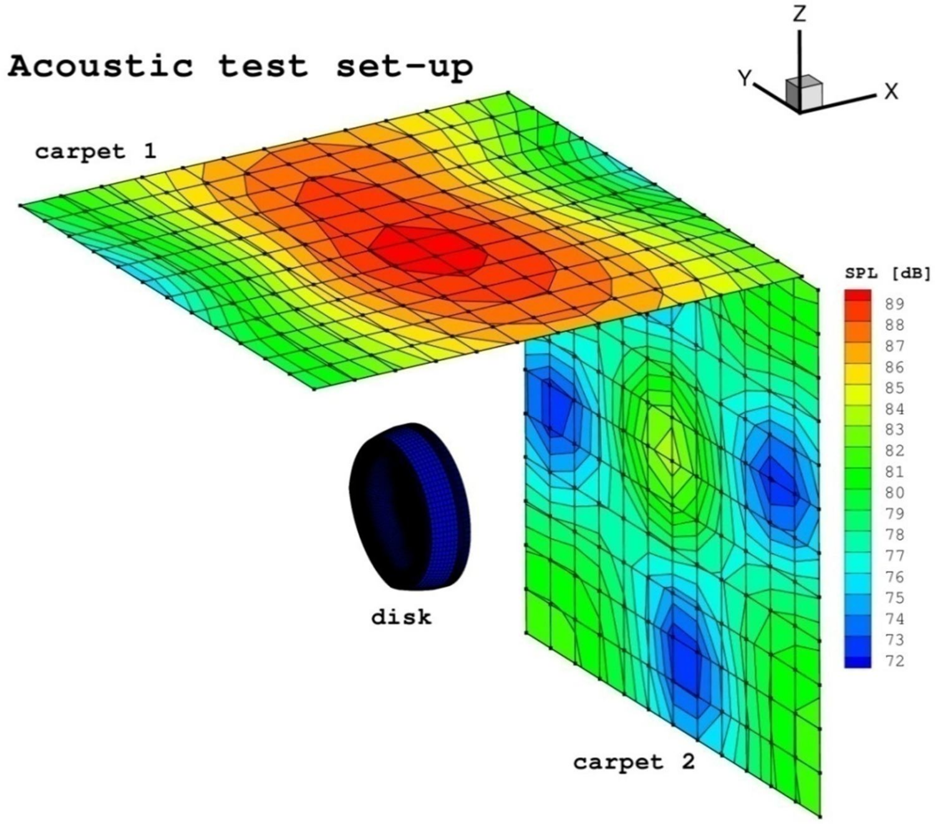

figure 99: Test setup in the aeroacoutic code

The test is relatively simple in nature. Although the input data comes from unsteady CFD simulation, the velocity of rotation of the rotor will be constant, and so a steady harmonic solution is expected. Because the solution is simple in theory this is highly useful since any effects that the usage of UZEN, e.g. the unphysical presence of non-linearity, will become apparent. The downside of this method is that because the test is simple, more complex aero-acoustic phenomena like the effect of a non-axisymmetrical nacelle geometry on the acoustic field, will be beyond the scope of the investigation. Since this is an investigation into the effects that emerge using a CFD code like UZEN in the FW-H code, this is not a problem.

5.3. Results

5.3.1. Tests conducted

In this aero-acoustic analysis, a number of tests are conducted. These tests are listed below, together with their intended objective.

Test	Goal
▪ Coarse vs. dense grid:	• To investigate the effects of accuracy of the CFD solution.
▪ Δ vs. Δ/2 distribution:	• To investigate the effects of the unsteady distribution BC profile
o Coarse vs. dense grid:	o To investigate the effects of accuracy of the CFD solution on this subject.
▪ Guideline surface vs. nearer surface:	• To investigate the influence of the surface distance from the actuator disk
▪ Guideline surface vs. guideline surface without wake surface:	• To investigate the influence of the wake on the accuracy of the aero-acoustic analysis.
o Coarse vs. dense grid:	o To investigate the effects of accuracy of the CFD solution on this subject.

5.3.2. Reference: RAMSYS input data

Depicted below are the resulting microphone carpets from the aero-acoustic simulation done with the RAMSYS input data. The output of the steady harmonic test case is as expected and consists of the unsteady loading (loading noise) and moving geometry (thickness noise) that generate the acoustic noise, hence the emerging dipole profile of the sound pressure levels on the microphone carpets. This result will be used as a reference.

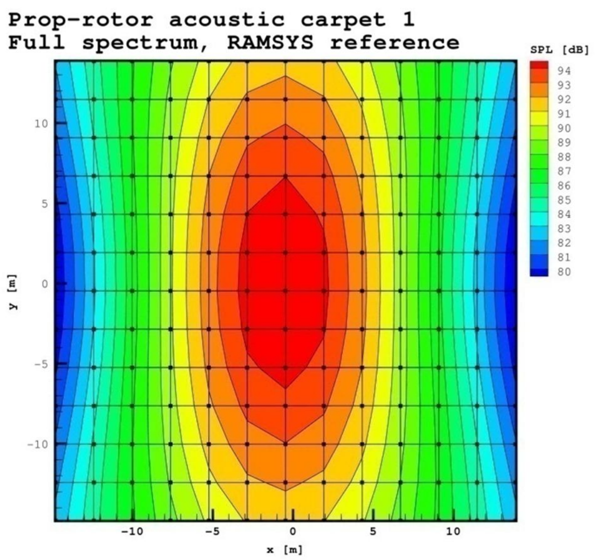

figure 100: Carpet 1, RAMSYS-input

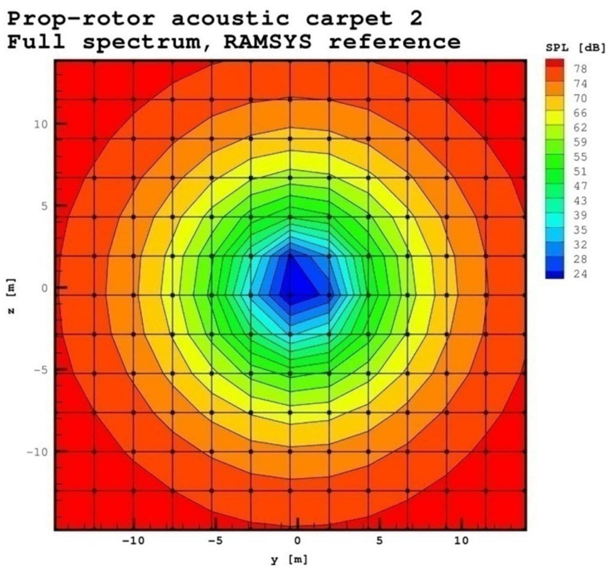

figure 101: Carpet 2, RAMSYS input

5.3.3. Coarse vs. dense grid solution:

In the plots below, the coarse grid output of UZEN is used as aero-acoustic input data.

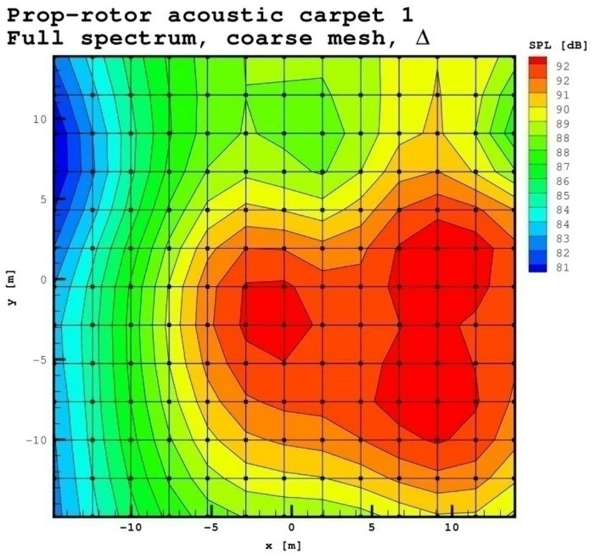

figure 102: Carpet 1, coarse mesh input, Δ

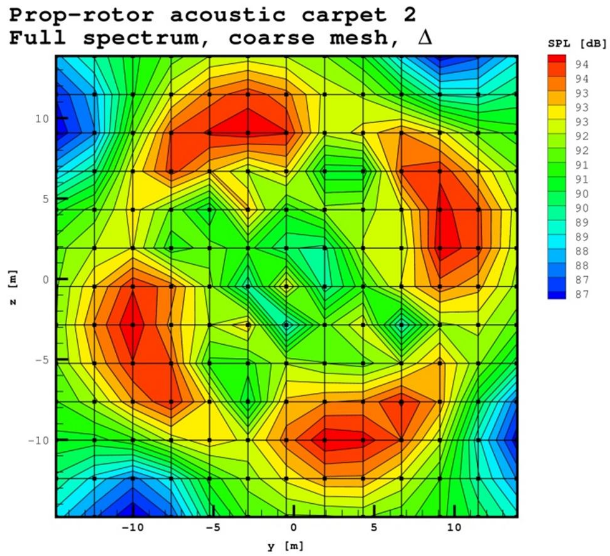

figure 103: Carpet 2, coarse mesh input, Δ

Furthermore, the resulting microphone carpets of the aero-acoustic analysis using the dense grid UZEN-solution as input data is displayed in figure 104 and figure 105.

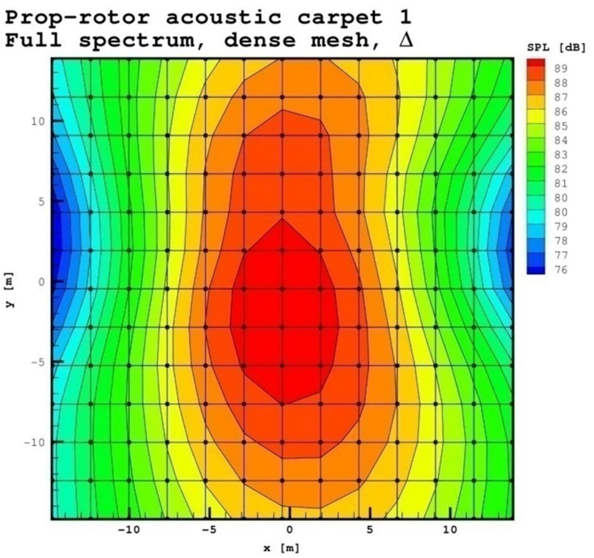

figure 104: Carpet 1, dense mesh input, Δ

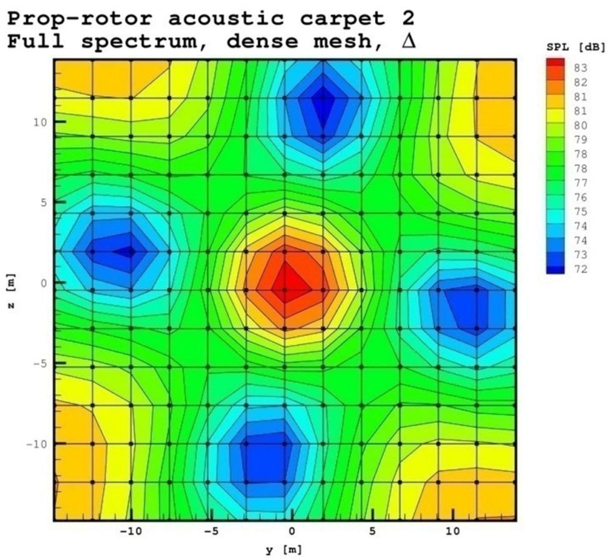

figure 105: Carpet 2, dense mesh input, Δ

What can be observed immediately is the large deviation of local sound pressure levels of the aero-acoustic run with coarse grid input data which renders this data practically unusable. The situation dramatically improves with the dense grid input data, but still on the downstream microphone carpet, a quadrupole-like profile is present, together with the maximum value in the center indicates unphysical non-linearity is generated. This effect can be caused by multiple reasons, discussed in paragraph 5.4.1. For further analysis, the frequency spectrum can be investigated as well:

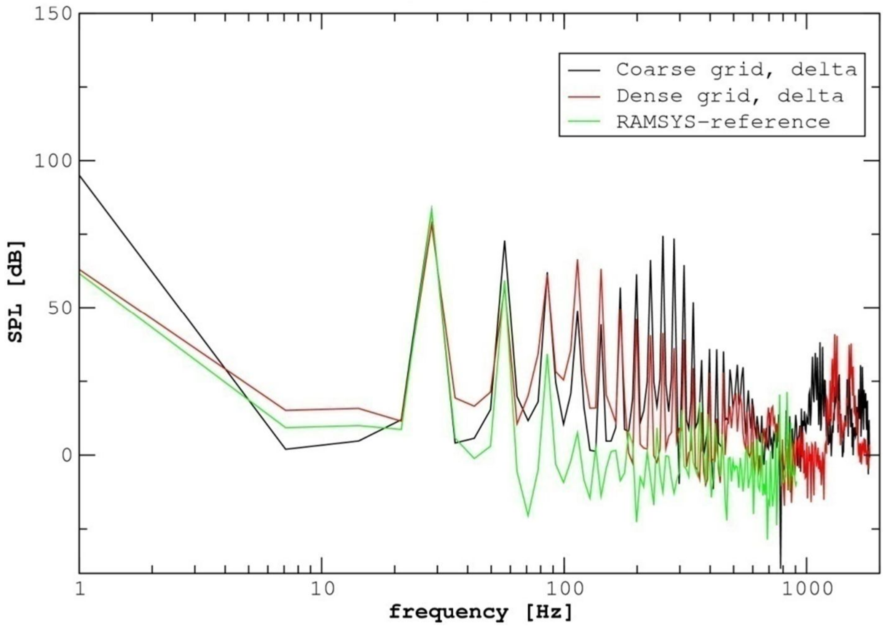

figure 106: frequency spectrum comparison on carpet 1

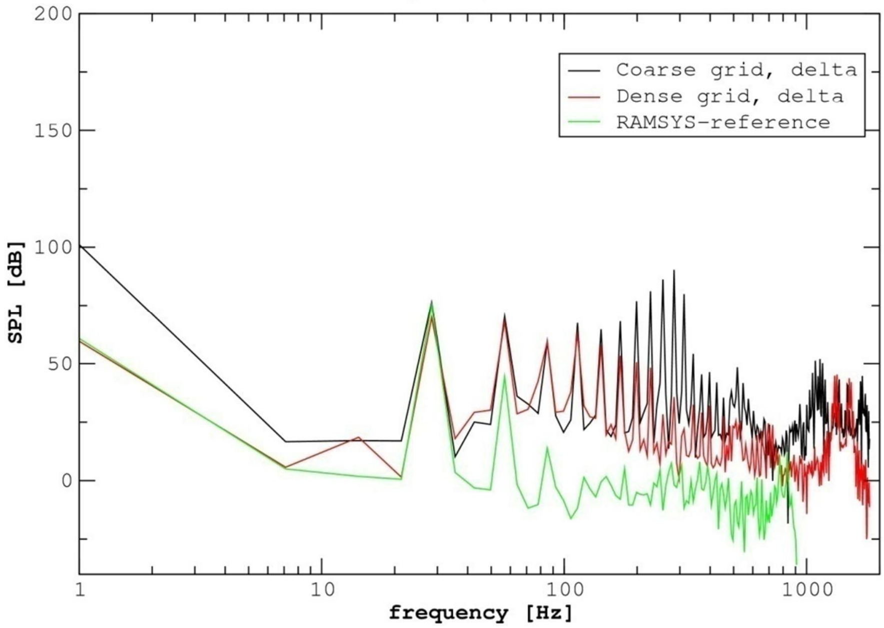

figure 107: frequency spectrum comparison on carpet 2

In figure 106, which displays data from a microphone near the center of the carpet parallel to the flow, we see that the first harmonic at $4 * 7.1$ rps$=28.4$Hz is matched accurately by the aero-acoustic results both the coarse grid and dense grid input. The dense grid also models the second mode with reasonable accuracy, but higher modes are not properly found; High frequency noise is taking over. What is positive about the results is that at least the first 3 harmonics of the UZEN input results are present at the proper frequency. Looking at figure 107, which displays data from a microphone near the center of the carpet perpendicular to the flow direction, we see that the first harmonic is again properly simulated by coarse and dense UZEN solution input data. However, all higher frequency modes are not captured with sufficient accuracy. This decrease of accuracy downstream of the accuracy hints to an influence of the wake on the aero-acoustic solution.

Together with the frequency spectrum, a comparison can be made of the signal on both carpets. figure 108 shows the results on a microphone placed on the carpet perpendicular to the flow. Results show large noise peaks because of second mode error for the simulation with coarse grid input data. The effect is reduced in the plot of the simulation with dense grid input, where the noise due to the second mode is significantly reduced and the noise is due to higher frequencies. The results from a microphone situated on the carpet parallel to the flow, depicted in figure 109 show the same effects, but further increased in magnitude.

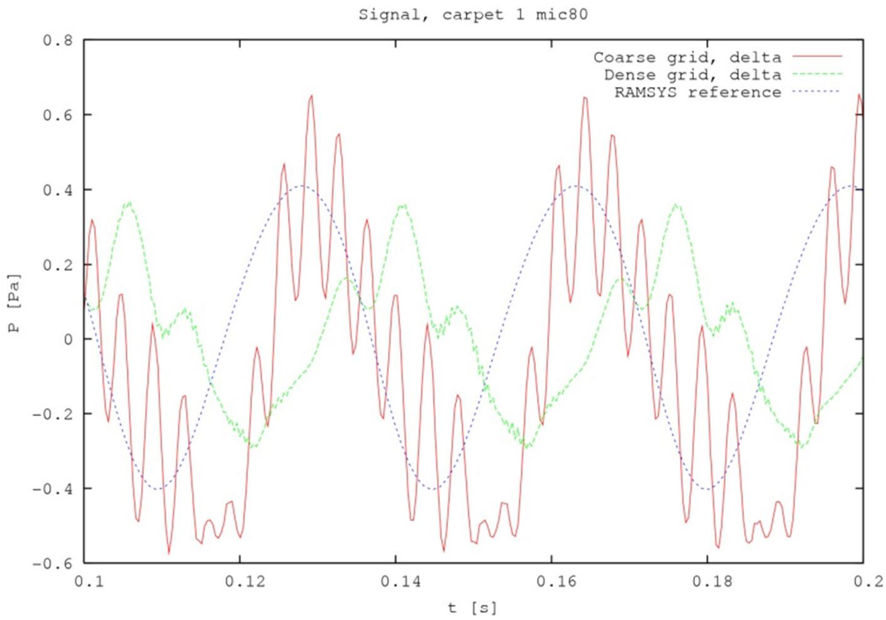

figure 108: Signal comparison on carpet 1

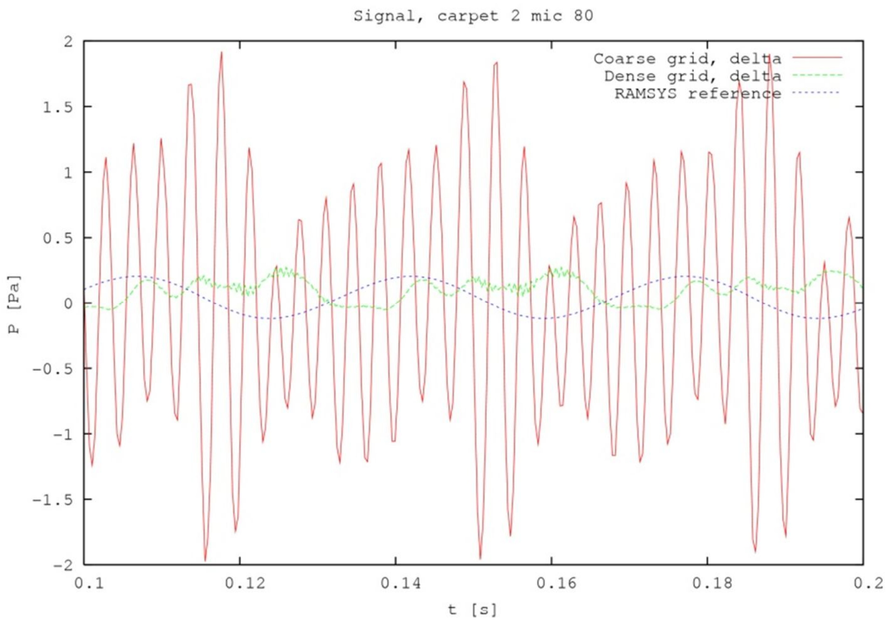

figure 109: Signal comparison on carpet 2

5.3.4. Δ vs. Δ/2 distribution solution

Below, the results with UZEN input using the alternative BC distribution are displayed, for both the coarse and dense grid.

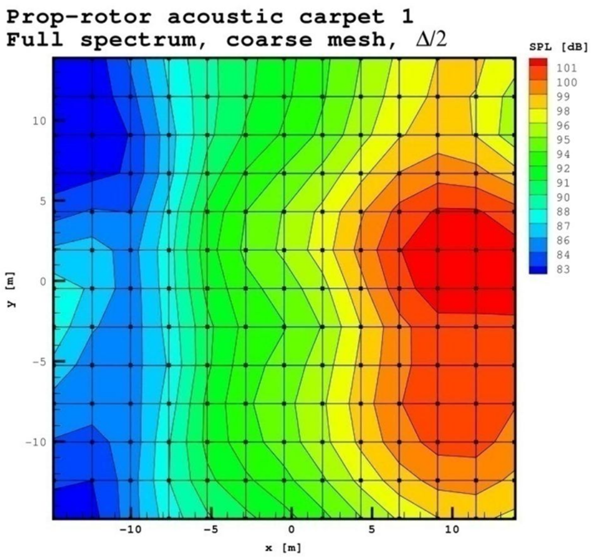

figure 110: Carpet 1, coarse mesh input, Δ/2

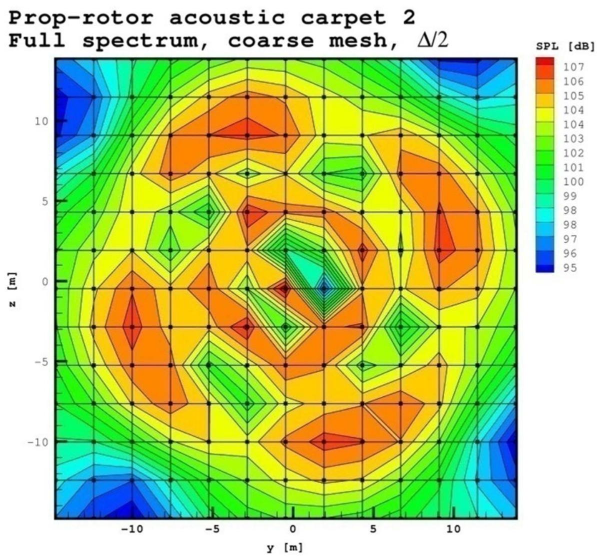

figure 111: Carpet 2, coarse mesh input, Δ/2

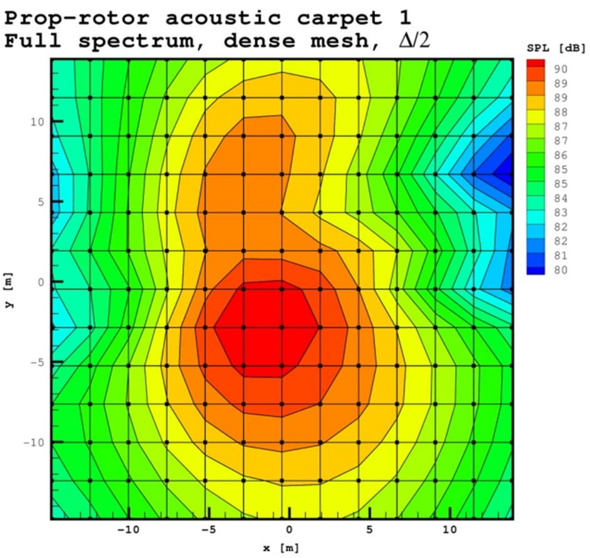

figure 112: Carpet 1, dense mesh input, Δ/2

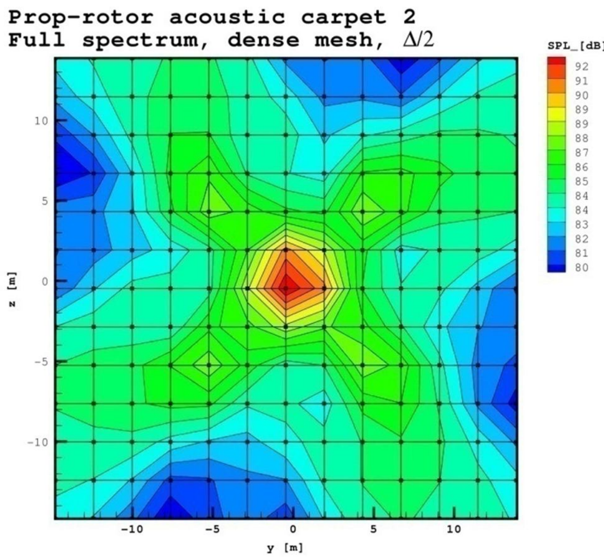

figure 113: Carpet 2, dense mesh input, Δ/2

As was found in the investigation of the CFD solution, decreasing the value of Δ in the unsteady BC-distribution leads to larger errors in the UZEN output. This observation is consistent with figures 102 to 105. When figures 110 to 113 are compared to figures 102 to 105 we see a decrease in accuracy regarding the distribution of sound pressure levels for both the dense and the coarse grid input. Also, the magnitude of sound pressure levels of the aero-acoustic simulation with coarse grid input deviates more with respect to the dense grid input which is again consistent with our previous observations regarding CFD mesh density.

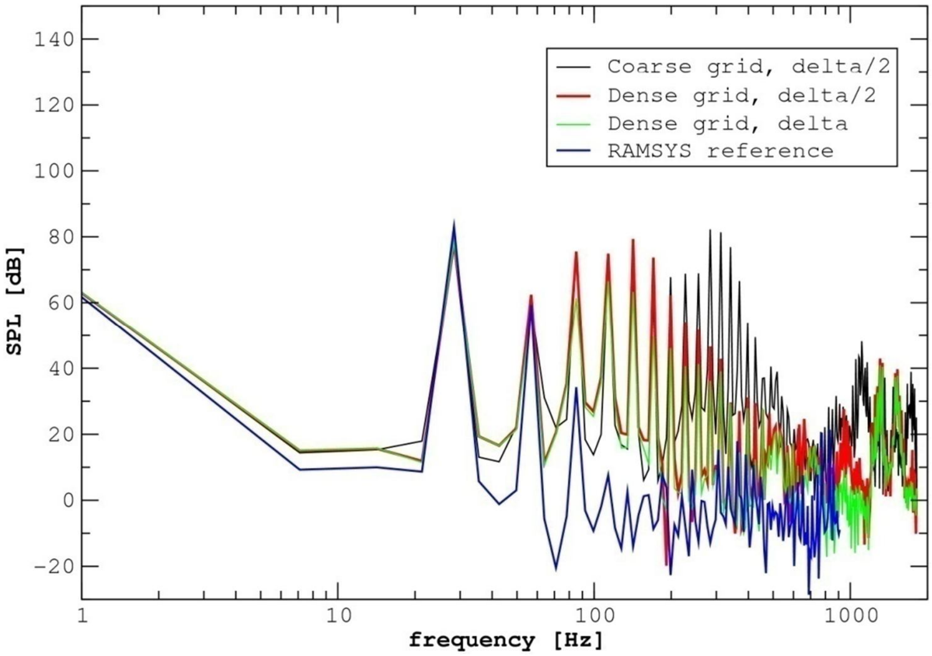

figure 114: frequency spectrum comparison on carpet 1

From the frequency spectrum plot of figure 114 which displays a microphone close to the center on the carpet parallel to the flow direction, it can be concluded that indeed high frequency noise is present with larger amplitude for smaller Δ of the unsteady BC distribution in UZEN. Nevertheless, the first harmonic of the UZEN input data is again properly simulated. This result is also present in figure 115, which represents the frequency spectrum recorded by a microphone on the carpet perpendicular to the flow direction, which was already found to be quite inaccurate. After about 100Hz, the amplitude of the noise goes up with respect to the simulation with original delta size.

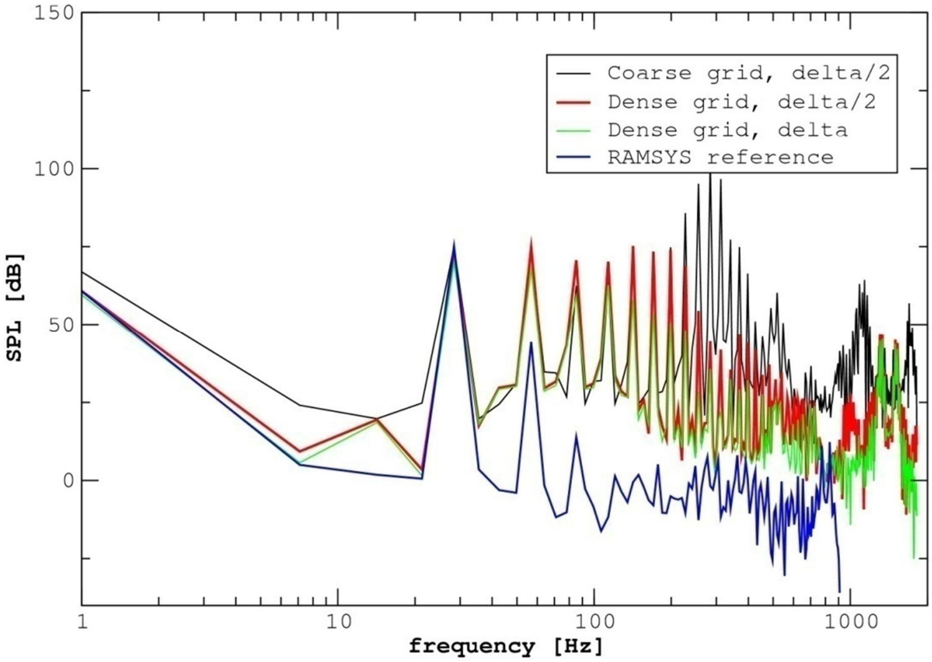

figure 115: frequency spectrum comparison on carpet 2

5.3.5. Guideline surface vs. nearer surface

To test the influence of the chosen surface enclosing the actuator disk data from the UZEN output, a test was made with an alternative surface which is at half the distance from the actuator disk with respect to the guideline surface. Aero-acoustic results are shown below:

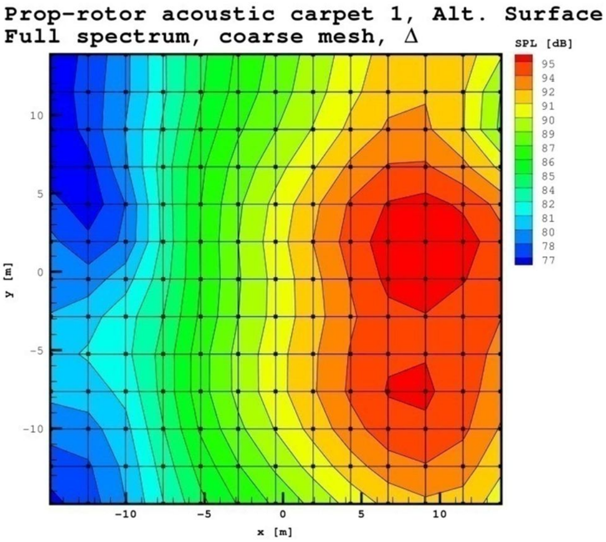

figure 116: Carpet 1, coarse mesh input, Δ, alt. surface

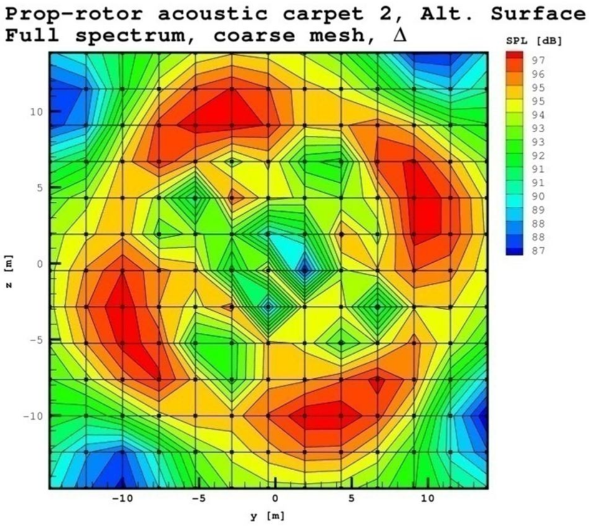

figure 117: Carpet 2, coarse mesh input, Δ, alt surface

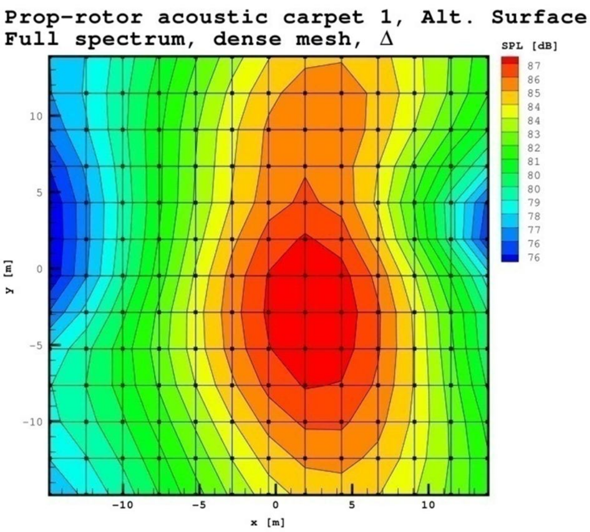

figure 118: Carpet 1, dense mesh input, Δ, alt surface

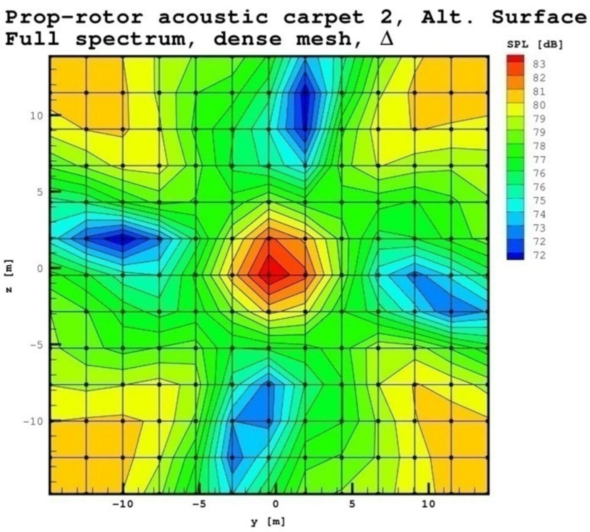

figure 119: Carpet 2, dense mesh input, Δ, alt surface.

The results look reasonably similar to the results with the standard surface, displayed in figures 102 to 105. An analysis in the frequency spectrum is needed to clearly tell the influence.

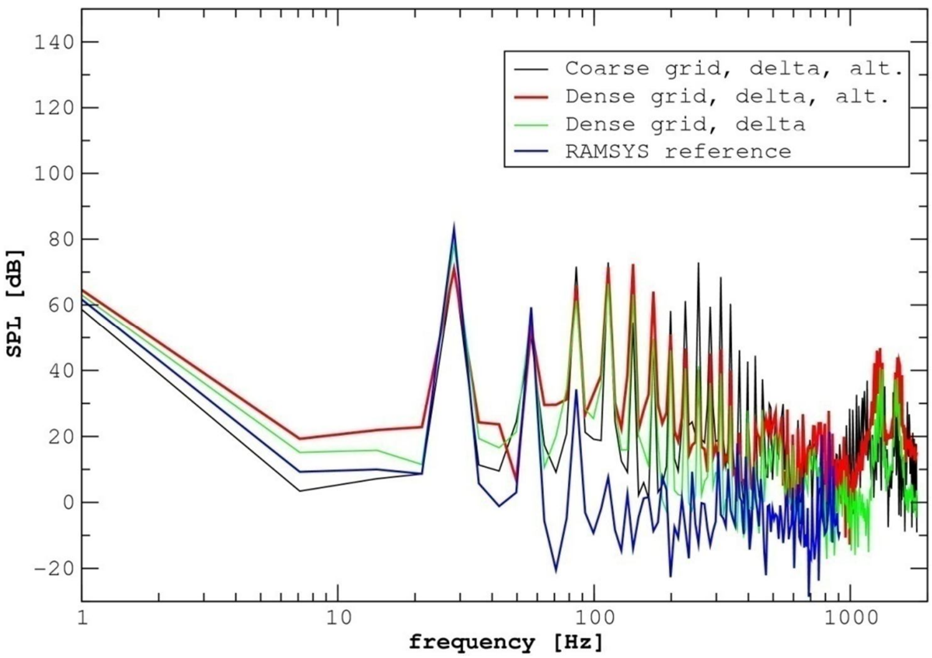

figure 120: frequency spectrum comparison on carpet 1

figure 120 displays a microphone close to the center of the carpet parallel to the flow direction. When closely inspecting the higher frequency spikes of the dense grid input from 100Hz upwards, it can be observed that the peaks have a slightly higher magnitude. In the lower frequencies, this effect is not present. A possible reason for this small high frequency difference is likely due to numerical oscillations. Close to the actuator disk, the sudden discontinuity in momentum is not yet sufficiently smoothed out. The same phenomenon is occurring on the microphone carpet perpendicular to the flow direction. The microphone capture is displayed in figure 121.

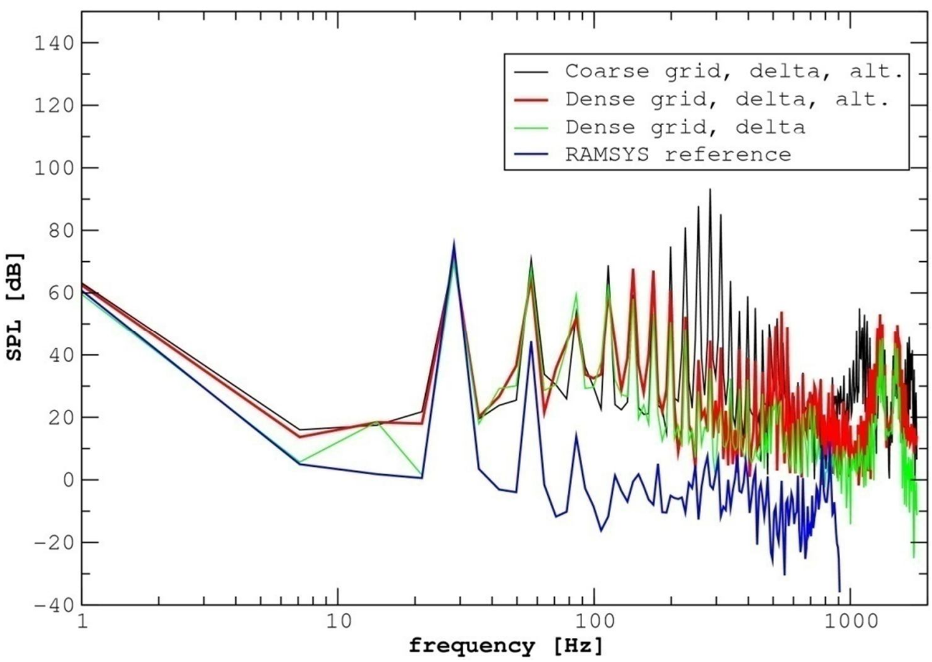

figure 121: frequency spectrum comparison on carpet 2

Another test has to be done with a surface further away from the geometry than the guideline in order to check if the guideline distance is actually a proper one. This test however was not done because of the limited time available for the project. It should be noted that the further away from the actuator disk, the numerical solution will show an error due to artificial dissipation. This justifies in some way that the test has not been done. Nevertheless, the test should be conducted in the future so statements can be made.

5.3.6. Guideline surface vs. guideline surface without wake surface

From the tests of paragraph 5.3.3, it was noticed that the microphones on the carpet parallel to the flow perform better than those that are placed on the carpet in the wake. The effect of the wake in open rotor noise predictions is a general cause for concern as was found by e.g. (Farassat, 2010), because it is difficult to precisely balance the non-linearity with sources on the wake surface. Therefore, a test was conceived with the same surface as the one used in the test of paragraph 5.3.3, however, without a wake surface present. Results are shown below.

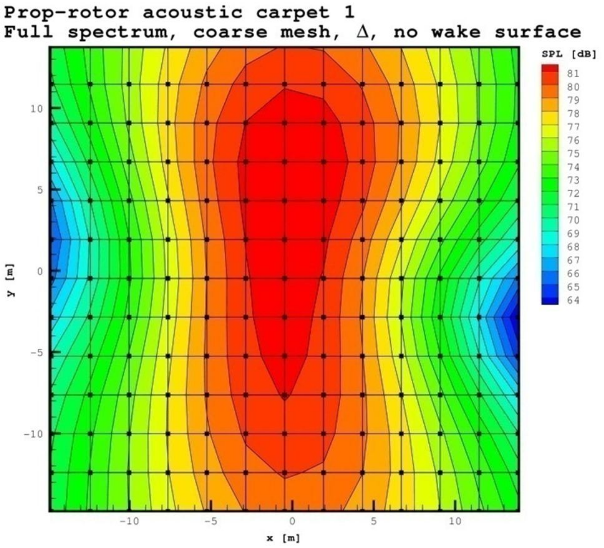

figure 122: Carpet 1, coarse mesh input, Δ, no wake surf.

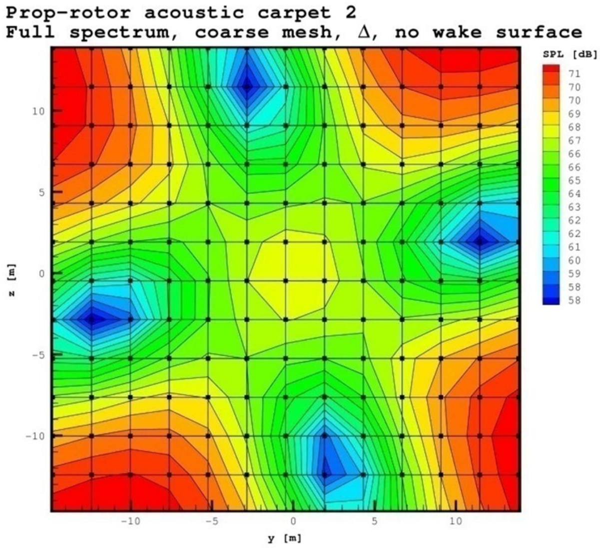

figure 123: Carpet 2, coarse mesh input, Δ, no wake surf.

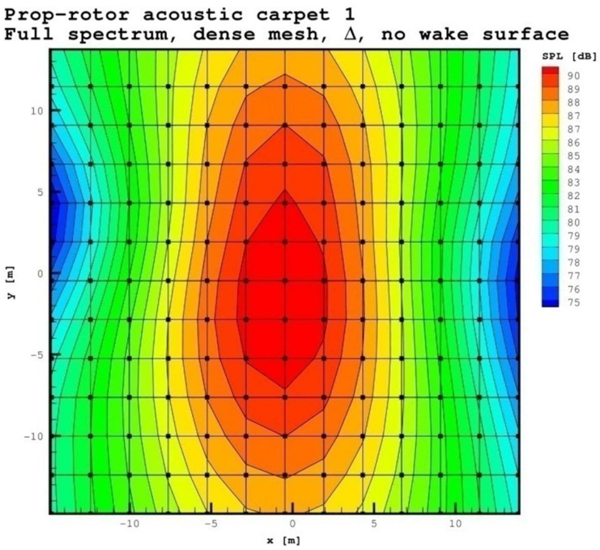

figure 124: Carpet 1, dense mesh input, Δ, no wake surf.

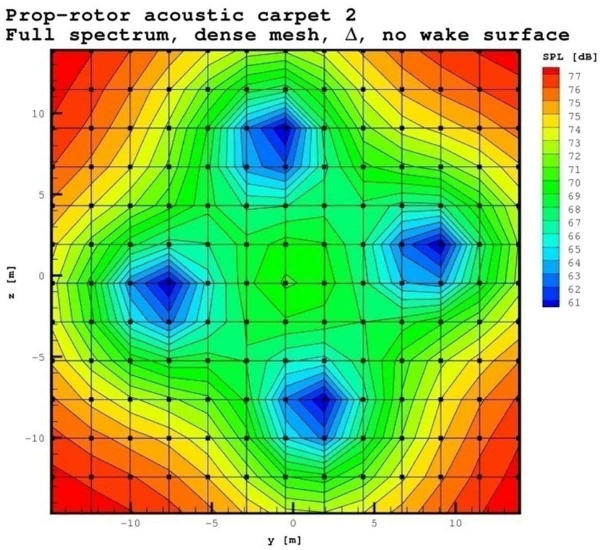

figure 125: Carpet 2, dense mesh input, Δ, no wake surf.

This result is the best so far. Even the aero-acoustic run with the coarse grid UZEN input gives quite a proper SPL distribution on both carpets, even though overall SPL levels are about 10dB too small on the carpet parallel to the flow displayed in figure 122. The SPL levels of the run with the dense grid UZEN input are quite accurate. What is remarkable though is the pattern of low SPL levels on the microphone carpets located in the wake. Since the actual wake surface is gone, this points to a general error in the CFD solution. This phenomenon is very likely a result of interpolation between mesh blocks, as was discussed in paragraph 3.3.3. Further investigation on this phenomenon is needed. However, a large amount of non-physical non-linearity is removed by excluding the wake surface, which is illustrated by the absence of the maximum in SPL in the middle of the wake.

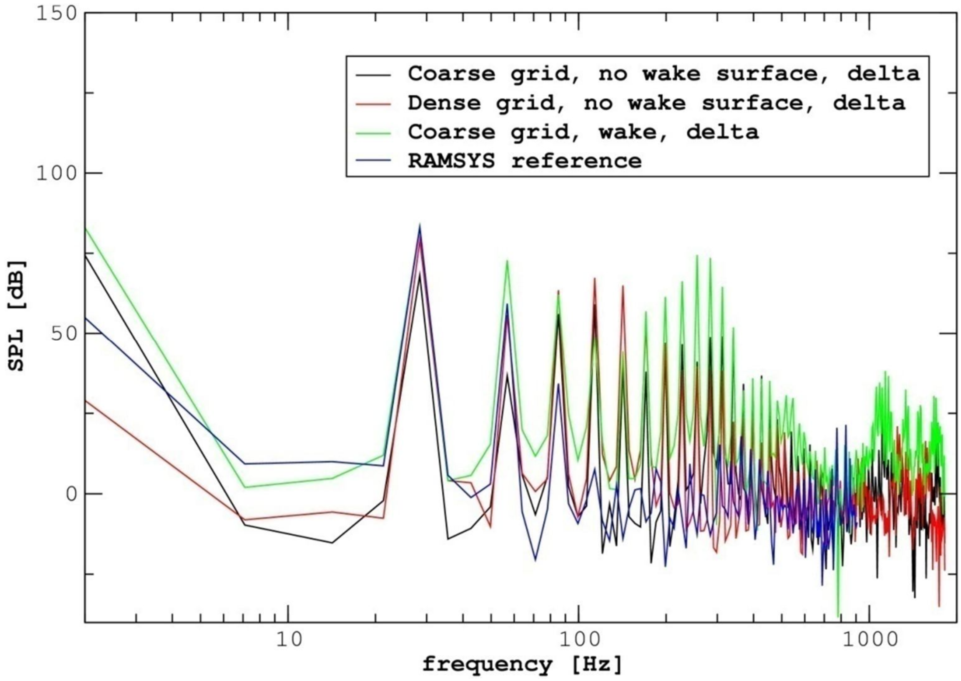

figure 126: frequency spectrum comparison on carpet 1

In figure 126, which again displays the capture of a microphone located close to the center of the carpet parallel to the flow direction. The effect of the missing wake surface results in the large reduction of noise on the simulation with coarse grid input in frequencies in the region higher than 100 Hz. This leads to a very small difference between the simulation with the dense grid input, from which can be concluded that the large errors found in the original simulation with coarse grid input in paragraph 5.3.3 are a result of the inability of the wake surface to balance flow field quantities in an accurate way.

An even more dramatic increase in accuracy is displayed in figure 127. In this figure, a microphone in the center of the carpet in the wake of the actuator disk is displayed. Also visible is the accuracy difference between the simulation with coarse and dense grid input, because the sound pressure levels in the frequency domain around 200 Hz are slightly larger for the coarse grid input.

All in all, it can be concluded that the effect of removing the wake surface significantly increases accuracy of the simulation with coarser grid input to the point where its use is more or less viable. It should be noted that overall sound pressure levels on the carpets are off by 10dB.

Also, since removing the wake surface brings the solution of the simulation with dense and coarse grid input closer together, the result hints to an intrinsic error in the CFD solution. There are a number of possible reasons for this, summed up in the next paragraph.

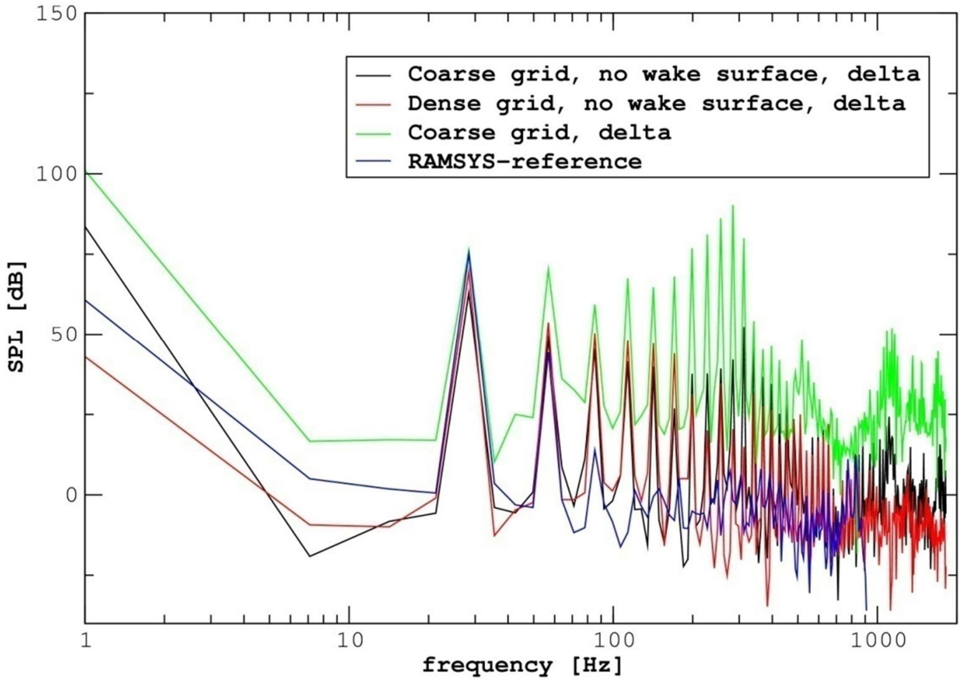

figure 127: frequency spectrum comparison on carpet 2

5.4. Conclusions

From the observations in the results from the tests in chapter 5.3 it is possible to draw a number of conclusions. Before this can be done however, a number of possible error sources should be pointed out as well. This is done in the paragraph below.

5.4.1. Possible error sources in the CFD output

As was observed in paragraph 5.3.6, removing the wake surface increases accuracy. However, high frequency errors still remain for both the coarse and dense grid UZEN input. Possible errors for this might lie in the CFD solutions used as input data. Listed below are possible reasons that contribute to this error:

- As was found in the investigation of the CESAR test case, there is a mesh inconsistency at the nacelle which results in a non-axisymmetrical flow near the nacelle.
- Because of time shortage in the project, the nacelle was not modeled in the RAMSYS simulation of the prop rotor. This inconsistency in the test might have a negative effect in the analysis accuracy.
- In the analysis of the unsteady ZEN simulation of the CESAR test case, it was found that there is an error caused by the interpolation between the blocks of the mesh. (paragraph 3.3.3) The error of interpolation is consistently visible on the microphone carpet perpendicular to the flow direction for all simulations that have some degree of accuracy.
- The UZEN simulation is not completely accurate as can be seen from the convergency plots in paragraph 3.3. The solution is oscillating.

5.4.2. Conclusions from observations

Keeping in mind the possible inaccuracies caused by using a CFD simulation as input data, there are some conclusions that can be made from the tests of chapter 5.3. These conclusions are summarized below.

From paragraph 5.3.3:

- Only the first harmonic mode is simulated with sufficient accuracy for both the dense and coarse grid input.
- Overall SPL levels are more or less correct of the simulation with dense grid input, in contrast to the coarse grid input simulation.
- The unphysical non-linearity present is illustrated the most by the maximum value of SPL in the center of the wake carpet, rendering the use of this simulation for accurate analysis undesirable.

From paragraph 5.3.4:

- Decreasing the Δ in the unsteady ZEN BC distribution leads to larger errors in the CFD solution due to higher gradients in momentum, which is consistently followed by an increase of unphysical non-linearity. These are represented by the more inaccurate distribution of SPL on the microphone carpets and the stronger HF peaks in the frequency spectrum for both tests. From this, it can be concluded that for the sake of accurately modeling a rotor in unsteady ZEN, it is undesirable to use a very dense local distribution of force coefficients in the boundary conditions.

From paragraph 5.3.5:

- Decreasing the distance of the FW-H surface with respect to the actuator disk results in the capture of not sufficiently smoothed out gradients in the flow near the actuator disk. The result of this is the growth of HF(100Hz+) noise peaks. Therefore, it can be concluded that the distance of the surface should be sufficiently far away from the actuator disk.

From paragraph 5.3.6:

As can be found in literature, the influence of the wake surface can impose unphysical non-linearity in the flow, resulting in an inaccurate aero-acoustic result. This is consistent with the results found in the tests done without the wake surface. Non-linearity decreases significantly and this results in:

- The absence of the maximum value of SPL in the middle of the wake
- Accurate simulation of the first two harmonic modes on both carpets using dense grid UZEN input data.
- The accurate SPL distribution and magnitude using the dense grid UZEN input on the surface parallel to the flow direction

5.4.3. Concluding remarks on the use of UZEN as input data for the FW-H code

Overall, it can be concluded that with the use of UZEN input data in the FW-H code is a feasible approach since results are consistently agreeing with the level of accuracy of the UZEN output. It should be noted that for the practical approach of estimating SPL and harmonic modes, a sufficiently accurate CFD simulation should be used, e.g. the UZEN result on the dense grid.

However, the rigor of the investigation is somewhat lacking. There are a number of tests that should be conducted in the future to construct definitive guidelines for the construction of the FW-H surface, as well as construction of the unsteady BCDAT used in UZEN. These tests are listed in chapter 7. The reader will also note that very few quantitative statements are made. This is the case because the present investigation was done purely with a qualitative objective, namely to see if the interface between UZEN and the FW-H code produces feasible results. In order to produce quantitative results, first and foremost, the existing errors in the CFD solution listed in paragraph 5.4.1 should be reduced. Because of the limited time span of this project, this investigation is left to future research.

6. Summary of project conclusions

In this chapter, the conclusions found in the investigation are compactly summarized.

Unsteady ZEN

The unsteady ZEN results for the CESAR test case show good coherence with the steady ZEN result, based on time averaged flow field quantities. Therefore, the chosen method of boundary condition distribution is a good initial guess.

Decreasing the magnitude of Δ increases flow field quantity gradients resulting in a decrease of total pressure due to artificial dissipation in the Euler flow simulations. Furthermore, the more concentrated distribution of boundary condition data increases the total temperature in the flow through a physical phenomenon.

RAMSYS to ZEN data conversion

The conversion between RAMSYS and ZEN using three components of local force coefficients works, but not for every blade geometry. Therefore when employing the method, the time averaged flow field solutions of both approaches should be compared for validation, favorably together with experimental data, in order to establish whether or not the conversion results in realistic ZEN-simulation results.

Ffowcs Williams-Hawkings analysis

From the results of the aero-acoustic simulations it can be qualitatively stated that the unsteady Euler simulation results from ZEN can be used as input data for the FW-H code. However, it should be taken into account that the wake surface of the input data is a source of a lot of noise. When this is considered and circumvented, the first two harmonics and overall sound pressure levels can be estimated with good accuracy using sufficiently accurate input data when simulations are performed with the current choice for input data.

Overall, the main goal of the project was to investigate the feasibility of using unsteady ZEN simulation results as input data for aero-acoustic analysis. After the investigations that were done in the project, it can be stated with some certainty that the approach is indeed feasible. This report should be viewed as a first investigation in the possibility of using this approach. For a more conclusive statement, a number of additional tests should be performed to obtain to increase the scientific rigor of the current investigation. Recommended tests are listed in the following chapter. Ultimately, a test case should be devised to create the possibility to compare the results of UZEN and the aero-acoustic results with experimental data in order to make proper quantitative statements about the approach.

7. Recommendations

After the tests in the project were devised and conclusions were formulated, it was found that a number of tests were missing. Without these tests it is very difficult to make proper statements about the feasibility of the approach that was investigated with full scientific rigor. However, due to the limited time in which the investigation was performed, it was not possible to include these tests in the report. The suggested tests are listed below for future study:

UZEN:

All simulations should be performed again on a grid that is both absolutely axisymmetric and has just one block in tangential direction to limit the inaccuracy caused by interpolation between blocks. The current flow field results show a small contribution of both effects, where the latter is also clearly visible in the aero-acoustic results.

Unsteady boundary condition distribution

A third test should be performed with a larger Δ than the value that results from the chosen guideline. Together with experimental data, this should answer the question whether or not the unsteady boundary condition distribution should incorporate geometrical features of a blade and/or what the optimum value for Δ should be for a given blade/rotor geometry.

In future research, different approaches of boundary condition distribution should also be investigated. The current triangle distribution can perhaps be replaced by a more accurate and realistic distribution.

RAMSYS to ZEN conversion of force coefficient data

In the report a problem was found in the usage of force coefficient data of the APIAN propeller geometry. The resulting flow fields of ZEN and RAMSYS show large differences. Why the approach works for a generic helicopter blade and a generic prop-rotor blade, but fails to give satisfactory results in the APIAN case should be investigated in future studies.

Aero-acoustic analysis

With the errors in the aerodynamic solution reduced as proposed, the aero-acoustic simulations should be performed over again. Very likely the aero-acoustic results will be more accurate for all tests, given that a sufficiently dense grid is used in the aerodynamic simulations.

Furthermore, since it was discovered that the wake surface generates significant noise, different configurations of input data surfaces should be investigated. More specifically a surface that has little to no surface geometry that is perpendicular to the flow direction. An example of this is a cone-like surface that is widely adopted in the analysis of jet wakes.

Overall

The main goal of an investigation into the applicability of integrating UZEN results and the FW-H code is to make qualitative and quantitative statements about the approach and its accuracy. To make quantitative statements, a test case should be devised that includes the capability to compare the results with experimental data in order to do this.

Appendices

I. The Jameson scheme

The ZEN flow solver is based on a finite volume approach which is a Jameson-like quasi second order accurate cell centered method. Because higher order central difference methods are generally very unstable for Euler flows, stability is ensured using artificial dissipation. To illustrate where the dissipative terms show up in the numerical scheme, as well as to show the accuracy of the method, the scheme is explained below. Consider inviscid Euler flow for two spatial dimensions:

$$E = \frac{P}{(\gamma - 1)\rho} + \frac{1}{2}\left(u^2 + v^2\right); \quad H = E + \frac{P}{\rho} \tag{1.1}$$

In integral form, the Euler equations then are:

$$\frac{\partial}{\partial t}\iint_{\Omega} w dx dy + \oint_{\partial\Omega}\left(f dy - g dx\right) = 0 \tag{1.2}$$

Where

$$w = \begin{pmatrix} \rho \\ \rho u \\ \rho v \\ \rho E \end{pmatrix}; \quad f = \begin{pmatrix} \rho u \\ \rho u^2 + p \\ \rho u v \\ \rho u H \end{pmatrix}; \quad g = \begin{pmatrix} \rho v \\ \rho u v \\ \rho v^2 + p \\ \rho v H \end{pmatrix}$$

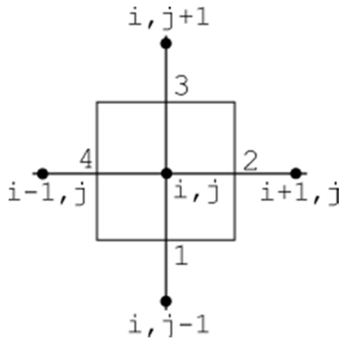

figure 128: depiction of single cell

Consider a grid cell depicted in figure 128. The equation for a single cell is:

$$\frac{d}{dt}(hw) + Qw$$

Where h is the surface of the cell and Q is the flux velocity. Let Δx_k and Δy_k be the increments in x and y direction along side k of the cell. Then the flux balance over the cell for e.g. x-momentum is:

$$\frac{\partial}{\partial t}(hwu) + \sum_{k=1}^{4}\left(Q_k \rho u_k + \Delta y_k p_k\right) = 0, \quad \text{where} \quad Q_k = \Delta y_k u_k - \Delta x_k p_k$$

Each numbered quantity is an average between cells. For instance:

$$(\rho u)_2 = \frac{(\rho u)_{i,j} + (\rho u)_{i+1,j}}{2}$$

In this way the finite volume method is further constructed, which reduces to a second order accurate central difference scheme. Because it is generally known that such a scheme is unstable, measures have to be taken to prevent even-odd coupling and the growth of wiggles in high pressure gradient wiggles. A good way to do this for Euler flow is to introduce artificial dissipation. Therefore, we rewrite the equation for a single cell as:

$$\frac{d}{dt}\left(hw\right)+Qw-Dw=0 \tag{1.3}$$

In this equation, D is the dissipative operator, which is a blend of 2nd and 4th order differences that depend on local pressure gradients. As an illustration on how it is defined, consider the density equation:

$$D\rho = D_x\rho + D_y\rho \tag{1.4}$$

Where

$$\begin{aligned} D_x\rho &= d_{i+1/2,j} - d_{i-1/2,j} \\ D_y\rho &= d_{i,j+1/2} - d_{i,j-1/2} \end{aligned} \tag{1.5}$$

The terms on the right hand side of the equation all have a similar form:

$$d_{i+1/2,j} = \frac{h_{i+1/2,j}}{\Delta t}\left[\varepsilon^{(2)}_{i+1/2,j}\left(\rho_{i+1/2,j}-\rho_{i,j}\right)-\varepsilon^{(2)}_{i+1/2,j}\left(\rho_{i+2,j}-3\rho_{i+1,j}+3\rho_{i,j}-\rho_{i-1,j}\right)\right] \tag{1.6}$$

The coefficients in this equation are adapting to the flow using a pressure sensor. They are defined in the following way. First, we define the pressure sensor:

$$v_{i,j} = \frac{\left|p_{i+1,j}-2p_{i,j}+p_{i-1,j}\right|}{\left|p_{i+1,j}\right|-2\left|p_{i,j}\right|+\left|p_{i-1,j}\right|} \tag{1.7}$$

Then:

$$\varepsilon^{(2)}_{i+1/2,j} = \kappa^{(2)}\max(v_{i+1/2,j},v_{i-1/2,j}) \quad ; \quad \varepsilon^{(4)}_{i+1/2,j} = \max\left(0,\left(\kappa^{(4)}-\varepsilon^{(2)}_{i+1/2,j}\right)\right) \tag{1.8}$$

Where the value for the constants $\kappa^{(2)}$ and $\kappa^{(4)}$ is typically:

$$\kappa^{(2)} = \frac{1}{4} \quad ; \quad \kappa^{(4)} = \frac{1}{256}$$

Now, if we analyze the steps defined above, we notice that $\varepsilon^{(2)}$ is because of the central difference of order $O(\Delta x^2)$, while $\varepsilon^{(4)}$ is of order $O(1)$. Since there are solely undivided differences between brackets in equation (1.6) and the incremental surface $h_{i+1/2,j}$ is $O(\Delta x)$, the difference operator D is $O(\Delta x^3)$ accurate. Otherwise when the flow isn't sufficiently smooth, i.e. shock waves are present, the pressure sensor will become of $O(1)$ and the scheme will behave locally as a first order scheme.

II. Definition of ZEN AD force model input data

The actuator disk BCDAT for the force model contains the non-dimensional force coefficients

$\frac{dC_a}{d\bar{r}}$:local thrust coefficient per unit radius

$\frac{dC_p}{d\bar{r}}$:local power coefficient per unit radius

$\frac{dC_r}{d\bar{r}}$:local radial force coefficient per unit radius

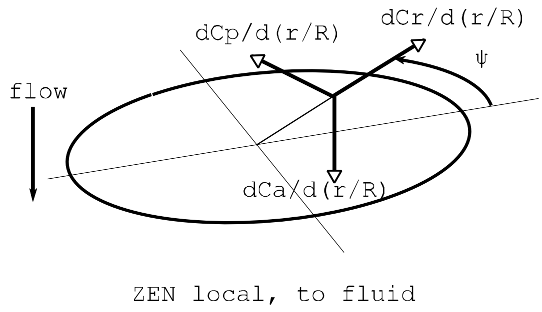

figure 129: ZEN axis definition, force from AD to fluid

Where $\bar{r}$ is the non-dimensional radius r / R_{tip}.

These coefficients are acting in the direction illustrated in figure 129 and defined using the non-dimensionalization of thrust, power and radial force proposed by Renard, in the following way.

II.I. Local thrust coefficient per unit radius:

The non-dimensional thrust coefficient is defined by Renard as(see nomenclature for symbol definitions):

$$C_a = \frac{T}{\rho_\infty n^2 D^4} \tag{2.1}$$

Where T is the thrust produced by N blades together, therefore:

$$T = NT_{blade} \tag{2.2}$$

Substituting this into the definition of the trust coefficient leads to:

$$NdT_{blade} = \rho_\infty n^2 D^4 \, C_a \tag{2.3}$$

or:

$$\frac{dT_{blade}}{d\bar{r}} = \frac{\rho_\infty n^2 D^4}{N} \frac{dC_a}{d\bar{r}} \tag{2.4}$$

$$\frac{dT_{blade}}{d\bar{r}} = \frac{\rho_\infty n^2 D^4}{N} \frac{dC_a}{d\bar{r}} \tag{2.5}$$

Using the definition of the advance ratio $J = V_\infty / nD$ this becomes:

$$\frac{dT_{blade}}{d\bar{r}} = \frac{\rho_\infty {V_\infty}^2 D^2}{NJ^2} \frac{dC_a}{d(r/R)} \rightarrow \tag{2.6}$$

$$\boxed{\frac{dC_a}{d\bar{r}} = \frac{NJ^2}{\rho_\infty V_\infty{}^2 D^2} \frac{dT_{blade}}{d\bar{r}}} \tag{2.7}$$

II.II. Local power coefficient per unit radius:

The non-dimensional power coefficient defined by Renard is defined as(see nomenclature for symbol definitions):

$$C_p = \frac{P}{\rho_\infty n^3 D^5} \tag{2.8}$$

Where p is the power produced by N blades together, therefore:

$$P = NP_{blade} \tag{2.9}$$

Substituting this into the definition of the power coefficient leads to:

$$NdP_{blade} = \rho_\infty n^3 D^5 C_p \tag{2.10}$$

or:

$$\frac{dP_{blade}}{d\bar{r}} = \frac{\rho_\infty n^3 D^5}{N} \frac{dC_p}{d\bar{r}} \tag{2.11}$$

$dP_{blade} / d\bar{r}$ can also be written as:

$$2\pi n\bar{r}R \frac{dF_{\theta blade}}{d\bar{r}}$$

Furthermore, using the definition of the advance ratio $J = V_\infty / nD$ equation (2.11) can be rewritten as

$$2\pi n\bar{r}R \frac{dF_{\theta blade}}{d\bar{r}} = \frac{\rho_\infty n V_\infty{}^2 D^3}{NJ^2} \frac{dC_p}{d\bar{r}} \rightarrow \tag{2.12}$$

$$\boxed{\frac{dC_p}{d\bar{r}} = \frac{2\pi NJ^2 \bar{r}R}{\rho_\infty V_\infty{}^2 D^3} \frac{dF_{\theta blade}}{d\bar{r}}} \tag{2.13}$$

II.III. Local radial coefficient per unit radius:

The non-dimensional radial force coefficient is defined by Renard as (see nomenclature for symbol definitions):

$$C_r = \frac{F_R}{\rho_\infty n^2 D^4} \tag{2.14}$$

Where F_R is the radial force produced by N blades together, therefore:

$$F_R = NF_{Rblade} \tag{2.15}$$

Substituting this into the definition of the radial force coefficient leads to:

$$NdF_{Rblade} = \rho_\infty n^2 D^4 \, C_r \tag{2.16}$$

or:

$$\frac{dF_{Rblade}}{d\overline{r}} = \frac{\rho_\infty n^2 D^4}{N} \frac{dC_r}{d\overline{r}} \tag{2.17}$$

Using the definition of the advance ratio $J = V_\infty / nD$ this becomes:

$$\frac{dF_{Rblade}}{d\overline{r}} = \frac{\rho_\infty V_\infty{}^2 D^2}{NJ^2} \frac{dC_r}{d\overline{r}} \rightarrow \tag{2.18}$$

$$\boxed{\frac{dC_r}{d\overline{r}} = \frac{NJ^2}{\rho_\infty V_\infty{}^2 D^2} \frac{dF_{Rblade}}{d\overline{r}}} \tag{2.19}$$

III. RAMSYS output conversion

The non-dimensional RAMSYS output data in the tip path plane frame of reference is defined as:

$C_N M_l^2$: local force coefficient in normal direction multiplied by the local Mach number squared.

$C_A M_l^2$: local force coefficient in chordwise direction multiplied by the local Mach number squared.

$C_Y M_l^2$: local force coefficient in spanwise direction multiplied by the local Mach number squared.

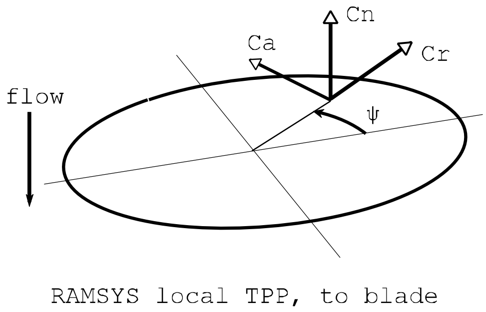

figure 130: RAMSYS TPP axis directions, force from fluid to blade

where $M_l = V_l / a_\infty$ and V_l is the local tangential velocity of the blades. Note also that these are coefficients of the forces acting from to fluid to the blade and act in the direction illustrated in figure 130. They are transformed to the desired output in the following way:

III.I. Local force coefficient in normal direction

The local normal force coefficient is defined as:

$$C_N = \frac{dN}{\frac{1}{2}\rho_\infty V_l^2 c(r) dr} \tag{3.1}$$

Where dN is the normal force on the blade segment in [N], V_l is the local tangential velocity in [m/s], c is the local chord length in [m] and dr is the length of the blade segment in spanwise direction in [m]. The tangential velocity for this simplified case is equal to:

$$V_l = \omega r \tag{3.2}$$

Where ω is the rotational velocity of the propeller in [rad/s]. Equation (3.1)can be rewritten to:

$$\frac{dN}{dr} = \frac{1}{2}\rho_\infty V_l^2 c(r) C_N \tag{3.3}$$

Which can conveniently be rewritten using the definitions of the Mach number and the speed of sound:

$$\frac{dN}{dr} = \frac{1}{2}\rho_\infty c\left(C_N M_l^2\right) = \frac{1}{2}\gamma P_\infty c\left(C_N M_l^2\right) \tag{3.4}$$

This expression uses the RAMSYS output data parameter $C_N M_l^2$. Furthermore:

$$\boxed{\frac{dT_{blade}}{d\bar{r}} = \frac{dN}{dr}R = \frac{1}{2}\gamma P_\infty c\left(C_N M_l^2\right)R} \tag{3.5}$$

III.II. Local force coefficient in chordwise direction

The local force coefficient in chordwise direction is defined as:

$$C_A = \frac{dA}{\frac{1}{2}\rho_\infty V_l^2 c\, dr} \tag{3.6}$$

Where dA is the local force coefficient in chordwise direction of a blade segment in [N], V_l is again the local tangential velocity in [m/s], c is the chord length in [m] and dr is the length of the blade segment in spanwise direction in [m]. Equation (3.6)can be rewritten to:

$$\frac{dA}{dr} = \frac{1}{2}\rho_\infty V_l^2 c\, C_A \tag{3.7}$$

This again can conveniently be rewritten using the definitions of the Mach number and the speed of sound:

$$\frac{dA}{dr} = \frac{1}{2}\rho_\infty c\left(C_A M_l^2\right) = \frac{1}{2}\gamma P_\infty c\left(C_A M_l^2\right) \tag{3.8}$$

This expression uses the RAMSYS output data parameter $C_A M_l^2$. Furthermore:

$$\boxed{\frac{dF_{\theta blade}}{d\overline{r}} = \frac{dA}{dr} R = \frac{1}{2}\gamma P_\infty c\left(C_A M_l^2\right) R} \tag{3.9}$$

III.III. Local force coefficient in spanwise direction

The local force coefficient in spanwise direction is defined as:

$$C_Y = \frac{dY}{\frac{1}{2}\rho_\infty V_l^2 c\, dr} \tag{3.10}$$

Where dY is the local force coefficient in spanwise direction of a blade segment in [N], V_l is again the local tangential velocity in [m/s], c is the chord length in [m] and dr is the length of the blade segment in spanwise direction in [m]. Equation (3.10)can be rewritten to:

$$\frac{dY}{dr} = \frac{1}{2}\rho_\infty V_l^2 c\, C_Y \tag{3.11}$$

This again can conveniently be rewritten using the definitions of the Mach number and the speed of sound:

$$\frac{dY}{dr} = \frac{1}{2}\rho_\infty c\left(C_Y M_l^2\right) = \frac{1}{2}\gamma P_\infty c\left(C_Y M_l^2\right) \tag{3.12}$$

This expression uses the RAMSYS output data parameter $C_Y M_l^2$. Furthermore:

$$\frac{dF_{Rblade}}{d\overline{r}} = \frac{dY}{dr} R = \frac{1}{2}\gamma P_\infty c\left(C_Y M_l^2\right) R \tag{3.13}$$

IV. Axis directions

Before the local force coefficient in normal, chordwise and spanwise direction can be converted to ZEN AD force model data, the definition of the used frames of reference have to be investigated in order to ensure correctness of the signs. This investigation is done in this paragraph.

IV.I. ZEN AD-axis directions (from biprop.f)

Consider an actuator disk located at $\vec{x}_c = \vec{0}$. The unit vector perpendicular to the disk is $\vec{A} = (1,0,0)$ and points downstream, i.e. along the x-axis. The vector directions are determined in the following way:

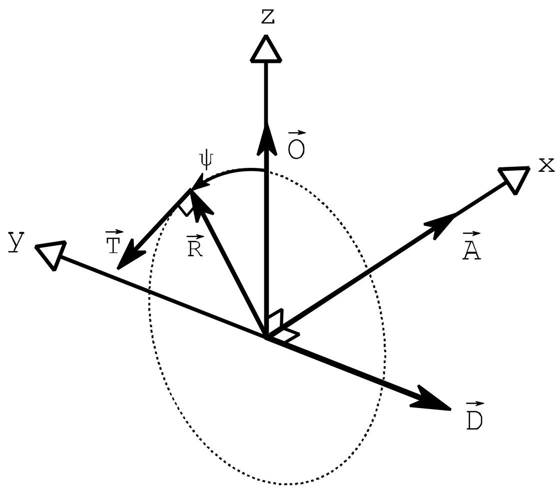

figure 131: Construction of ZEN axis directions from code

First, define the vector $\vec{O}$:

$$y_O = 0,\ z_O = \frac{x_A^2}{\sqrt{y_A^2 + z_A^2}}, x_O = -\frac{z_O \cdot z_A}{x_A}$$

Then, define the vector $\vec{D}$:

$$\vec{D} = \vec{A} \times \vec{O}$$

Furthermore, the radial vector is calculated as $\vec{R} = (\vec{x} - \vec{x}_c) / \left|\vec{x} - \vec{x}_c\right|$. The tangential vector is defined as $\vec{T} = \vec{R} \times \vec{A}$. This result in the vector directions depicted in figure 131, in which $\vec{A} = (1,0,0)$. These vectors can be used to define the starting point and the direction of ψ. In order to do this, define:

$$R_{xp} = \min(1.0, \max(-1.0, \vec{R} \cdot \vec{O}))$$

$$R_D = \vec{R} \cdot \vec{D}$$

In ZEN, ψ is defined using these values as:

$$\psi = \begin{cases} \frac{180}{\pi} - \cos^{-1}(R_{xp}) & \text{if } R_D < 0 \\ 360 - \frac{180}{\pi}\cos^{-1}(R_{xp}) & \text{if } R_D \geq 0 \end{cases}$$

So ψ starts at $\vec{O}$ and is positive in the direction depicted in figure 131. This results in a force coefficient frame of reference shown in figure 129.

IV.II. RAMSYS tip path plane axis directions

The default RAMSYS output on the tip path plane consists of force coefficient data in the Cartesian frame of reference, depicted in figure 132. To convert this data to a local system, a transformation to polar coordinates with variables r, ψ and z is required, depicted in figure 133:

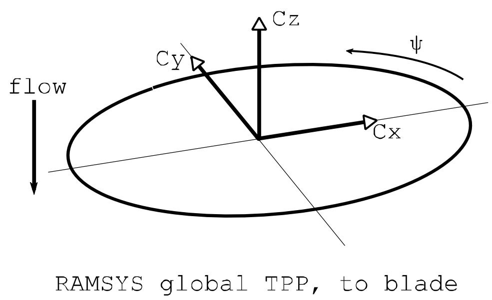

figure 132: RAMSYS TPP force directions, Cartesian coordinates from fluid to blade

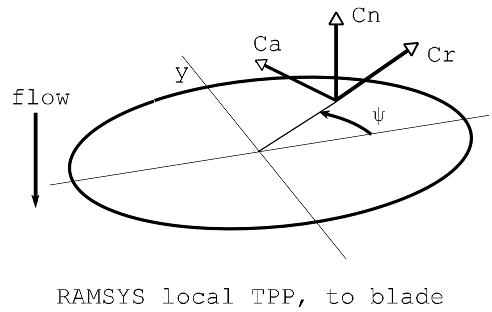

figure 133: RAMSYS TPP force directions, polar coordinates from fluid to blade

The transformation of the coefficients is done in the following way:

$$\boxed{\begin{array}{c} C_n(r,\psi)=C_z(r,\psi) \\ C_a(r,\psi)=-C_x(r,\psi)\sin\psi+C_y(r,\psi)\cos\psi \\ C_r(r,\psi)=C_x(r,\psi)\cos\psi+C_y(r,\psi)\sin\psi \end{array}} \tag{4.1}$$

Because ZEN uses force coefficients for defining the force <u>from</u> the blade <u>on</u> the fluid, another transformation is required: $C_n(r,\psi)=-C_n(r,\psi)$, $C_a(r,\psi)=-C_a(r,\psi)$, $C_r(r,\psi)=-C_r(r,\psi)$. This results in the force coefficients orientation depicted in figure 134. The axis orientation in ZEN is illustrated in figure 135. In ZEN the force coefficient in <u>downstream</u> direction is <u>positive</u> for a propeller moving <u>upstream</u>. Because this is exactly the opposite in RAMSYS, another similar transformation has to be done: $C_n(r,\psi)=-C_n(r,\psi)$, $C_a(r,\psi)=-C_a(r,\psi)$, $C_r(r,\psi)=-C_r(r,\psi)$. Note that after multiplying the coefficients twice by -1 the situation of equation (4.1) is restored, however they apply on a different FOR.

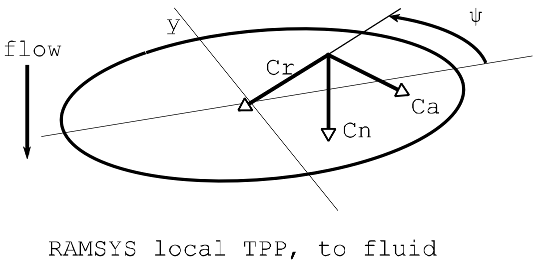

figure 134: RAMSYS TPP force directions, polar coordinates from blade to fluid

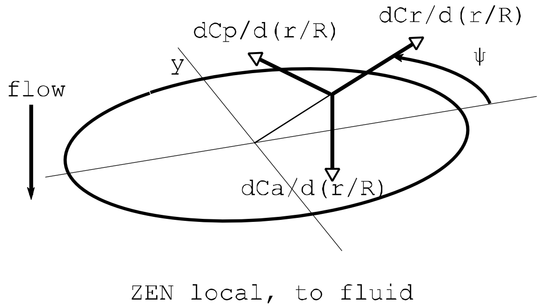

figure 135: ZEN axis definition, force from AD to fluid

Comparing figure 134 with figure 135 one finds that in order to make the correct force coefficient transformation from RAMSYS to ZEN, the following operations have to be done after the transformation to the polar coordinate system in order to ensure the forces to be in the proper direction:

$$\boxed{C_n = C_n,\; C_a = -C_a,\; C_r = -C_r} \tag{4.2}$$

V. Ffowcs Williams – Hawkings analogy

The following derivation is a more detailed description of the steps provided by (Casalino, 2003). Consider an arbitrary stationary volume V in space enclosed by a surface Σ. Suppose the volume V is divided into two sub-volumes 1 and 2 by a smooth surface of discontinuity S. Let $\vec{l}$ be the outward normal from V and let $\vec{n}$ be the unit normal going from region 1 to region 2. The change of mass inside the volume is:

$$\frac{\partial}{\partial t}\int_V \rho dV = \frac{\partial}{\partial t}\int_{V^{(1)}} \rho^{(1)} dV + \frac{\partial}{\partial t}\int_{V^{(2)}} \rho^{(2)} dV \tag{5.1}$$

For each region:

$$\frac{\partial}{\partial t}\int_{V^{(1)}} \rho^{(1)} dV = -\int_{\Sigma^{(1)}=0} \left(\rho u_i\right)^{(1)} l_i d\Sigma - \int_S \left[\rho(u_i - v_i)n_i\right]^{(1)} dS$$

So equation (5.1) becomes:

$$\frac{\partial}{\partial t}\int_V \rho dV = -\int_\Sigma \left(\rho u_i\right) l_i d\Sigma + \int_S \left[\rho\left(u_i - v_i\right)\right]_{(1)}^{(2)} n_i dS$$

Applying the divergence theorem and using the fact that we are dealing with a stationary volume allows us to write:

$$\int_V \left[\frac{\partial \rho}{\partial t} + \frac{\partial}{\partial x_i}\left(\rho u_i\right)\right] dV = \int_S \left[\rho\left(u_i - v_i\right)\right]_{(1)}^{(2)} n_i dS \tag{5.2}$$

Suppose the surface S is defined by $f(\vec{x},t) = 0$ so that $f < 0$ is region 1 and $f > 0$ is region 2. It is possible to replace the surface integral on the right hand side of the equation by a volume integral using the results of generalized function theory (JONES, 1966). For instance. We can use a generalized function that uses a volume integral containing delta functions:

$$\int_{-\infty}^{\infty} F(\vec{z})\delta(g(\vec{z}))d\vec{z} = \int_{\Sigma_k} \frac{F}{|\nabla g|}\left(\vec{z}^*\right) d\Sigma \tag{5.3}$$

Where $|\nabla g|^2 = \left(\partial g / \partial z_k\right)^2$ and $\vec{z}^*$ is a point on the surface Σ_k defined by $g(\vec{z}^*) = 0$. Here, Σ_k is the projection of the surface onto the plane that has its normal in k direction.

We can use this expression conveniently because S is defined by $f(\vec{z}) = 0$, i.e. the right hand side of equation (5.2) is compatible. However, we do have to multiply the integrand of this part of the equation by the divergence of f. After having done this, we can use expression (5.3) and find that:

$$\int_V \left[\frac{\partial \rho}{\partial t} + \frac{\partial}{\partial x_i}(\rho u_i) \right] dV = \int_{-\infty}^{\infty} \left[\left[\rho(u_i - v_i) \right]_{(1)}^{(2)} \delta(f) \frac{\partial f}{\partial x_i} \right] dV$$

Because $\delta(f)$ is a one dimensional delta function which is zero everywhere except at $f = 0$ (which is contained within V), we can take the integrand out of the integral on both sides of the equation without any problems to find the generalized equation for conservation of mass:

$$\frac{\partial \rho}{\partial t} + \frac{\partial}{\partial x_i}(\rho u_i) = \left[\rho(u_i - v_i) \right]_{(1)}^{(2)} \delta(f) \frac{\partial f}{\partial x_i} \tag{5.4}$$

This equation implies that in order to keep the fluid in its defined state, a shell distribution of sources is needed. This distribution of sources has to have the same strength as the difference between the mass flux requirements of each region. The same procedure can be done on conservation of momentum to find the generalized momentum equation:

$$\frac{\partial}{\partial t}(\rho u_i) + \frac{\partial}{\partial x_i}(\rho u_i u_j + P_{ij}) = \left[P_{ij} + \rho u_i (u_j - v_j) \right]_{(1)}^{(2)} \delta(f) \frac{\partial f}{\partial x_j} \tag{5.5}$$

Where $P_{ij} = (p - p_0)\delta_{ij} - \tau_{ij}$ is the compressive stress tensor. Note that these equations govern the unbounded fluid and that the source terms disappear if there are no discontinuities present in the domain. The only requirement on the discontinuity is that its surface has to be smooth and differentiable. Also note that

Now suppose that region 1 is the interior of the permeable surface S and suppose that here, the fluid is at rest:

$$P' = 0, \quad \rho = \rho_0, \quad \vec{u} = \vec{0}$$

Also, note that $\partial f / \partial x_i$ in this case is the unit normal outward of the surface. Region 2 is the exterior of the surface. Equation (5.4) now reads:

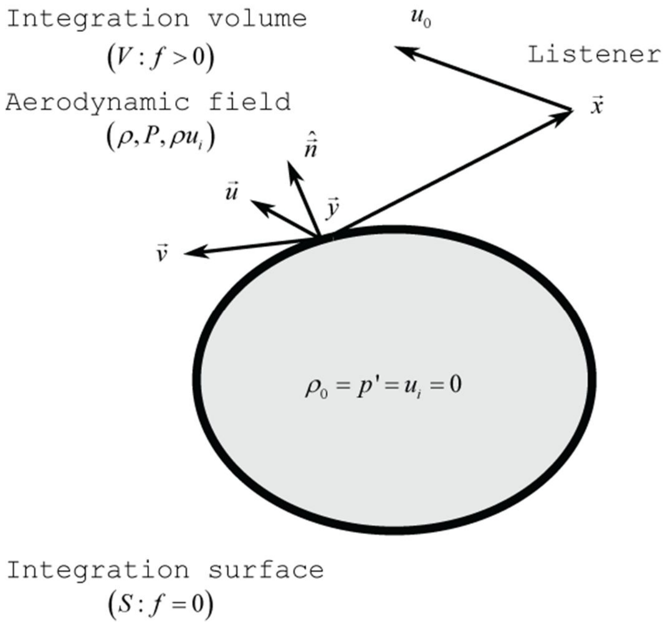

figure 136: FW-H definition overview

$$\frac{\partial \rho}{\partial t} + \frac{\partial}{\partial x_i}(\rho u_i) = \rho_0 u_n \delta(f) + (\rho - \rho_0)(u_n - v_n)\delta(f) \tag{5.6}$$

And equation (5.5) becomes:

$$\frac{\partial}{\partial t}\left(\rho u_i\right)+\frac{\partial}{\partial x_j}\left(P_{ij}+\rho u_i u_j\right)=P'_{ij}n_j\delta(f)+\rho u_i\left(u_n-v_n\right)\delta(f) \tag{5.7}$$

Where $P'_{ij}=P_{ij}-p_0\delta_{ij}$ is the perturbation stress tensor.

We can use expression (5.6) and (5.7) to construct an expression involving the wave operator. This is done by taking the divergence from equation (5.7) and subtracting it from equation (5.6) after differentiating it with respect to t:

$$\begin{aligned}\frac{\partial^2\rho}{\partial t^2}-\frac{\partial^2}{\partial x_i\partial x_j}\left(P_{ij}+\rho u_i u_j\right)=\frac{\partial}{\partial t}\left[\rho_0 u_n\delta(f)\right]+\frac{\partial}{\partial t}\left[\left(\rho-\rho_0\right)\left(u_n-v_n\right)\delta(f)\right]-\frac{\partial}{\partial x_i}\left[P'_{ij}n_j\delta(f)\right]\\-\frac{\partial}{\partial x_j}\left[\rho u_i\left(u_n-v_n\right)\delta(f)\right]\end{aligned}$$

Rearranging leads to:

$$\begin{aligned}\frac{\partial^2}{\partial t^2}\left(\rho-\rho_0\right)-c^2\frac{\partial^2}{\partial x_i\partial x_j}\left(\rho-\rho_0\right)=\frac{\partial}{\partial t}\left[\rho_0 v_n\delta(f)\right]-\frac{\partial}{\partial x_i}\left[P'_{ij}n_j\delta(f)\right]+\frac{\partial^2}{\partial x_i\partial x_j}\left[P_{ij}+\rho u_i u_j-c^2\left(\rho-\rho_0\right)\right]\\+\frac{\partial}{\partial t}\left[\left(\rho-\rho_0\right)\left(u_n-v_n\right)\delta(f)\right]-\frac{\partial}{\partial x_j}\left[\rho u_i\left(u_n-v_n\right)\delta(f)\right]\end{aligned}$$

This can be rewritten in a more compact way as:

$$\boxed{\Box^2\left[c^2\left(\rho-\rho_0\right)\right]=\frac{\partial}{\partial t}\left[Q\delta(f)\right]-\frac{\partial}{\partial x_i}\left[L_i\delta(f)\right]+\frac{\partial^2 T_{ij}}{\partial x_i\partial x_j}} \tag{5.8}$$

Which is known as the Ffowcs Williams – Hawkings equation for a permeable surface, where:

$$Q=\rho_0 U_i n_i,\quad U_i=u_i+\left(\frac{\rho}{\rho_0}-1\right)\left(u_i-v_i\right),\quad L_i=P'_{ij}n_j+\rho u_i\left(u_n-v_n\right)$$

And where

$$T_{ij}=P'_{ij}+\rho u_i u_j-c^2\left(\rho-\rho_0\right)\delta_{ij}$$

Is Lighthill's equivalent stress tensor.

V.I. Solution

For the solution of the FW-H equation, we use Green's functions. The Green's function G of the unbounded three-dimensional space is defined as $G = \delta(g)/r$, where $r = \|\vec{x} - \vec{y}\|$, $g = t - \tau - r/c$, and where $\vec{x}$ and $\vec{y}$ represent observer and source positions respectively. Furthermore, t is the observer time and τ is the source(emission) time. Note that equation (5.8) is a generalized wave equation of the form:

$$\frac{\partial^2 \phi}{\partial t^2} - c^2 \frac{\partial^2 \phi}{\partial x_i^2} = \frac{\partial^n Q_{ij\ldots}}{\partial x_i \partial x_j \ldots}$$

With ϕ and Q being generalized functions. Its formal solution is known, so that the solution of equation (5.8) is: (JONES 1964):

$$\begin{aligned} 4\pi p' = \frac{\partial^2}{\partial x_i \partial x_j} \iint_{f>0} \frac{\delta(t-\tau-r/c)}{r} T_{ij} dV d\tau - \frac{\partial}{\partial x_i} \iint_{f=0} \frac{\delta(t-\tau-r/c)}{r} L_i dS d\tau \\ + \frac{\partial}{\partial t} \iint_{f=0} \frac{\delta(t-\tau-r/c)}{r} Q dS d\tau \end{aligned} \tag{5.9}$$

On this equation, we can change integral variable using:

$$\int L(\tau)\delta(g(\tau)) = \sum_{n=1}^{N} \frac{L}{|\partial g / \partial \tau|}\left(\tau_{ret}^n\right)$$

Which is taking the sum over all the zero's τ_{ret}^n of the retarded time equation $g = 0$. Furthermore, note that:

$$\frac{\partial g}{\partial \tau} = -1 - \frac{1}{c}\frac{\partial r}{\partial \tau} = -1 + \frac{1}{c}\left(\frac{\partial \vec{y}}{\partial \tau} - \frac{\partial \vec{x}}{\partial \tau}\right) = -1 + M_r$$

The term $|1 - M_r|$ accounts for dilatation or contraction of the observer time scale with respect to the source time scale. This effect is known as the Doppler effect. Suppose the source elements are in subsonic motion. We denote $[\ldots]_{ret}$ as the evaluation at the retarded time:

$$\tau_{ret} = t - \frac{|\vec{x} - \vec{y}(\tau_{ret})|}{c}$$

With this, equation (5.9) can be written as:

$$4\pi p' = \frac{\partial^2}{\partial x_i \partial x_j} \int_{f>0} \left[\frac{T_{ij}}{r(1-M_r)}\right]_{ret} dV - \frac{\partial}{\partial x_i} \int_{f=0} \left[\frac{L_i}{r(1-M_r)}\right]_{ret} dS + \frac{\partial}{\partial t} \int_{f=0} \left[\frac{Q}{r(1-M_r)}\right]_{ret} dS \tag{5.10}$$

We will try to further rearrange this equation to something useful. This is done using the relation:

$$\frac{\partial}{\partial x_i}\int_{f=0}\left[\frac{\delta(g)}{r}\right]_{ret} dS=-\frac{1}{c}\frac{\partial}{\partial t}\int_{f=0}\left[\frac{r_i\delta(g)}{r^2}\right]_{ret} dS-\int_{f=0}\left[\frac{r_i\delta(g)}{r^3}\right]_{ret} dS \tag{5.11}$$

For the loading noise. For the quadrupole noise term, the above chain can be used twice to find: (Brentner & Farassat, 1998)

$$\frac{\partial^2}{\partial x_i \partial x_j}\int_{f>0}\left[\frac{\delta(g)}{r}\right]_{ret} dV=\frac{\partial}{\partial x_i}\left[-\frac{1}{c}\frac{\partial}{\partial t}\int_{f>0}\left[\frac{r_i\delta(g)}{r^2}\right]_{ret} dV-\int_{f>0}\left[\frac{r_i\delta(g)}{r^3}\right]_{ret} dV\right]=$$

$$\frac{1}{c^2}\frac{\partial^2}{\partial t^2}\int_{f>0}\left[\frac{\hat{r}_i\hat{r}_j\delta(g)}{r}\right]dV+\frac{1}{c}\frac{\partial}{\partial t}\int_{f>0}\left[\frac{\left(3\hat{r}_i\hat{r}_j-\delta_{ij}\right)\delta(g)}{r^2}\right]dV+\int_{f>0}\left[\frac{\left(3\hat{r}_i\hat{r}_j-\delta_{ij}\right)\delta(g)}{r3}\right]dV \tag{5.12}$$

Where $\hat{r}_i=\left(x_i-y_i\right)/r$ and δ_{ij} is the Kronecker delta. Using relations (5.11) and (5.12), equation (5.10) can be written as:

$$\begin{aligned}
4\pi p'=&\frac{1}{c^2}\frac{\partial^2}{\partial t^2}\int_{f>0}\left[\frac{T_{rr}}{r\left(1-M_r\right)}\right]_{ret} dV+\frac{1}{c}\frac{\partial}{\partial t}\int_{f>0}\left[\frac{3T_{rr}-T_{ii}}{r^2\left(1-M_r\right)}\right]_{ret} dV+\int_{f>0}\left[\frac{3T_{rr}-T_{ii}}{r^3\left(1-M_r\right)}\right]_{ret} dV\\
&+\frac{1}{c}\frac{\partial}{\partial t}\int_{f=0}\left[\frac{L_i\hat{r}_i}{r\left(1-M_r\right)}\right]_{ret} dS+\int_{f=0}\left[\frac{L_i\hat{r}_i}{r^2\left(1-M_r\right)}\right]_{ret} dS\\
&+\frac{\partial}{\partial t}\int_{f=0}\left[\frac{Q}{r\left(1-M_r\right)}\right]_{ret} dS
\end{aligned} \tag{5.13}$$

Where $T_{rr}=\hat{r}_i\hat{r}_jT_{ij}$ and $T_{ii}=T_{11}+T_{22}+T_{33}$. In (Brentner, 1997) it is demonstrated that:

$$\left.\frac{\partial}{\partial t}\right|_{\vec{x}}=\left[\frac{1}{\left(1-M_r\right)}\left.\frac{\partial}{\partial \tau}\right|_{\vec{x}}\right]_{ret}$$

$$\frac{\partial r}{\partial \tau}=-cM_r,\quad \frac{\partial \hat{r}_i}{\partial \tau}=\frac{\hat{r}_i cM_r-cM_i}{r},$$

$$\frac{\partial M_r}{\partial \tau}=\frac{1}{r}\left[\hat{r}_i\frac{\partial M_i}{\partial \tau}+c\left(M_r^2-M^2\right)\right]$$

Now we can rewrite equation (5.13) as:

$$\boxed{p'(\vec{x},t)=p'_Q(\vec{x},t)+p'_L(\vec{x},t)+p'_T(\vec{x},t)} \tag{5.14}$$

And thus the pressure pertubations are divided into 3 components, namely the thickness noise p'_Q, the loading noise p'_L and the quadrupole noise term p'_T, which are defined as:

Thickness noise:

$$4\pi p'_Q(\vec{x},t)=\int_{f=0}\left[\frac{\rho_0\dot{U}_n+U_{\dot{n}}}{r\left(1-M_r\right)^2}\right]_{ret}dS+\int_{f=0}\left[\frac{\rho_0 U_n\left(r\dot{M}_r+c\left(M_r-\left|\vec{M}\right|^2\right)\right)}{r^2\left(1-M_r\right)^3}\right]_{ret}dS \tag{5.15}$$

Where $\vec{M}$ is the Mach number vector of a source point on the integration surface. Furthermore:

$$U_n=U_i\hat{n}_i,\quad U_{\dot{n}}=U_i\dot{\hat{n}}_i,\quad \dot{U}_n=\dot{U}_i\hat{n}_i,\quad M_r=M_i\hat{r}_i,\quad \dot{M}_r=\dot{M}_i\hat{r}_i$$

Where the dots represents a derivative with respect to τ. This thickness noise accounts for the displacement of fluid due to the moving surface.

Loading noise:

$$\begin{aligned}4\pi p'_L(\vec{x},t)=&\frac{1}{c}\int_{f=0}\left[\frac{L_r}{r\left(1-M_r\right)^2}\right]_{ret}dS+\int_{f=0}\left[\frac{L_r-L_M}{r^2\left(1-M_r\right)^2}\right]_{ret}dS\\&+\frac{1}{c}\int_{f=0}\left[\frac{L_r\left(r\dot{M}_r+c\left(M_r-\left|\vec{M}\right|^2\right)\right)-L_M}{r^2\left(1-M_r\right)^3}\right]_{ret}dS\end{aligned} \tag{5.16}$$

Where

$$L_r=L_i\hat{r}_i,\quad \dot{L}_r\hat{r}_i,\quad L_M=L_iM_i$$

The loading noise accounts for the unsteady loading of forces and pressures of the surface on the fluid.

Quadrupole noise:

$$\boxed{4\pi p'_T(\vec{x},t) = \int_{f>0}\left[\frac{K_1}{c^2 r} + \frac{K_2}{cr^2} + \frac{K_3}{r^3}\right]_{ret} dV} \quad (5.17)$$

With:

$$K_1 = \frac{\ddot{T}_{rr}}{(1-M_r)^3} + \frac{\ddot{M}_r T_{rr} + 3\dot{M}_r \dot{T}_{rr}}{(1-M_r)^4} + \frac{3\dot{M}_r^2 T_{rr}}{(1-M_r)^5},$$

$$K_2 = \frac{-\dot{T}_{ii}}{(1-M_r)^2} - \frac{4\dot{T}_{Mr} + 2T_{\dot{M}r} + \dot{M}_r T_{ii}}{(1-M_r)^3}$$
$$+\frac{3\left[\left(1-\left|\vec{M}\right|^2\right)\dot{T}_{rr} - 2\dot{M}_r T_{Mr} - M_i \dot{M}_i T_{rr}\right]}{(1-M_r)^4} + \frac{6M_r\left(1-\left|\vec{M}\right|^2\right)T_{rr}}{(1-M_r)^5},$$

$$K_3 = \frac{2T_{MM} - \left(1-\left|\vec{M}\right|\right)T_{ii}}{(1-M_r)^3} - \frac{6\left(1-\left|\vec{M}\right|\right)T_{Mr}}{(1-M_r)^4} + \frac{3\left(1-\left|\vec{M}\right|\right)^2 T_{rr}}{(1-M_r)^5}$$

Where:

$$T_{MM} = T_{ij}M_i M_j, \quad T_{Mr} = T_{ij}M_i \hat{r}_j, \quad T_{\dot{M}r} = T_{ij}\dot{M}_i \hat{r}_j,$$
$$\dot{T}_{Mr} = \dot{T}_{ij}M_i \hat{r}_j, \quad \dot{T}_{rr} = \dot{T}_{ij}\hat{r}_i \hat{r}_j, \quad \ddot{T}_{rr} + \ddot{T}_{ij}\hat{r}_i \hat{r}_j$$

The quadrupole noise sources account for the non-linearities in the flow field outside the permeable surface(e.q. induced vortical disturbances, shocks and local sound speed variations.)

Equation (5.14) is the solution of the Ffowcs Williams- Hawkings for a permeable surface proposed by Farassat & Brentner. The loading, thickness and quadrupole noise terms as derived above are used in the FW-H code written by D. Casalino.

Bibliography

A. D'Alascio, A. R. (n.d.). *RAMSYS: A Parallel Code for the Aerodynamic Analysis of 3D Potential flows around Rotorcraft Configurations.* Capua, Italy.

A. Jameson, W. S. (1983). Numerical Solution of the Euler Equations by Finite Volume Methods.

Brentner, K. (1997). An efficient and robust method for predicting helicopter high-speed impulsive noise. *Journal of Sound & Vibration 203*, 87-100.

Brentner, K., & Farassat, F. (1998). Analytical comparison of the acoustic analogy and Kirchhoff formulation for moving surfaces. *American Institute of Aeronautics and Astronautics Journal 36*, 1379-1386.

Casalino, D. (2003). An advanced time approach for acoustic analogy predictions. *Journal of Sound & Vibrations*, 583-612.

Farassat, F. (2010, January). NASA TM 216178 - Open Rotor Noise Prediction at NASA Langley - Capabilities, Research and Development.

Ffowcs Williams J. E., H. D. (1969). Sound Generation by Turbulence and Surfaces in Arbitrary Motion. *Philosophical Transactions of the Royal Society*, 321-342.

Glauert, H. (1963). Airplane Propellers. In W. Durant, *Aerodynamic Theory* (pp. 170-201). New York: Dover Publications.

Jameson, A. (1983). Transonic flow calculations. *MAE-report 1651*.

Lighthill, M. (1952). On sound generated aerodynamically: 1. general theory. *Proceeding of The Royal Society, A 211*, pp. 564-578.

National Aerospace Laboratory NLR. (1987). *Memorandum I-87-005L: Boundary conditions for actuator-disk models of propellers in Euler calculations; method and software description.* Amsterdam.

Tomas, J. (2009). *Actuator Disk Modelling For Helicopter Rotors.* Internship report, CIRA.